The Hong Kong Polytechnic University

Department of Computing

New Generation of Automated Fingerprint Recognition System

Feng Liu

A Thesis

Submitted in partial fulfillment of the requirements

for the degree of

Doctor of Philosophy

September 2013

CERTIFICATE OF ORIGINALITY

I hereby declare that this thesis is my own work and that, to the best of my knowledge and belief, it reproduces no material previously published or written, nor material that has been accepted for the award of any other degree or diploma, except where due acknowledgement has been made in the text.

______________________________ (Signed)

Feng Liu (Name of student)

To My Family – *Love, Faith, and Hope*

ABSTRACT

NEW GENERATION OF AUTOMATED FINGERPRINT RECOGNITION SYSTEMS

By

Feng Liu

Fingerprint-based biometric is the most proven technique and has the largest market shares. It has been used for personal authentication for centuries and automated fingerprint recognition systems (AFRSs) have been used for decades. Although much progress has been made in AFRSs, the performance is still much lower than the expectations of people and theory estimation. Many new requirements are also raised along with more and more adoption of fingerprint technique in civilian applications, such as template security, hygiene, user-friendly and so on. For the purpose of further meeting people's needs (e.g. recognition accuracy, template security, and hygiene etc.), this thesis explores two types of advanced AFRSs, namely high-resolution AFRS and Touchless 3D AFRS. For high-resolution AFRS, we firstly recommend an optimal reference resolution by theoretical analysis and experimental simulation based on two most representative fingerprint features, minutiae and pores. Such reference resolution is helpful to solve problems such as cost, interoperability, and performance of an AFRS, so as to benefits the establishment of optimal AFRSs. To improve the recognition accuracy based on features on high resolution fingerprint images, a novel hierarchical fingerprint matching method is then proposed. The approach directly matches features in fingerprints by adopting a coarse-to-fine strategy. In the coarse matching step, a tangent distance and sparse representation-based matching method (denoted as TD-Sparse) is put forward. In the fine matching

step, false correspondences are further excluded by a weighted RANdom SAmple Consensus (WRANSAC) algorithm in which the weights of correspondences are determined based on their dis-similarity. High recognition accuracy is achieved since our proposed method is robust to noise and distortions of captured fingerprints and the inaccurate of extracted features. For touchless 3D AFRS, we firstly designed a touchless multi-view fingerprint acquisition device by optimizing parameters regarding the captured fingerprint image quality and device size. Optimization design of our device is demonstrated by introducing our design procedure and comparing with current touchless multi-view fingerprint acquisition devices. The efficiency of our device is further proved by comparing recognition accuracy between mosaicked images obtained by our proposed method and touch based fingerprint images. Then, 3D fingerprint images are generated by the proposed 3D reconstruction technique from captured touchless multi-view fingerprint images. The proposed reconstruction method puts emphasis on the correspondence establishment from 2D touchless fingerprint images and finger shape model estimation. Several popular used features, such as scale invariant feature transformation (SIFT) feature, ridge feature and minutiae, are considered for correspondence establishment. Binary quadratic function is found to be more suitable for finger shape model compared with another mixed model we proposed by analyzing 440 3D point cloud finger data collected by the structured light illumination (SLI) method. 3D fingerprint reconstruction results from different fingerprint feature correspondences are then given and the reconstruction accuracy is finally analyzed and compared. After that, 3D fingerprint features and their applications for personal authentication are studied. We define the 3D finger structural features, such as curve-skeleton, overall maximum curvatures as Curvature Fingerprint Features and investigate their distinctiveness for user authentication. These features are also used to assist fingerprint matching and make contribution to fingerprint recognition by combining with 2D

fingerprint features. Since more information can be captured by touchless imaging, we propose an end to end solution for user authentication based on images captured by our designed touchless fingerprint acquisition device. Preprocessing steps including region of interest (ROI) extraction and image correction are implemented on the three views of raw fingerprint images captured by our device. New feature--Distal Interphalangeal Crease (DIP) based feature is then extracted and matched to recognize the human's identity in which part selection is introduced to improve matching efficiency. Experimental results show the effectiveness of combining DIP-based feature with other features for touchless fingerprint recognition systems.

LIST OF PUBLICATIONS

1. David Zhang, **Feng Liu**, Qijun Zhao, Guangming Lu, Nan Luo, “Selecting a reference high resolution for fingerprint recognition using minutiae and pores,” *IEEE T. Instrumentation and Measurement*, vol. 60, no. 1, pp. 863-87, Mar. 2011.
2. **Feng Liu**, Qijun Zhao, David Zhang, “A novel hierarchical fingerprint matching approach,” *Pattern Recognition*, vol. 44, no. 8, pp. 1604-1613, Aug. 2011.
3. **Feng Liu**, David Zhang, Changjiang Song, Guangming Lu, “Touchless multi-view fingerprint acquisition and mosaicking,” *IEEE T. Instrumentation and Measurement*, vol. 62, no. 9, pp. 2492 - 2502, Sep. 2013.
4. **Feng Liu**, David Zhang, Zhenhua Guo, “Distal Interphalangeal Crease based User Authentication System,” *IEEE T. Information Forensics and Security*, vol. 8, no. 9, pp. 1446 - 1455, Sep. 2013.
5. **Feng Liu**, David Zhang, “3D fingerprint reconstruction system using feature correspondences and finger shape model,” *Pattern Recognition*, to be published, 2013.
6. **Feng Liu**, David Zhang, “3D Fingerprint recognition using curvature features,” *Pattern Recognition*, under review.
7. **Feng Liu**, Wangmeng Zuo, David Zhang, “3D Reconstruction Model without Corner Points,” *IEEE T. Pattern Recognition and Machine Intelligence*, under review.
8. Biao Hou, **Feng Liu**, Licheng Jiao, Huidong Bao, “Image segmentation based on wavelet domain hidden markov tree model,” *J. Infrared Millim. Waves*, vol. 28, no. 2, pp. 156-160, Apr. 2009.
9. Biao Hou, **Feng Liu**, Licheng Jiao, Huidong Bao, “A multiscale texture image segmentation algorithm based on adaptive window fixing and propagation,” *J. Acta Electronica Sinica*, vol. 37, no. 7, pp. 1492-1501, July 2009.
10. Biao Hou, Jing Xu, **Feng Liu**, Licheng Jiao, “Image segmentation using second generation bandelet-domain hidden markov tree models,” *J. Acta Automatica Sinica*, vol. 35, no. 5, pp. 498-504, May 2009.
11. **Feng Liu**, Qijun Zhao, Lei Zhang, David Zhang, “Fingerprint Pore Matching Based on Sparse Representation,” *ICPR*, 2010, pp. 1630-1633.
12. Qijun Zhao, **Feng Liu**, Lei Zhang, David Zhang, “A comparative study on quality assessment of high resolution fingerprint images,” *ICIP*, 2010, pp. 3089-3092.
13. Qijun Zhao, **Feng Liu**, Lei Zhang, David Zhang, “Parallel versus Hierarchical Fusion of Extended Fingerprint Features,” *ICPR*, 2010, pp. 1132-1135.

ACKNOWLEDGEMENTS

I would like to appreciate all those people who have made everything possible for me to finish the Ph.D. degree. First and foremost, I am deeply grateful to my chief supervisor, Prof. David Zhang. It is him who provides a chance to me to open my research field. It is him who continuously supports and encourages me during my four years Ph.D. career. It is him who gives professional advice and help to me to complete my research study. I cannot finish this thesis without his guidance. I am also indebted to him for setting an example to me about how to treat work, life and people. I am lucky to have him as my supervisor.

I owe acknowledgement to Dr. Lei Zhang, Prof. Jane You, Dr. Ajay Kumar, Prof. Yong Xu and Dr. Wangmeng Zuo and Dr. Guangming Lu for their unconditional help to both of my study and life during my Ph.D. period. I have learnt a lot from them by listening to their talks and discussing with them.

It is my fortune to have Jerry Zhao, Denis Guo, Andy Wang, Madge Guo, Vivek Kanhangad, Nan Luo, Wei Li, Lin Zhang, Jin Xie, Bo Peng, Qin Li, Xiaofeng Qu, Kunai Zhang, Kai Chen, Dimin Wang, Fangmei Chen, Ke Yan, Meng Yang, Kaihua Zhang, Pengfei Zhu, Jinghua Wang, Lei Xu, Dr. Qinghua Hu, Dr. Haomian Zheng, Dr. Wei Jia, Dr. Ya Su and Dr. Weisheng Dong, as my colleagues. They play important role in my academic career. Much research work and papers are finished after discussion with them.

Special word of appreciation goes to all my friends in Hong Kong, especially lilly Li, Bin Liao, Renqi Zhang, Dingyong Hu, Dr. King Hong Cheung, and Tian Tuo. Thanks them to make my life in Hong Kong colorful. Thank all of the nice colleagues in the department and university for their support.

Finally, my sincere thanks go to my parents, parents-in-law, and sisters for their incredible love, encouragement, and support. The love and understanding from my husband Huidong Bao makes the completion of this thesis to be possible. I am very thankful to have them as my family members and I dedicate this thesis to them.

TABLE OF CONTENTS

LIST OF FIGURES

LIST OF TABLES

Chapter 1
Introduction

1.1 Biometric Recognition

Nowadays, with the development of technology, biometric recognition has been widely employed in various domains no matter for forensics (e.g. criminal identification, and prison security) or civilian uses (e.g. access to buildings, airport check-in, electronic banking and credit card, web access, ATM security, computers and cell phones). The role of biometrics in such applications is to guarantee that the facilities are accessed by the legitimate user. The popular adoption of biometrics rather than knowledge-based (passwords) and token-based (keys) techniques for security is because biometric recognition is inherently more reliable than the other two techniques. Fig. 1.1 shows the annual biometric industry revenues reported by International Biometric Group (IBG) [1]. This report was studied and authored by biometric technology experts with years of hands-on experience deploying and testing leading biometrics systems. It can be seen that there are growing trends of biometric industry in the near future.

Generally, biometric recognition refers to user authentication using his/her physiological or behavioral traits [2-6]. Such traits are unique and distinctive, cannot be shared or forgotten, and the user to be recognized is required to be physically presented at the scene of authentication. Typical physiological biometric traits include fingerprint, face, iris, vein, hand geometry and so on, while signature and gait are two examples of behavioral traits. The weights of various biometric technologies are different in the global market. As the report given by BCC Research [7] shown in Fig. 1.2, the global market for biometric technologies is grown steadily throughout the forecast period. This market was estimated at $5 billion in 2010 and is expected to reach a value of nearly $12 billion by 2015, at a compound annual growth rate (CAGR) of 18.9%. The market for fingerprint-based technologies accounts for the greatest share of the global biometrics market and is forecast to continue to be the main source of overall market revenues from 2010 to 2015 and beyond. This sector was valued at $2.7 billion in 2010 and is expected to increase at a 19.6% compound annual growth rate (CAGR) to reach nearly $6.6 billion in 2015. This report demonstrated the leading role of fingerprint-based verification among biometrics. We thus were motivated to investigate advanced fingerprint-based techniques.

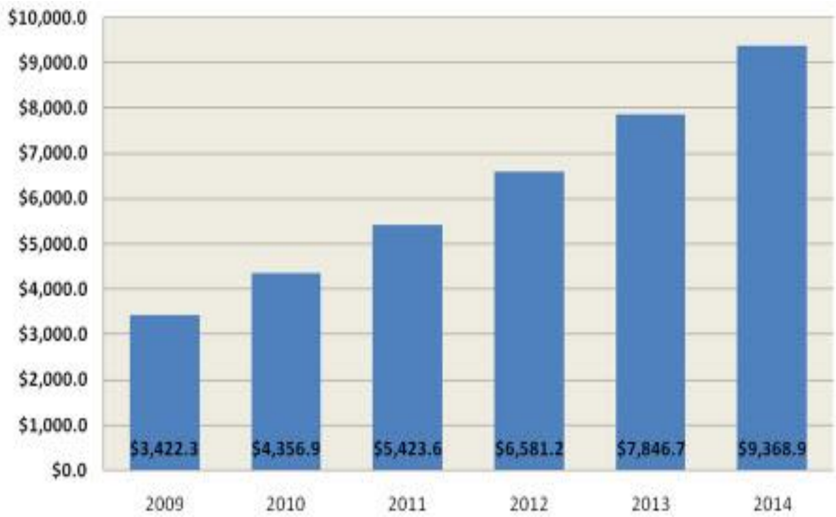

Fig. 1.1: Annual biometric industry revenues, 2009-2014 (Adapted from IBG Reports: https://ibgweb.com/products/reports/bmir-2009-2014).

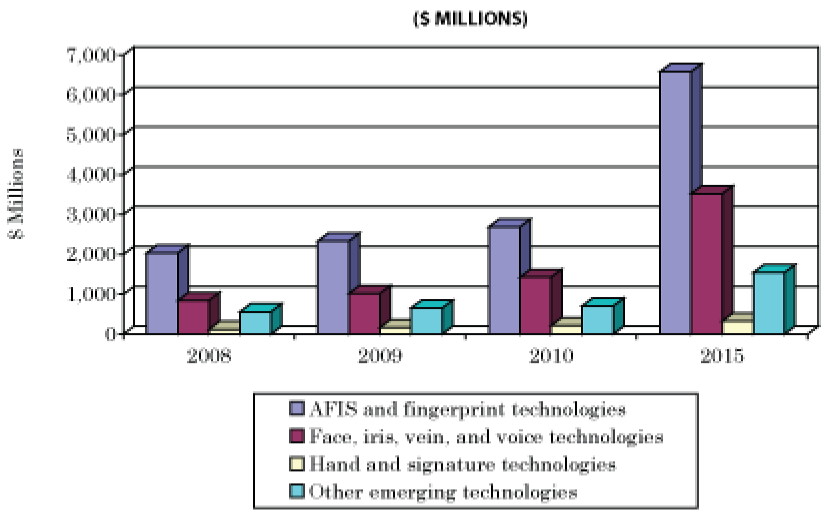

Fig. 1.2: Summary of global market for various biometric technologies, 2008-2015. (Adapted from BCC Research: http://www.bccresearch.com/report/biometrics-technologies-markets-ift042c.html).

1.2 Fingerprints

In a narrow sense, a fingerprint is defined as an impression left by the friction ridges of a human finger. In a broad sense, fingerprints are impressions of the friction ridges of all or any part of fingers [8]. Fig. 1.3 gives a fingerprint image example we commonly referred. The individuality of fingerprints was theoretically studied [9-11] and results demonstrated the uniqueness of fingerprints that it would be virtually impossible for two fingerprints (even two fingerprints of identical twins) to be exactly alike.

Fig. 1.3: Human fingerprint.

1.2.1 Fingerprint History

The evidence of main's first discovery of fingerprints can be traced back to 300 B. C. in Egypt and China [12]. The ancient Babylonians pressed their fingetips into clay for business transactions, while the Chinese used thumb prints for clay seals and used ink-on-paper fingerprints for business. However, it was till 19th century that fingerprinting was taken as a means of positive identification. In 1858, Sir William Herschel began requiring fingerprints on contracts [13, 14]. In 1880, Dr. Henry Faulds -- a Scottish surgeon in a Tokyo hospital, published an article in the scientific journal: "Nature", talking about the use of printers ink as a method for obtaining fingerprints and taking such fingerprints for personal identification. He established the first fingerprint classification system and was also the first person to identify fingerprints left on an alcohol bottle [15]. Starting in 1888, Sir Francis Galton began collecting fingerprints and eventually gathered ~8,000 different samples to analyze. He then published a book called "Fingerprints" in 1892, in which he introduced works about fingerprints, compared fingerprints using minutiae feature, identified patterns and created a fingerprint classification system [16]. Such works thus made fingerprints suitable for forensics and the first criminal fingerprint identification using Galton's system was made by Juan Vucetich in 1892. In 1896, Sir Edward Richard Henry established his own classification system, namely Henry classification system, based on Galton's technique [17]. This well-known system was adopted by Scotland Yard to establish the first Fingerprint Bureau in 1901. In the following year, fingerprints were for the first time taken as evidence in English courts. The New York state prisons adopted fingerprints in 1903 followed later by the FBI. The Henry system was the most popular method of classifying and identifying fingerprints in law enforcement agencies from then until the computer age.

With the fast development of fingerprint recognition techniques, people realized that it must find an automated method to operate fingerprints since it is infeasible to do fingerprint identification manually for large fingerprint databases. For instance, the total number of fingerprint cards included in the FBI fingerprint database is over 200 million from its original number of 810,000, and the number is still increasing. Fortunately, the advent of computers made it possible to classify, search for and match fingerprints automatically [17]. In the 1980s, the Japanese National Police Agency paved the way for this automation. They established the first electronic fingerprint matching system. Their Automated Fingerprint Identification Systems (AFIS), eventually enabled law enforcement officials around the world to cross-check a print with millions of fingerprint records almost instantaneously. These systems had not only greatly improved the operational efficiency of law enforcement agencies but also reduced the cost of labors expert at fingerprints. Besides for forensics, it also was adopted for civilian and commercial applications (e.g. welfare disbursement, cellular phone access, and laptop computer login) with the rapid development of automatic fingerprint recognition technique.

1.2.2 Fingerprint Acquisition

Fingerprint acquisition is the first step of fingerprint recognition systems. Generally, fingerprint can be imaged off-line or live-scan. An off-line fingerprint image is usually acquired based on ink-techniques, in which finger skin is first smeared with ink and then pressed against a paper, and finally digitized by means of a paper-scanner. Latent fingerprints are another special kind of off-line images. They are ubiquitous at crime scenes due to the contact between oily human skin and the surface of some objects. Such impressions can be lifted from the surface where they are left by using specific chemicals. The acquisition of live-scan fingerprint image is achieved by sensing the tip of the finger directly. The advantages of live-scan fingerprinting includes: 1) Avoiding problems associated with ink prints, such as smudging, smearing, and over or under inking. 2) High processing speed. 3) Convenient to users. Thus, live-scan acquisition is gradually took the place of off-line fingerprinting and becomes the main stream fingerprint imaging technique for AFRSs.

The key part of a live-scan fingerprint acquisition device is its sensor. By using current effective, efficient, and user-friendly live-scan fingerprint sensors, on-line fingerprint image acquisition becomes possible, so as to spread the applications of fingerprint recognition techniques. Nowadays, the existing sensors fall into three categories: optical, silicon, and ultrasound [18, 19]. Among these sensors, silicon-based sensors (e.g. capacitive, thermal, electric field and piezoelectric) are usually employed for consumer products popularity such as laptop computers, cellular phones and PDAs due to their small size and low cost [20-24]. However, it is hard to achieve high quality or high resolution fingerprint images by using such kind of sensors [24]. For ultrasound sensors [25, 26], they can achieve high quality fingerprint images since they are insensitive to the skin accumulations (dirt or oil). However, they are large in size, costly and take long time to acquire an image [18, 24]. Thanks to the merits of stable, reliable, easy to implement and relatively low cost, optical sensors have been used for fingerprint imaging for a long time compared with the usage of other two types of fingerprint sensors [18, 27]. The existing optical sensors mainly consist of Frustrated Total Internal Reflection (FTIR)-based [28-30], optical fibers [31], electro-optical [32], direct reading [33-40] and multispectral imaging [41]. Among them, FTIR-based sensor and direct reading are frequently-used for fingerprint acquisition. The devices designed to capture fingerprint images in our thesis are based on this two kinds of optical sensors.

Each of the two kinds of sensor-based acquisition technique has its own merits and drawbacks. For example, the FTIR-based acquisition needs contact between finger and prism while direct reading captures fingerprint image by a high-quality camera at a distance (touchless acquisition) [18]. The quality of captured fingerprint images by them is quite different, as the example images shown in Fig. 1.4. it can be seen that the difference from these parameters characterizing a digital fingerprint image (e.g. resolution, effective print area, geometric accuracy, contrast, and geometric distortion). We described the details of the merits, drawbacks, as well as the motivations of adopting different sensors in our fingerprint acquisition devices in the following chapters.

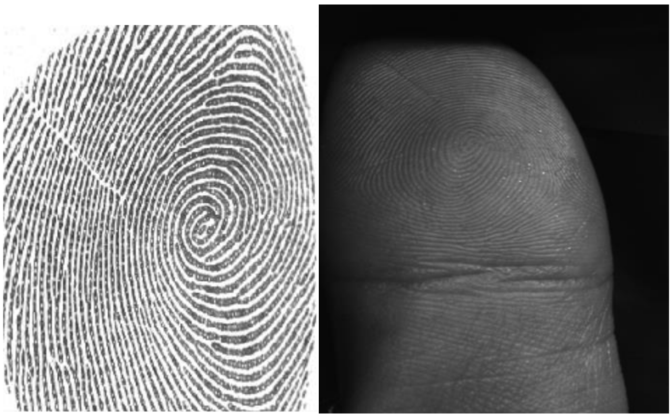

(a) (b)

Fig. 1.4: Example fingerprint images captured by different sensors. (a) FTIR-based sensor. (b) Direct reading.

1.2.3 Fingerprint Features

In a real world situation, the same fingerprint scanned twice may look different due to some distortions and skin conditions. Thus, salient features but not directly the pixel intensity values of fingerprint image are usually used to discriminate between identities. Fingerprint features have been comprehensively studied in the last decades. In general, features on fingerprints are categorized at different scales and fall into three levels [12]. Features on the first level are defined by ridge patterns globally. Such as the examples of the fingerprint classes shown in Fig. 1.5 (left loop, right loop, whorl and arch). Singular points (cores and deltas) [42], external fingerprint shape, orientation and frequency maps of fingerprint ridges also belong to this category. The level 2 features mainly refer to minutiae (e.g. ridge endings and ridge bifurcations) [43]. They are stable and robust to fingerprint conditions. Thus, they become the basis of most existing AFRSs. Level 3 features are defined as intra-ridge details. Finger sweat pore is one of the most important level 3 features [45]. Others also include width, curvature, edge contours and so on. However, exacting such level features like sweat pores requires high-resolution (e.g., 1,000 dpi) fingerprint images with good quality. Since most existing AFRSs are equipped with fingerprint sensors of ~500dpi, level-3 features attract little attention by them. Recently, researchers found it is difficult to robustly extract the above mentioned three levels of fingerprint features from very low resolution fingerprint images (~50 dpi, e.g. touchless fingerprint images captured by a webcam) [45]. They designated a coarser level of fingerprint features--level zero features. This level features consist of broken line-like patterns representing creases and ridges of varying clarity, which can be extracted and used for human identification.

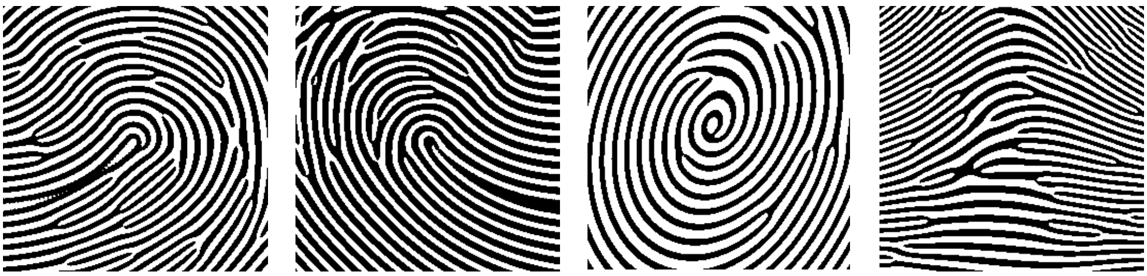

(a) (b) (c) (d)

Fig. 1.5: Example fingerprint classes. (a) Left loop. (b) Right loop. (c) Whorl. (d) Arch.

1.2.4 Fingerprint Matching

Fingerprint matching is an essential and tough task for fingerprint-based personal authentication. User's identity will be confirmed only after matching. The difficulty of matching exists in the large intra-class variations among different impressions of the same finger. Such variations include displacement, rotation, non-linear distortion, partial overlap, changing skin condition, variable pressure, noise, and feature extraction errors. For manual fingerprint matching, there are mainly three aspects an expert considered when comparing two fingerprints. Firstly, they check the global fingerprint pattern configuration. Secondly, they examine the minutiae details. Thirdly, the number of identical minutiae should be counted [18]. In fact, there are detailed and specific protocols and flowcharts guide for manual fingerprint matching.

Algorithms about fingerprint matching usually refer to automatic fingerprint matching. In general, they can be classified into three categories: correlation-based matching, minutiae-based matching and non-minutiae feature-based matching. Correlation-based matching compares the global pattern of ridges and valleys to see whether the patterns of two fingerprints are aligned or not [46-48]. The performance heavily affects by the distortions and noise present in the fingerprint image. Minutiae-based matching tries to find the alignment between two sets of minutiae points and figure out the maximum number of matched minutiae pairs [18, 49, 50]. The matching results of minutiae-based methods rely on minutiae extraction accuracy and the techniques used to handle the non-rigid transformation between two minutiae sets. Non-minutiae feature-based matching refers to match fingerprints using other features beyond minutiae [51-54]. Those features include fingerprint additional features, texture information, local orientation and frequency. Such kind of methods is found to be very effective with poor quality fingerprint images and also helpful to increase system accuracy and robustness when combined with minutiae-based matching.

1.3 Overview of Automated Fingerprint Recognition Systems

Automated Fingerprint Recognition Systems (AFRSs) generally refer to capturing fingerprints through electronics and recognizing the obtained digital fingerprint images automatically. The advent of AFRSs is promoted by the increasing workloads and time-consuming tasks of manually comparing fingerprints by experts. AFRSs had been deeply studied over the past 4 decades and now widely used in applications such as attendance and access control systems [18, 49, 55-57]. Fig. 1.6 shows the framework of a general AFRS. We can see that it consists of two modules. One is enrollment module and another is matching module. Since the steps of the enrollment module are almost included in the matching module, an AFRS mentioned in this thesis omits the enrollment module. So far, lots of methods about fingerprint preprocessing, feature extraction and matching have been proposed in the literature to solve different problems involved in AFRSs [50, 58-67].

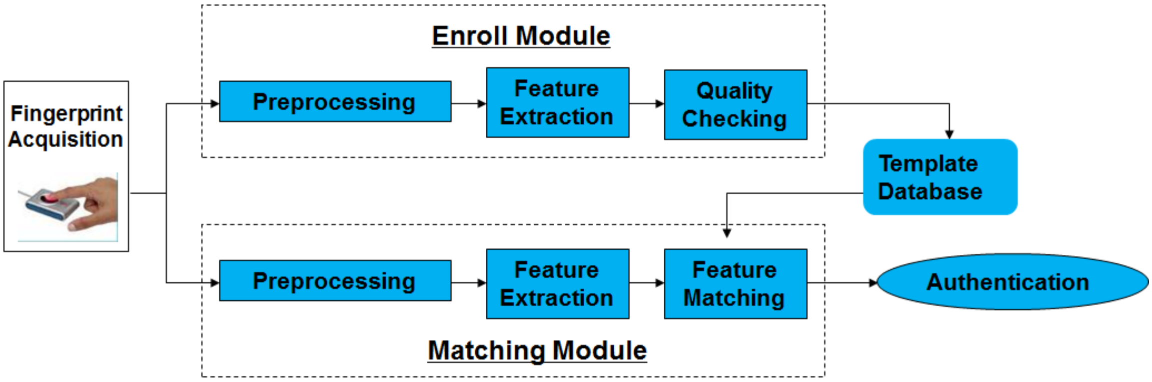

Fig. 1.6: Framework of a general automated fingerprint recognition system.

In the early studies, almost all of the AFRSs are minutiae-based systems since minutiae are distinctive and stable fingerprint features, and can be robustly extracted from fingerprint images at a resolution of ~500dpi [12, 18, 57]. However, with the development of fingerprint imaging techniques, higher performance and more new requirements (e.g. hygiene and user-friendly) can be achieved by improving earlier minutiae-based AFRSs. For instance, by using high resolution fingerprint imaging technique, high quality fingerprint image can be obtained which permits the extraction of fingerprint additional features (e.g. level 3 features). Such features are found to be helpful to enable high-confidence and more accurate matching, especially when partial fingerprints with insufficient minutiae are used for authentication [68]. Stosz and Alyea proposed the first modern high resolution AFRS in 1994 [54]. In their AFRS, they extracted pores and minutiae from fingerprint images at a resolution of approximately 1,270dpi*2,400dpi (vertical*horizontal). Both of these features are then used to recognize fingerprints. Great improvement on the recognition accuracy is finally achieved when compared with minutiae-based AFRS. After that, more advance pore extraction and matching methods were proposed to build high performance AFRS [69-80]. Such researches further demonstrate that fingerprint recognition accuracy will be increased by including level-3 features which just can be extracted from high resolution fingerprint images. Another example is the development of touchless 3D AFRS. As we all know, touchless fingerprint imaging technique has advantages of being insensitive to skin deformation and skin conditions, avoiding distortions and inconsistencies due to projecting an irregular 3D finger onto a 2D flat plane image, securing against latent fingerprints, practically maintenance free, being hygienic and robust to fake attacks. Multi-view imaging further provides a way to generate 3D shape of human finger. Such merits permit new developed AFRS to meet more requirements for civilian applications and provide more reliable recognition by using 3D information. Earlier work about touchless fingerprint recognition is leaded by Kim et al. in Korea

[81]. They proposed a prototype of touchless fingerprint recognition system using a camera sensor and processed the captured fingerprint images in their following work [37, 82]. Furthermore, new multi-view fingerprint acquisition devices and a mosaicking method used to splice different view of images into one are proposed by them in 2010 [83]. In 2007, an end to end solution of fingerprint recognition system is proposed by Hiew et al. using Gabor feature and SVM classifier [84]. Kumar et al. proposed a low resolution touchless fingerprint recognition system using their own defined Level Zero Feature [45]. Parziale et al. designed a multi-camera touchless fingerprint capture device and proposed 3D minutiae for fingerprint recognition [35]. Even though there are lots of works about touchless fingerprint recognition, few of them gave recognition results and a thorough analysis about 3D information generated from touchless multi-view fingerprint images.

1.4 Problems and Challenges Couple with the Development of AFRSs

Even huge achievements had been made after the fast development of AFRSs in the last several tens of years, the performance of current AFRSs is still not meet the market requirements yet. There are some problems not well solved in the literature and new issues arose.

The first problem concerned about high resolution AFRS is the image resolution. Image resolution is one of the main parameters affecting the captured digital fingerprint image quality. It plays important role in the design and deployment of AFRS and impacts both their cost and recognition performance. It is necessary to provide a standard resolution for high resolution AFRS. Unfortunately, different resolutions were used in the study of current high resolution AFRS.

Even though high recognition accuracy can be achieved by combining level 2 and level 3 features for high resolution AFRS, it still has space to improve the accuracy. Higher accuracy can be obtained if a more advanced matching method is used. Since noise and distortion may be introduced during fingerprint acquisition and feature extraction (see Fig. 1.7), there are errors in the fingerprint representation. Thus, it is required to propose more effective matching algorithm which is robust to these errors to improve recognition accuracy at certain degree.

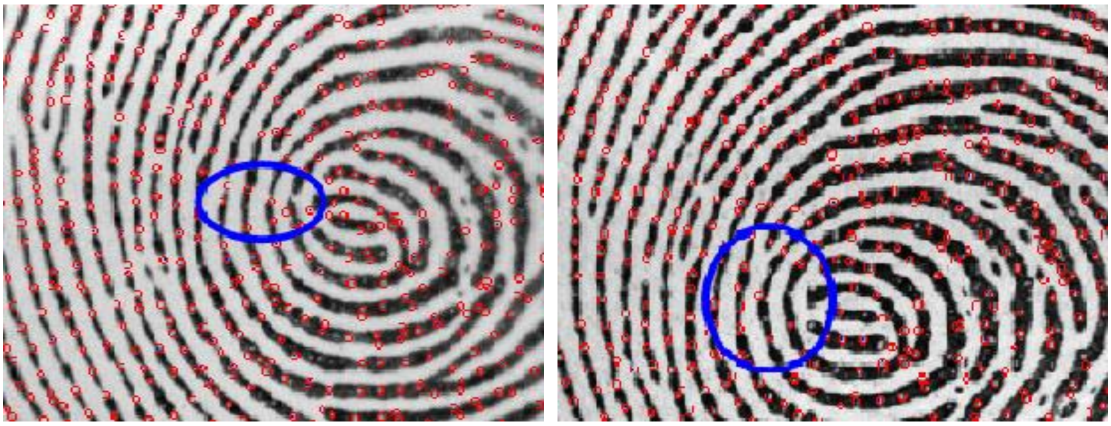

Fig. 1.7: Two prints of one finger captured at different times, where red circles represent the position of extracted pores and blue labeled the errors caused by feature extraction algorithms.

Although there were many studies about touchless fingerprint recognition, there were few works talking about the design of optimal touchless fingerprint acquisition device, construction of accurate 3D finger shape from 2D fingerprint images, and researches of 3D fingerprint recognition techniques. Such issues are of great importance to the development of touchless 3D AFRS. They are also very difficult problems needs to be investigated.

Due to the essential drawback of low ridge-valley contrast of touchless fingerprint imaging, it is difficult to correctly extract classical fingerprint features (e.g. minutiae) from touchless fingerprint images. This drawback resulted in low recognition accuracy of touchless-based fingerprint recognition. Therefore, it is required to propose effective recognition methods specific to touchless fingerprint images. Such methods should overcome the drawbacks of touchless fingerprint images to achieve high recognition accuracy.

1.5 Outline of the Thesis

To settle the issues mentioned in the previous section, this thesis presented a number of novel methods for reference high resolution establishment, sweat pore matching, touchless multi-view fingerprint image acquisition, 3D fingerprint reconstruction, 3D fingerprint feature extraction and matching, and user authentication based on touchless multi-view fingerprint images. The details of these methods were described in the subsequent chapters and the outline of each chapter was summarized as follows.

Chapter 2 describes the method we proposed to establish the reference resolution for high resolution AFRS. First of all, we collected multi-resolution (from 500dpi to 2,000dpi) fingerprint images as candidates for resolution selection. Secondly, we set three criteria based on minutiae and pores to select the optimal resolution. Finally, the reference resolution was recommended based on theoretical analysis, the setting criteria and recognition performance comparison.

In Chapter 3, we proposed a pore matching method to improve recognition accuracy. Pores extracted from high resolution fingerprint images were matched using a coarse-to-fine strategy. Coarse pore correspondences were firstly established based on a tangent distance obtained by a sparse representation based matching method. Pore correspondences were then further refined by a weighted RANdom SAmple Consensus algorithm, where weights of pore correspondences were determined based on the dis-similarity between the pores in the correspondences. The better performance of our proposed method compared with other state-of-the-art pore matching methods was demonstrated by experiments conducted on two databases of high resolution fingerprints.

We presented a touchless multi-view fingerprint acquisition device in Chapter 4. By considering the captured fingerprint image quality and device size, several parameters of the device were optimized. They mainly include the Lens selection and distance setting, light source selection, and the camera number and arrangement. We also introduced a fingerprint mosaicking method to stitch the different views of touchless fingerprint images of a finger to one new image with larger area. Experiments shown the effectiveness of our designed device by comparing recognition accuracy between mosaicked images obtained by our proposed method and touch-based fingerprint images.

In Chapter 5, we put forward a 3D fingerprint reconstruction method to generate 3D fingerprint images for 3D fingerprint recognition. Since 3D finger shape can be reconstructed from its 2D fingerprint images, we investigated the technique for 3D fingerprint reconstruction. There are mainly five steps for our reconstruction method, including camera parameters calculation, correspondences establishment, 3D coordinates computation, shape model estimation, and interpolation. We put emphasis on introducing correspondences establishment and finger shape model estimation in the chapter. 3D fingerprint reconstruction results based on different fingerprint feature correspondences were finally given based on our proposed method. The best result was finally selected out to establish our 3D fingerprint image database by analyzing the reconstruction accuracy.

Chapter 6 then for the first time studied 3D fingerprint recognition. Coarser finger structure features than level 1 fingerprint features were proposed and defined firstly. Then, we extracted and matched such features. The case studies of such features' application were given in the experimental part. We concluded that the curve-skeleton feature can be used to assist fingerprint recognition and the overall maximum curvatures would be used for human gender classification.

In Chapter 7, we described an end to end touchless multi-view fingerprint recognition system. This system was proposed based on the touchless fingerprint images captured by our own designed device introduced in Chapter 4. We firstly defined new feature--Distal Interphalangeal Crease (DIP) based feature on the captured fingerprint image. Then, the corresponding feature extraction and matching methods were proposed. By comparing matching results using SIFT or minutiae, we found higher recognition accuracy can be achieved using the proposed DIP-based feature. Promising EER was obtained when combining DIP-based feature with SIFT and minutiae for touchless fingerprint recognition.

Chapter 8 summarized the research contributes of the thesis and indicated the future directions which would further improve our research and the development of AFRSs.

Chapter 2
Selecting a Reference High Resolution for Fingerprint Recognition System

High-resolution AFRSs offer higher security because they are able to make use of level 3 features, such as pores, that are not available in lower-resolution (<500dpi) images. One of the main parameters affecting the quality of a digital fingerprint image and issues such as cost, interoperability, and performance of an AFRS is the choice of image resolution. In this chapter, we identify the optimal resolution for an AFRS using the two most representative fingerprint features, minutiae and pores. We first designed a multi-resolution fingerprint acquisition device to collect fingerprint images at multiple resolutions and captured fingerprints at various resolutions but at a fixed image size. We then carried out a theoretical analysis to identify the minimum required resolution for fingerprint recognition using minutiae and pores. After experiments on our collected fingerprint images and applying three requirements for the proportions of minutiae and pores that must be retained in a fingerprint image, we recommend a reference resolution of 800dpi for high-resolution AFRS.

2.1 Backgrounds

As one of the most popular biometric traits, fingerprints are widely used in personal authentication, especially with the availability of a variety of fingerprint acquisition devices and the advent of thousands of advanced fingerprint recognition algorithms. Such algorithms make use of distinctive fingerprint features which can usually be classified at three levels of detail [12], as shown in Fig. 2.1 and referred to as level 1, level 2, and level 3. Level 1 features are the macro details of fingerprints such as singular points and global ridge patterns, such as deltas and cores (indicated by red triangles in Fig. 2.1). They are not very distinctive and are thus mainly used for fingerprint classification rather than recognition. The level 2 features (red rectangles) primarily refer to the Galton features or minutiae, namely ridge endings and bifurcations. Level 2 features are the most distinctive and stable features, which are used in almost all AFRSs [12, 18, 57] and can be reliably extracted from low resolution fingerprint images (~500dpi). A resolution of 500dpi is also the FBI's (Federal Bureau of Investigation) standard fingerprint resolution for AFRS using minutiae [76, 54]. Level 3 features (red circles) are often defined as the dimensional attributes of the ridges and include sweat pores, ridge contours, and ridge edge features, all of which provide quantitative data supporting more accurate and robust fingerprint recognition. Among these features, pores have been most extensively studied [54, 69-79, 85] and are considered to be reliably available only at a resolution higher than 500dpi.

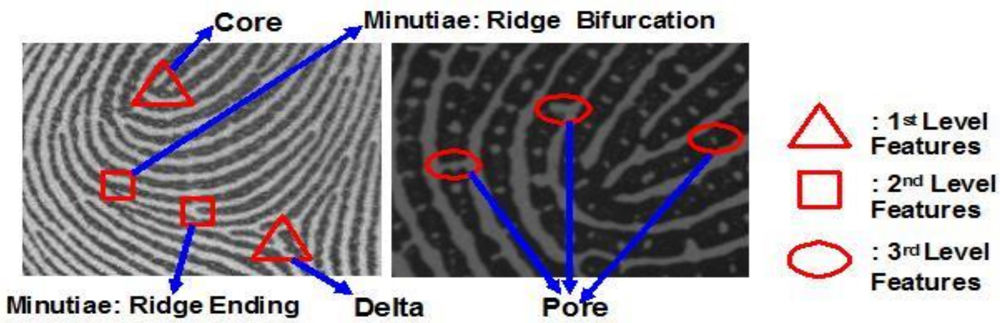

Fig. 2.1: Three levels of fingerprint features.

Resolution is one of the main parameters affecting the quality of a digital fingerprint image and so has an important role in the design and deployment of AFRS and impacts both their cost and recognition performance. Despite this, the field of AFRS does not currently have a well-proven reference resolution or standard resolution for high resolution AFRS which can be used interoperably between different AFRSs. For example, Stosz and Alyea extracted pores at a resolution of approximately 1,270dpi in the vertical direction and 2,400dpi in the horizontal direction (1,270dpi*2,400dpi) [54]. Jain et al. chose a resolution of 1,000dpi based on the 2005 ANSI/NIST fingerprint standard update workshop [76]. CDEFFS [73] defined level 3 features at a resolution of 1,000dpi. Zhao et al. proposed some pore extraction and matching methods at a resolution of 902dpi*1,200dpi [70-72]. Finally, the International Biometric Group (IBG) analyzed level-3 features at a resolution of 2,000dpi [74].

In this chapter, we take steps toward establishing such a reference resolution, assuming a fixed image size and making use of the two most representative fingerprint features, minutiae and pores, and providing a minimum resolution for pore extraction that is based on anatomical evidence. The use of a fixed image size is determined by the fact that the quality of a digital fingerprint image is mainly determined by three factors, the resolution, the number of pixels in a fingerprint image, and the measured area of the fingerprint, with it being possible to uniquely determine the value of any one given the other two. In analyzing the influence of resolution on AFRS, it was thus necessary to fix one of the other two parameters. Here, we choose to fix the image size. We conducted experiments on a set of fingerprint images of different resolutions (from 500dpi to 2,000dpi). By evaluating these resolutions in terms of the number of minutiae and pores, the results have shown that 800dpi would be a good choice for a reference resolution. Finally, we applied state-of-the-art automated fingerprint recognition algorithms to our collected fingerprint images. Via cross validation experiments, we found the recognition precision under resolution 700dpi~1,000dpi is one order of magnitude higher than that under other considered resolutions. The highest recognition accuracy in different fingerprint groups is almost always obtained under

800dpi. These results validate our proposed resolution from the point of view of automated fingerprint recognition accuracy.

2.2 Collecting Multi-resolution Fingerprint Images

According to our knowledge, there is no dataset of multi-resolution fingerprint images publicly available. We therefore collected a multi-resolution fingerprint image database by using our custom-built fingerprint image acquisition device. In this part, we introduce the fingerprint acquisition device and the established multi-resolution fingerprint image database.

2.2.1 Acquisition Device

A multi-resolution fingerprint acquisition device (or sensor) must be cost-effective but should in particular be able to acquire fingerprint images at multiple resolutions without any negative impact on the quality of the image [18]. There are generally three kinds of fingerprint sensors: solid-state, ultrasound, and optical [18, 19]. Solid-state sensors are small and inexpensive but cannot capture high resolution images [86]. Ultrasound sensors can capture high resolution images, but are usually bulky and expensive [25]. Optical sensors can capture a variety of different image resolutions, varying in a range of sizes and prices. They are easy to implement and have been found to have a high degree of stability and reliability [27]. Our system is thus equipped with an optical fingerprint sensor.

While there are also several different ways to implement optical fingerprint sensors, the oldest and most widely used way [18], and the way we have chosen to implement our sensor, is frustrated total internal reflection (FTIR). As shown in Fig. 2.2, an FTIR-based fingerprint sensor consists of a light source, a glass prism, a lens, and a CCD or CMOS camera. When users put their fingers on the surface of the glass prism, ridges absorb light and so appear dark whereas valleys and the fine details on ridges reflect light and thus appear bright. Different resolutions can be obtained by simply adjusting the distance between the glass prism and the lens and the distance between the lens and the camera.

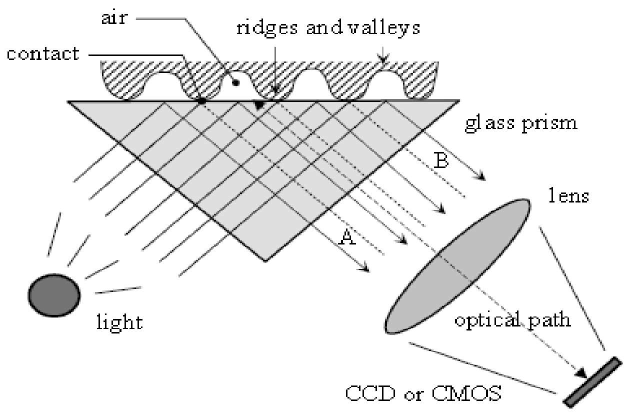

Fig. 2.2: Operation of an FTIR based fingerprint sensor [18].

2.2.2 Fingerprint Samples

The most commonly used fingers in fingerprint recognition are the thumb, index finger, and middle finger. These are also the fingers that we use for the images used in our experiments. We collected fingerprint images from both males and females. This is pertinent because male and female fingers are on average different in area and ridge width (or pore size). 25 males and 25 females contributed to our database. Four fingerprint images were captured from each of the six fingers (i.e. thumb, index and middle fingers on right and left hands) of them under each of the following resolutions: 500dpi, 600dpi, 700dpi, 800dpi, 900dpi, 1,000dpi, 1,200dpi, 1,600dpi, and 2,000dpi. As a result, there are totally 1,200 fingerprint images for each of the considered resolutions in the database. Fig. 2.3 shows some example fingerprint images collected from a male and a female.

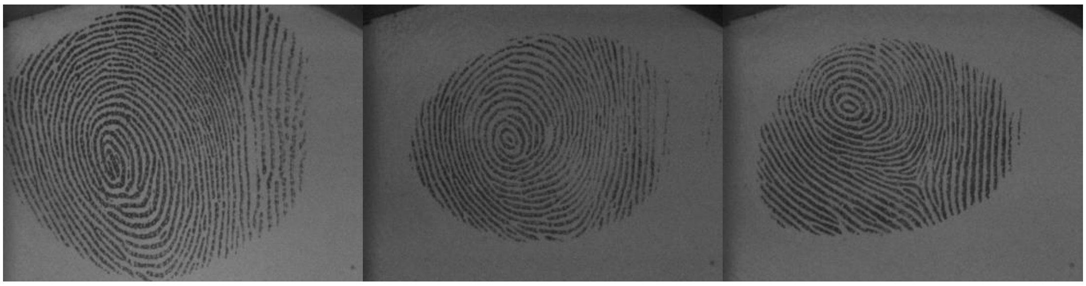

(a)

(b)

Fig. 2.3: Example 800dpi fingerprint images in our established database. (a) From a female and (b) From a male (From left to right: Thumb, Index finger and Middle finger).

2.2.3 Implementation of Multi-resolution

Three factors among others can affect the quality of a fingerprint image: its resolution, the measured area of the fingerprint that is captured or sensed, and the size of the image (the number of pixels). These factors are essentially not independent, but related with each other as follows:

$$H = 25.4 \times h / r,\ W = 25.4 \times w / r \tag{2.1}$$

where r denotes resolution, h and w denote the height and width of the image, and H and W denote the height and width of the captured area (in millimeters). To generate fingerprint images of different resolutions, one of the other two parameters must be fixed. Table 2.1 shows the values of H and W according to Eq. 2.1 at different resolutions when h and w are set as 640 and 480 pixels. It can be seen that at a fixed image size, the area captured by the image decreases as the resolution increases. Different resolutions can be easily obtained by adjusting the distances between the glass prism, the lens and the CCD. Fig. 2.4 shows some example fingerprint images at different resolutions.

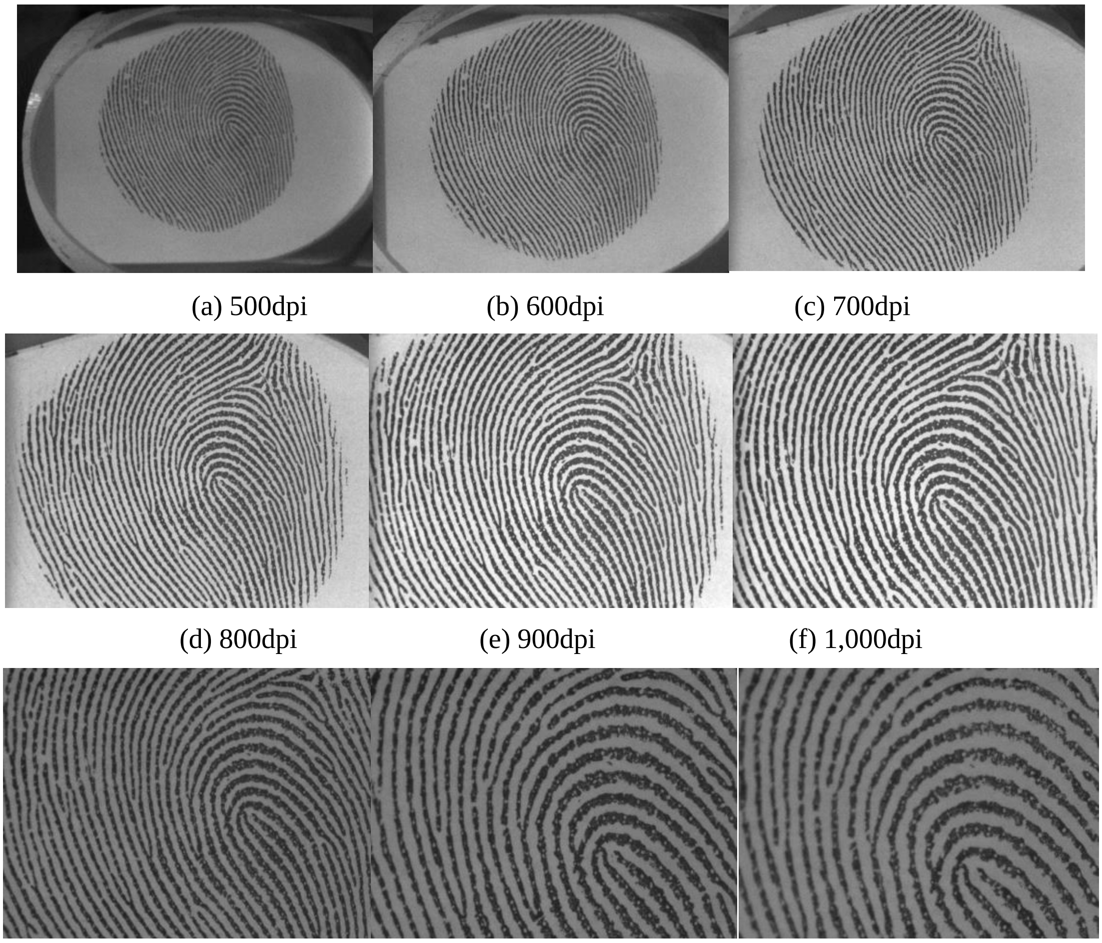

(a) 500dpi (b) 600dpi (c) 700dpi

(d) 800dpi (e) 900dpi (f) 1,000dpi

(g) 1,200dpi (h) 1,600dpi (i) 2,000dpi

Fig. 2.4: Example fingerprint images at different resolutions when using a fixed image size of 640*480 pixels.

Table 2.1: The values of *H* and *W* at various *r* when *h* and *w* are set as 640 and 480.

(*h*, *w*) (pixel)	***r* (dpi)**	**(*H*, *W*) (mm)**
(640, 480)	500	(32.5, 24.4)
	600	(27.1, 20.3)
	700	(23.2, 17.4)
	800	(20.3, 15.2)
	900	(18.1, 13.5)
	1,000	(16.3, 12.2)
	1,200	(13.6, 10.2)
	1,600	(10.2, 7.6)
	2,000	(8.1, 6.1)

It should be noted that the resolution of our device is not identical along the vertical and horizontal directions. This is because the CCD camera has a vertical resolution of 1,040 lines and a horizontal resolution of 1,394 lines. At 500dpi this is not a large difference and researchers usually ignore it. However, as the resolution increases, the difference between the vertical and horizontal resolutions becomes more obvious. For example, at vertical resolution 800dpi the horizontal resolution is 1,064dpi, but at vertical resolution 1,200dpi the horizontal resolution is 1,596dpi. The ratio between the horizontal resolution and vertical resolution equals to the one between the horizontal resolution and vertical resolution of CCD camera. Thus, given both vertical or horizontal resolution of fingerprint images and the parameters of CCD camera, we can calculate the resolution of fingerprint images along the other direction. For simplicity, in this chapter we refer just to the vertical resolution.

2.3 Selecting Resolution Criteria Using Minutiae and Pores

Generally, people may think that higher recognition accuracy can be achieved by increasing the resolution. It is true if the whole fingerprint region is covered. However, in practical AFRS, the fingerprint image size is usually confined to a relatively small one for the purpose of miniaturization and reducing the computational complexity. Until now, the most widely used image size in most chapters [68-75, 77-79, 85] or in most public fingerprint image databases such as the fingerprint verification competition (FVC) databases (e.g. FVC2000, FVC2002, FVC2004 and FVC2006) is 640*480 pixels. With a limited image size, the larger the resolution is, the smaller the captured fingerprint region. Although increasing the fingerprint image resolution can provide more fine details on fingerprints for fingerprint matching, it would degrade the fingerprint recognition accuracy if the loss of useful discriminative information (e.g. minutiae) due to decreased fingerprint areas dominates the newly emerged fingerprint details (e.g. pores). For instance, the fingerprint images of a fixed size might cover the whole fingerprint regions at low resolution, but capture only few ridges on the fingers at high resolution (see Fig. 2.4). Thus, in this chapter aiming at a balance between various fingerprint features (in particular, minutiae and pores) available on high resolution fingerprint images, we investigate the fingerprint distinctiveness and recognition accuracy at different resolutions when a fixed image size is adopted. It is also worth mentioning that noise caused by the skin condition or the amount of pressure applied by the finger [18] also plays an important role in the recognition performance of AFRS due to its influence on the quality of fingerprint images. However, it is a common issue to fingerprint images at all resolutions, and is thus out of the scope of the resolution selection work in this chapter.

Since 500dpi minutiae-based AFRS were taken as the baseline systems, we chose the fingerprint image size so that as many minutiae as possible are captured by the 500dpi fingerprint image, or in other words, it can cover the full fingerprint region. By experience, we used an initial image size of 640*480 pixels. As can be seen in Fig. 2.4, this size actually can capture the full fingerprint region at resolution of 500dpi and 600dpi as well. Thus, we cropped the foreground fingerprint regions on these 500dpi fingerprint images by using rectangles. The maximum width and height of these rectangles observed in the database are 380 and 360 pixels, which were finally taken as the image size for the fingerprint images captured under higher resolutions (i.e. 600dpi~2,000dpi in the experiments in this chapter). Such an image size, which may be comparable with the templates stored in most of existing minutiae-based AFRS, will be very helpful to realize the interoperability between different AFRS, which is one motivation of this chapter.

In order to utilize the minutiae and pores on fingerprints, it is necessary that we be able to robustly extract both of these features. Minutiae can be robustly extracted from images of 500dpi or above but pore extraction requires higher resolution images according to investigating most of the chapters about fingerprints' studies [12, 18-19, 50, 54, 57, 68-79, 85]. It thus became necessary to figure out what would be the minimum resolution needed to extract pore features. Intuitively, such a figure can be arrived at based on anatomical evidence, i.e. the possible smallest physical size of pores on fingers. We will discuss this in detail in Section 2.4.1.

We finally raised three criteria to select the image resolution for high-resolution AFRS by considering the followings:

1. Given a fixed image size, retain as many minutiae as possible while pores begin to be available.
2. The number of pores begins to decrease, and no other useful information but the position of pores will be conveyed, when resolution reaches a certain value.
3. Minutiae are more discriminative than pores if the same number of them is considered. Retain as many minutiae as possible while also retaining an acceptable number of pores.

We can better understand the rationale for the criteria by considering the images of an example finger shown in Fig. 2.5, whose image size is 380*360 pixels and resolution increases from 500dpi to 2,000dpi. The minutiae are the features of interest and are marked with red circles. The availability of pores also can be seen on these images. One may clearly observe the change of available minutiae and pores across these fingerprint images of different resolutions. Next, we introduce the three selection criteria in detail.

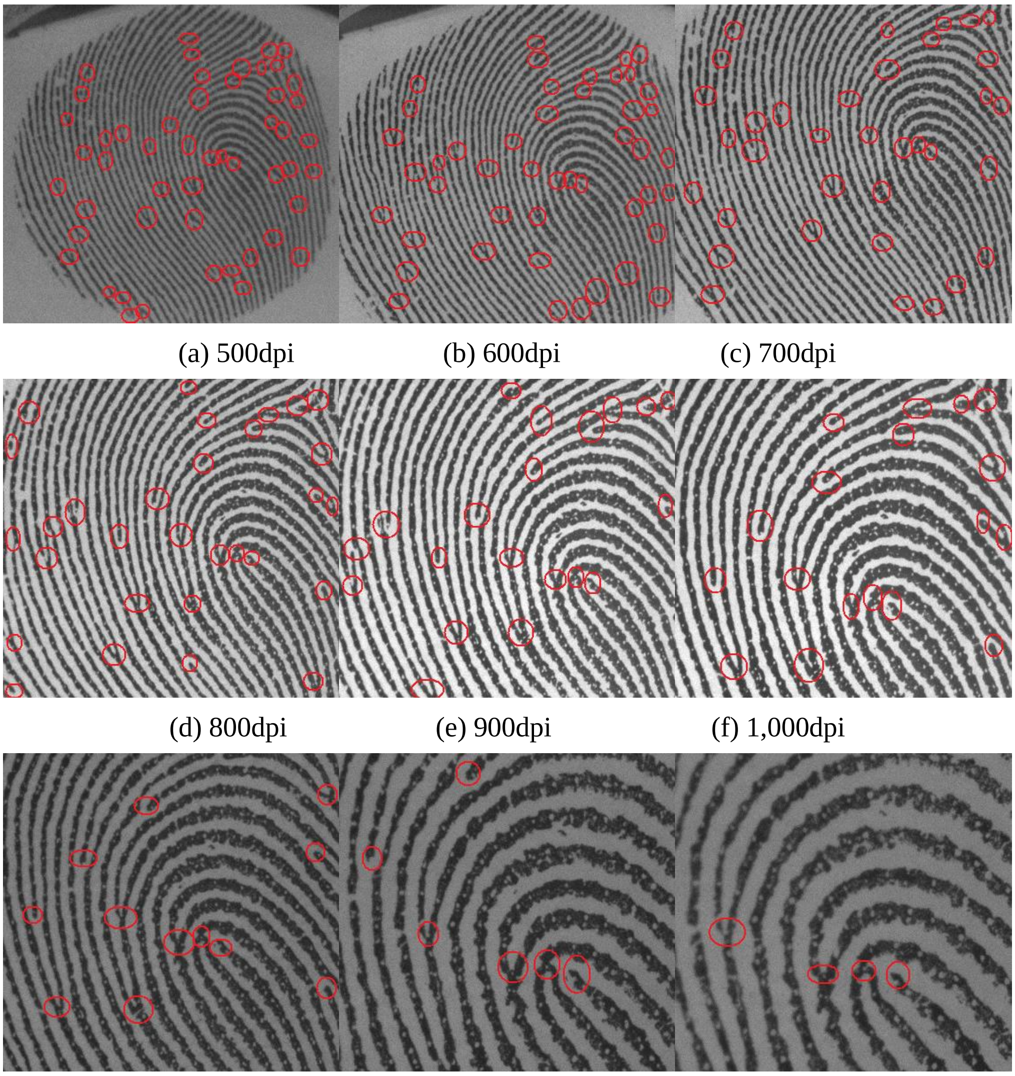

(a) 500dpi (b) 600dpi (c) 700dpi

(d) 800dpi (e) 900dpi (f) 1,000dpi

(g) 1,200dpi (h) 1,600dpi (i) 2,000dpi

Fig. 2.5: Minutiae and pores on fingerprint images of 380*360 pixels at different resolutions.

Criterion 1: Given a fixed image size, retain as many minutiae as possible while pores begin to be available. A lower limit image resolution can be obtained.

Most minutiae-based AFRS judge whether two fingerprints are from the same finger by counting the number of matched minutiae, basically the larger the number of minutiae is, the higher the possibility of making correct judgment. Thus, we should try to retain as many minutiae as possible. Table 2.2 lists the number of minutiae and pores in an image at different resolutions. As expected, the number of minutiae decreases as resolution increases. On the other hand, the number of pores first increases and then decreases as resolution increases. According to the analysis of Stosz and Alyea [54], there is a minimum resolution (larger than 500dpi) for robust pore extraction. As a consequence, the criterion 1 is established to determine the lower limit of resolution.

Table 2.2: Number of minutiae and pores in Fig. 2.5 at different resolutions.

r (dpi)	500	600	700	800	900	1,000	1,200	1,600	2,000
Num_minu	51	46	35	30	20	18	12	6	4
Num_pore	0	85	617	683	710	609	356	172	140

Criterion 2: The number of pores begins to decrease, and no other useful information but the position of pores will be conveyed when resolution reaches to a certain value. An upper limit image resolution can be obtained.

As can be seen in Fig. 2.5, the size and shape of pores become more visible at higher resolutions. However, according to [12, 69], usually only the location of pores is reliable discriminative information for fingerprint recognition; on the contrary, the size and shape of one pore can vary significantly from one impression to another. The two 2000dpi images in Fig. 2.6 are from the same finger but collected at different times. Clearly, the pores' size and shape (see the pores marked by red circles) are corrupted by noise or influenced by the condition of pores (open or closed). We thus set another criterion for resolution selection based on the number of pores at different resolutions, which can offer us the upper limit resolution.

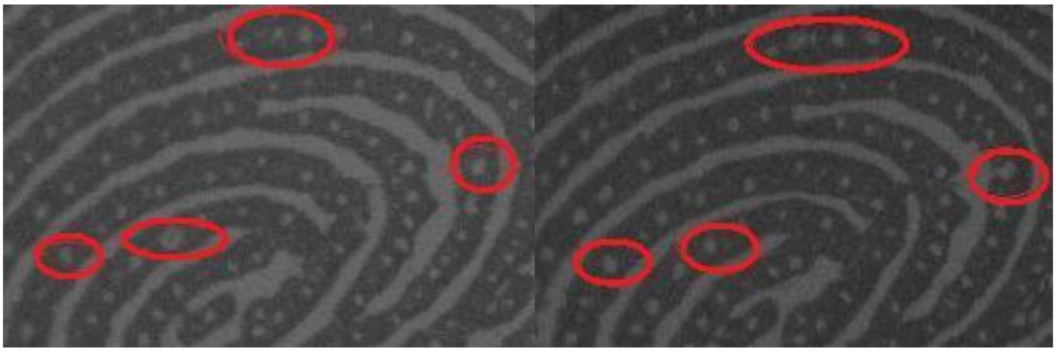

(a) (b)

Fig. 2.6: Two prints of one finger under 2,000dpi captured at different times.

Criterion 3: Minutiae are more discriminative than pores if the same number of each is considered. Retain as many minutiae as possible while also retaining an acceptable number of pores. A reference image resolution is then proposed.

Criteria 1 and 2 put emphasis on the number of minutiae and pores respectively, which just offer the lower resolution and upper resolution for high resolution AFRS. However, it is obvious that this will at times also require us to make some kind of tradeoff between the two. In this tradeoff, the bias will be towards retaining minutiae because the distribution of minutiae is more random than that of pores and so the number of minutiae in an image will have a greater influence on fingerprint recognition. The blue line on Fig. 2.7 links ten adjacent minutiae on a fingerprint image while the red line links adjacent pores. We can see that the blue line traverses approximately 1/3 of the entire fingerprint image while the red line is concentrated in just one area of about 1/100 of the fingerprint image. From this it would seem that if one or the other, minutiae or pores, must be traded off, then we lose less discriminative power if we bias towards retaining minutiae in the selection of a suitable resolution. We thus set our last criterion for resolution selection as retaining as many minutiae as possible while acceptable number of pores is available.

Note that all the above three criteria are about the number of minutiae and pores with a fixed image size. However, ridge width, which differs between different kinds of fingers (e.g. thumb, index finger and middle finger) [87] and between different genders (female and male) [88], also has some effect on the number of minutiae and pores for a fixed image size, and would consequently affect the selection of resolution. To make the reference resolution we selected based on the established criteria be universal to all fingers, it is necessary to study the relationship between ridge width and resolution. An analysis of ridge width on different kinds of fingers (e.g. thumb, index finger and middle finger) and on fingers from different genders (female and male) is conducted with respect to the resolution selected based on the established criteria. Section 2.4.3 will report the analysis result.

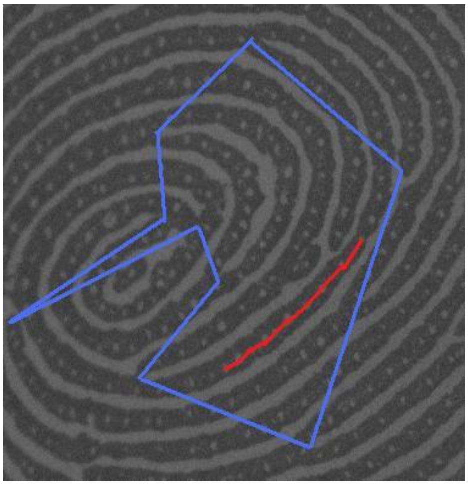

Fig. 2.7: The distribution of a similar number of minutiae and pores on a fingerprint image of 380*360 pixels.

2.4 Experiments and Analysis

To get a reference resolution based on our established criteria and to verify it, some analysis and experiments are organized as follows. Firstly, theoretical analysis of the minimum resolution for pore extraction is given. Secondly, the statistical number of minutiae and pores counted manually is offered. Thirdly, an analysis of ridge width on different kinds of fingers (thumb, index finger and middle finger) and on fingers of different genders (female and male) is given. Finally, the automated fingerprint recognition results of different resolution fingerprint images are provided.

2.4.1 Selecting the Minimum Resolution Required for Pore Extraction

There is a minimum resolution that is required to be able to extract pores well. In 1994, Stosz and Alyea [54] automatically extracted pores using a high resolution fingerprint sensor. They noted that pores could range in size from 60~250*um* in one dimension and that the smallest detectable pores, 60*um* in one dimension, determined the minimum resolution required by a sensor. They assumed a sampling period half the size of the smallest pore and concluded that the minimum required resolution of 800 dpi. In a later chapter, in 1997, Roddy and Stosz [69] talked about a range of pore sizes of 88~220*um*. Taking these two figures into account, in this work we use the average of these two minimum pore sizes.

To determine the minimum required resolution, we take the size of pores and the resolution and apply Eq. 2.1 to calculate the number of pixels in a pore. Then, based on the rule that the size of the smallest pores in one dimension can be down sampled [54], we know that the minimum resolution for pore extraction should guarantee that there are at least 2 pixels of the smallest pores in one dimension, as illustrated in Fig. 2.8. Table 2.3 shows the minimum values of height *h* for different resolutions. We can see that the minimum resolution required for pore detection is 700dpi when assuming a sampling period half the size of the smallest pores.

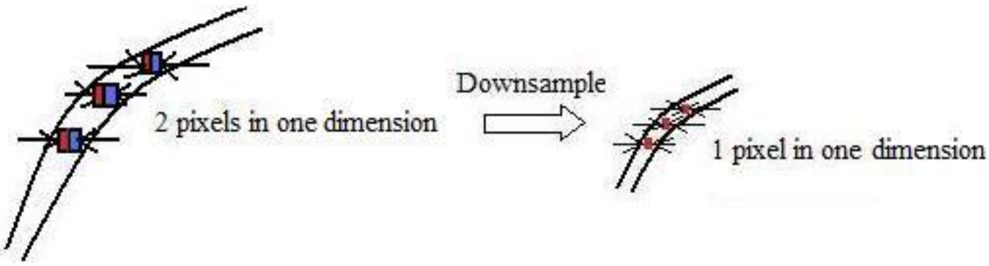

Fig. 2.8: The rule used to choose the minimum resolution for pore extraction.

Table 2.3: The minimum value of h of different resolutions.

Resolutions (dpi)	500	600	700	800	900	1,000	1,200	1,600	2,000
minimum value of h (pixel)	1.5	1.7	2.0	2.3	2.6	2.9	3.5	4.7	5.8

2.4.2 Selecting the Resolution based on the Established Criteria

Given a fixed image size, as resolution increases, the number of minutiae decreases and pores become more visible. We manually counted the numbers of minutiae and pores in the 120 fingerprint images at each resolution (500dpi~2,000dpi) at an image size of 380*360 pixels and then averaged these numbers. Fig. 2.9 shows the relationship between the numbers of minutiae and pores. We have exaggerated the number of minutiae tenfold for the purpose of display. We can see that the number of minutiae is monotonically decreasing but within an acceptable range from 500dpi to 1,000dpi and that a relatively large number of pores (statistical number by counting manually) is retained at resolutions in the range of 700dpi~1,000dpi. It would appear that the best choice of resolution for fingerprint recognition is 700dpi. However, given that 700dpi is the minimum resolution for pore extraction, we decided that in order to make the system more robust to noise, 800dpi would be a better choice.

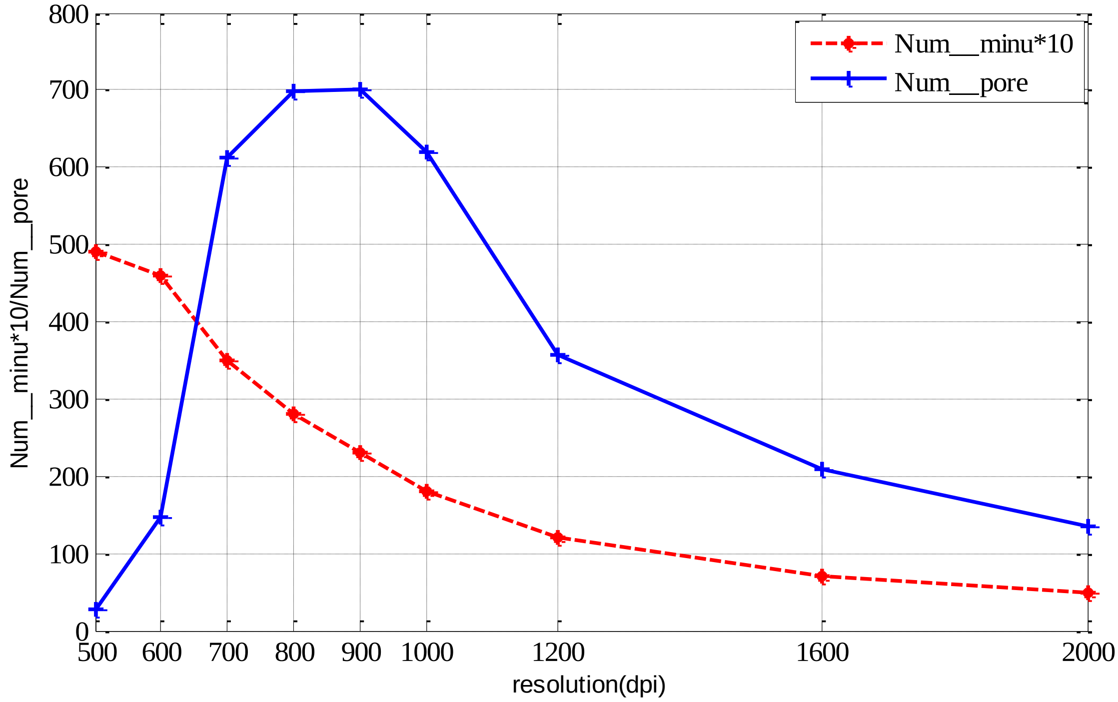

Fig. 2.9: Average numbers of minutiae and pores in 120 selected images in our database at different resolutions.

2.4.3 Analysis of Ridge Width

Since minutiae and pores are both related to fingerprint ridges, there is some influence of ridge width on the number of minutiae and pores. We thus did some analysis about the ridge width for different groups of fingers. Ridge width has been studied in [87, 88]. In [87], ridge width was determined by counting the ridges crossing transversely a line 1*cm*. In the chapter, the authors concluded that ridge width has little to do with body weight, stature, hand length, and so on. They also summarized that ridge width is different for different fingers even though not differs greatly. However, they did not discuss the relationship between ridge width and gender, for the reason that all the samples used in their chapter are from males. The relationship between ridge width and gender was studied in [88]. Ridge width in that chapter was decided by the ridge density, which counted the epidermal ridges on fingerprints with a 5*mm**5*mm* square drawn on transparent film. The authors of [88] concluded that women tend to have a statistically significant greater ridge density. Getting aware of the variation of ridge width, we also studied the ridge width on different kinds of fingers (e.g. thumb, index finger and middle finger) and on fingers from different genders (female and male) by using our collected fingerprint image database at the selected resolution 800dpi. The ridge density used in [88] is adopted here to determine the ridge width. In our database, there are 150 female fingers, 150 male fingers, 100 thumbs, 100 index fingers, and 100 middle fingers. Some descriptive statistics of dermal ridge densities as mentioned in [88] and the corresponding ridge width represented by both *um* (calculated by the following Eq. 2.2) and pixel (calculated by Eq. 2.1), are given for different groups of fingers in Table 2.4.

$$ridge\ width = sqrt(5^2 + 5^2) / \left(ridge\ density \times 2\right) \tag{2.2}$$

Here, the diagonal length of the 5*mm**5*mm* square is considered as the overall length of all ridge-valley period.

Table 2.4 shows the standard variation (SD), mean value (Mean), minimum value per person (Minimum) and maximum value per person (Maximum) of ridge density, as well as their corresponding ridge width on different groups of fingers. The results of different kinds of fingers (thumb, index finger and middle finger) in Table 2.4 show that there is little difference of ridge width between them, which agrees with the conclusion made in [87]. The results in Table 2.4 also show that the ridge width of females is generally smaller than that of males by 15*um* or 0.5 pixels. However, this difference is not significant (i.e. of sub-pixel level). Thus, we conclude that under resolution 800dpi, the ridge width had little influence on the number of minutiae and pores. It makes our proposed reference resolution be universal to all fingers.

Table 2.4: Descriptive statistics comparisons of ridge density and their corresponding ridge width on different group of fingers.

	Females	**Males**	**Thumb**	**Index Finger**	**Middle Finger**
Number of fingers	**150**	**150**	**100**	**100**	**100**
Mean (ridges/25 mm^2)	19.13	17.67	18	18.23	18.67
Corresponding ridge width (*um, pixel*)	(185, 5.8)	(200, 6.3)	(196, 6.2)	(194, 6.1)	(189, 6.0)
Minimum[a] (ridges/25 mm^2)	16.83	15.50	16.13	16.00	16.67
Corresponding ridge width (*um, pixel*)	(210, 6.6)	(228, 7.2)	(219, 6.9)	(220, 6.9)	(212, 6.7)
Maximum[a] (ridges/25 mm^2)	22.67	21.67	21.17	21.77	22
Corresponding ridge width (*um, pixel*)	(156, 4.9)	(163, 5.1)	(167, 5.3)	(162, 5.1)	(161, 5.1)
SD (Standard Variation)	**1.85**	**1.26**	**1.89**	**2.08**	**2. 16**

[a] Based on the average number of ridges/25 mm^2 per person [88].

2.4.4 Fingerprint Recognition Accuracy

To verify our choice of resolution and its relationship to accurate fingerprint recognition, we conducted a series of experiments using the fusion strategy presented in [71] by combining the state-of-the-art minutia-based method proposed in [50] and the pore-based method proposed in [71], evaluating recognition accuracy according to the Equal Error Rate (EER). Specifically, we did cross validation experiments by dividing all fingers into 3 groups according to the types of fingers (i.e. thumb, index finger, and middle finger, respectively), as well as by dividing all fingers into female and male groups. The recognition results by considering all the fingers included in our database were also given. The lower the value of EER is, the higher the recognition accuracy. Fig. 2.10 shows the EERs obtained at different resolutions on the six different groups of fingers and the mean EERs by averaging those EERs at different resolutions. For the thumb, index finger and middle finger groups, the EERs were obtained from 600 genuine scores (generated from 100 fingers, 4 pictures of each finger) and 4,950 imposter scores (generated from 100 fingers, comparing the first images of different fingers). For the female and male groups, the EERs were obtained from 900 genuine scores (generated from 150 fingers, 4 pictures of each finger) and 11,175 imposter scores (generated from 150 fingers, comparing the first images of different fingers). When considering all the fingers, the EERs were obtained from 1,800 genuine scores (generated from 300 fingers, 4 pictures of each finger) and 44,850 imposter scores (generated from 300 fingers, comparing the first images of different fingers).

Fig. 2.10 shows the EERs on different groups of fingers at different resolutions by fusing the state-of-the-art minutia-based method proposed in [50] and the pore-based method proposed in [71]. Specifically, the black line in Fig. 2.10 shows the recognition results when only males' fingers in our database are considered. The lowest EER is obtained when resolution is 700dpi. The red line in Fig. 2.10 shows the EER values at different resolutions when only females' fingers in our database are involved. The lowest EER is obtained when resolution is 900dpi.The gray line which represents the EERs when only thumbs are considered shows that the lowest EER can be obtained at the resolution of 700dpi. The rest of the lines in Fig. 2.10 all show that the lowest EER is achieved at the resolution of 800dpi. However, all of the results in Fig. 2.10 show that relatively lower EER can be obtained when the resolution is between 700dpi to 1,000dpi. A resolution of 800dpi can achieve the lowest EER in most cases and the lowest mean EER of the 6-fold experiments (pink line). This result further confirms our proposed reference resolution.

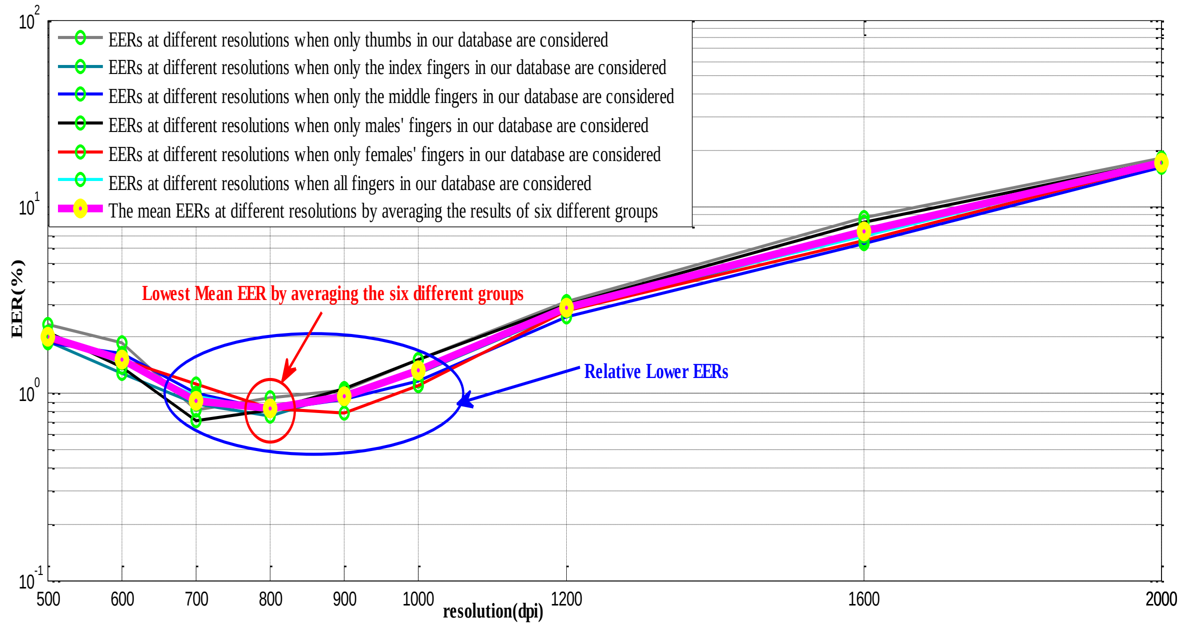

Fig. 2.10: EERs obtained at different resolutions on the six different groups of fingers and the mean EERs by averaging those EERs at different resolutions.

2.5 Summary

This chapter has proposed a method to select a reference resolution for use in high resolution AFRS based on minutiae and pores. We initially found that, based on anatomical evidence, a minimum resolution of 700dpi would give good results; but further analysis based upon an analysis of the number of minutiae and pores and the ridge width on different kinds of fingers and on fingers of different genders, as well as tests of comparative accuracy, has led us to recommend a reference resolution of 800dpi. While we regard this as an advance, we must point out that image size also has an important role in high resolution AFRS. In this chapter, we limited images to a size of 380*360 pixels so as to allow us to investigate only the impact of resolution. In future work, we will investigate how to best make the trade-off between the influences of resolution and image size within a certain range on high resolution AFRS, and to figure out does there exist a dynamic resolution to different image sizes for high resolution AFRS.

Chapter 3
A Novel Hierarchical Fingerprint Matching Approach

With the advent of high resolution fingerprint imaging techniques and the increasing demand for high security, sweat pores have been recently attracting increasing attention in automated fingerprint recognition. This chapter proposes a new fingerprint pore matching method to achieve higher recognition accuracy. This method directly matches pores in fingerprints by hierarchical strategy. In the step of coarse matching, a tangent distance and sparse representation based matching method (denoted as TD-Sparse) is used to compare pores in the template and test fingerprint images and establish one-to-many pore correspondences between them. The proposed TD-Sparse method is robust to noise and distortions in fingerprint images. In the step of fine matching, false pore correspondences are pruned by a weighted RANdom SAmple Consensus (WRANSAC) algorithm. The weights of pore correspondences are determined based on the dis-similarity between the pores in the correspondences. The chapter is organized as follows. Backgrounds and literature reviews are described in section 3.1. We introduces the establishment of one-to-many coarse pore correspondences by the TD-Sparse based matching method in the following section 3.2. Section 3.3 presents the WRANSAC algorithm that we have adopted in the fine matching step, and describes in detail the calculation of the weights used in WRANSAC. Section 3.4 then reports the experiments and analyzes the results. Finally, section 3.5 summarizes this chapter.

3.1 Introduction

Fingerprint matching is an important and essential step in AFRSs. It aims to offer a degree of similarity (value between 0 and 1) or a binary decision (matched or non-matched) between two given fingerprint images (template and test fingerprints). Generally, such fingerprints are not compared directly but based on the representation of them, such as minutiae, sweat pore, ridge contour and so on [73], as shown in Fig. 3.1. Because of noise and distortion introduced during fingerprint capture and the inexact nature of feature extraction, there are errors in the fingerprint representation (e.g. missing, spurious, or noisy features). Therefore, the matching algorithm should be robust to these errors. As the advent of high resolution fingerprint imaging techniques, new distinctive features, such as sweat pores, ridge contours, ridge edge features, are attracting increasing attention from researchers and practitioners who are working on AFRSs. They also have been proven to be very useful for improving the accuracy of existing minutiae-based AFRSs [54, 68, 69, 71, 75, 76]. Sweat pores, among various new features, have attracted the most attention [54, 68, 69, 71, 75-79, 89]. Some effective pore extraction methods have been proposed in [77-80, 89]. However, there are few algorithms for pore matching [68, 71, 75, 76]. The errors mentioned above make fingerprint pore matching very challenging. Thus, this chapter takes fingerprint pore matching as an example to introduce our proposed robust fingerprint matching method.

Existing pore matching methods can be roughly divided into two categories. Methods in the first category align the fingerprint images before matching the pores in them [68, 75, 76]. Various methods have been proposed for the alignment. Kryszczuk et al. [68] first aligned the test fragmentary fingerprint with the full template fingerprint using the image-correlation based method, and then matched the pores in the aligned fingerprint images based on their geometric distances. This method has the following two drawbacks: 1) it is time consuming to obtain the best alignment in a quantized transformation parameter space by trying all possible rotations and translations, and 2) recognition accuracy heavily relies on the alignment accuracy and is sensitive to the instability of extracted pores and nonlinear distortions in fingerprint images. Jain et al. [75, 76] proposed a minutiae-based method. The fingerprint images are first aligned by using minutiae. Then, pores lying in a rectangular neighborhood to each aligned minutiae pair are matched using a modified iterative closest point (ICP) algorithm. This method is more efficient than that in [68]. However, it requires a sufficient number of minutiae for effective alignment and considers only the pores in a small neighborhood of aligned minutiae.

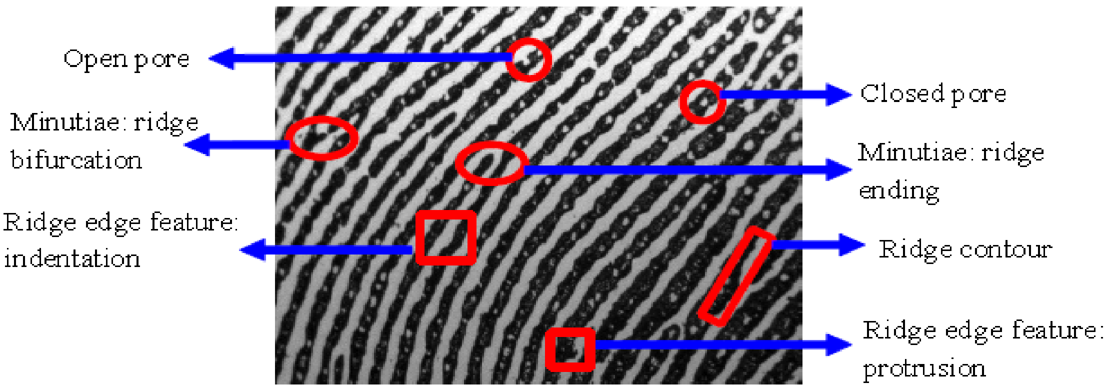

Fig. 3.1: Features on a high resolution fingerprint image.

Methods in the second category directly match pores in fingerprints without explicit alignment of the fingerprint images. In [71], Zhao et al. proposed a hierarchical coarse-to-fine pore matching scheme. In the coarse step, one-to-one pore correspondences are roughly determined based on the correlation between the local patches around the pores. In the fine step, the obtained pore correspondences are further refined using a global transformation model. This method has the advantage of robustness to the instability of extracted pores by considering all the available pores in fingerprint images. However, it still has some limitations. 1) The correlation between local patches can be not discriminative enough to ensure that the similarity between a pore and its true corresponding pore is always higher than that between it and the other pores. For example, when the local patches mainly consist of parallel ridges or when they are very noisy or heavily distorted, true pore correspondences could have their similarity ranked not at the top. As a consequence, considering only the top 1 pore correspondences is very likely to miss many true correspondences. 2) Not all the pore correspondences established at the coarse step have the same reliability. Instead, the similarity between the pores in different correspondences can be quite different, and those correspondences with higher similarity are generally believed to be more reliable. Therefore, the similarity of the correspondences provides a natural indicator of their reliability. Yet, previous pore matching methods [71, 89] did not explore this information.

In this chapter, we propose a novel hierarchical matching method, namely TDSWR, which is less sensitive to the instability of pores and gets rid of the above-mentioned limitations of existing pore matching methods. Compared with existing pore matching methods, the proposed method has the following characteristics: 1) a tangent distance and sparse representation based matching method (TD-Sparse), which is robust to noise and distortion, is proposed to determine the pore correspondences at the coarse step; 2) one-to-many pore correspondences are established at the coarse step, and thereby most of the true pore correspondences are retained in the results of coarse matching; and 3) a weighted RANdom SAmple Consensus (WRANSAC) algorithm [90] which explores the reliability information of pore correspondences, is employed in the fine matching step to exclude false pore correspondences. Fig. 3.2 gives the framework of the proposed method.

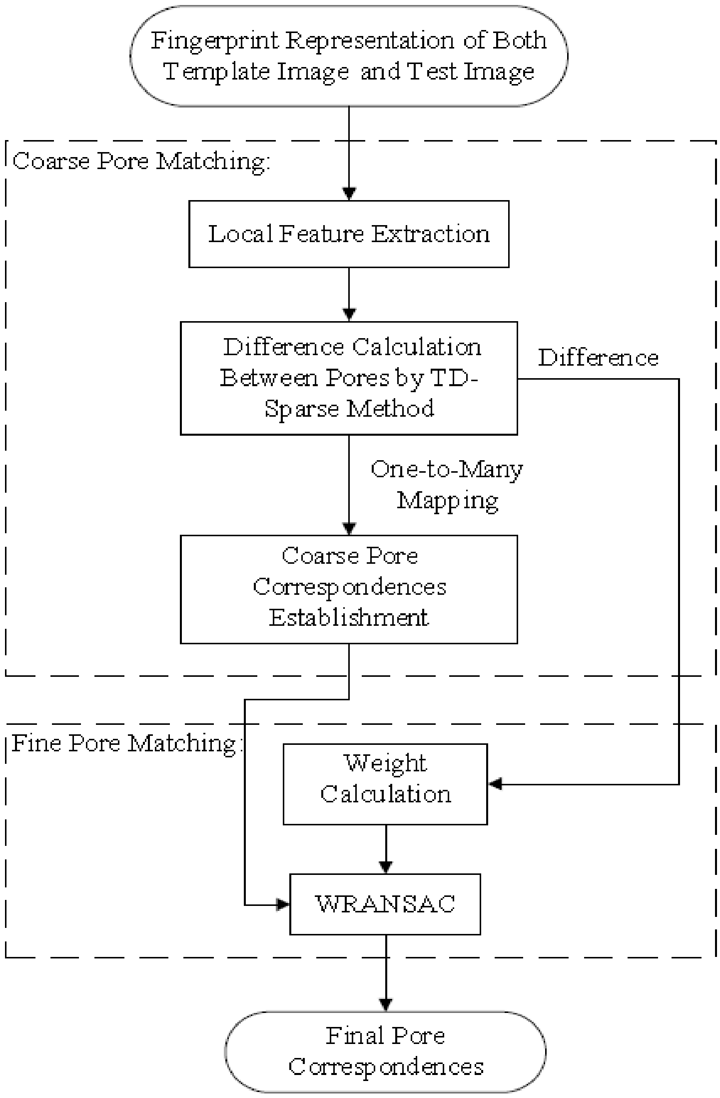

Fig. 3.2: Framework of the proposed TDSWR method.

3.2 Coarse Pore Matching

A key issue in establishing coarse pore correspondences is to calculate the similarities or differences between individual pores. Unlike existing methods [71, 89], this chapter proposes a TD-Sparse based method, which is more robust to noise and distortion [95-99], to calculate the differences between pores and establish one-to-many pore correspondences in the coarse pore matching step.

A local descriptor is first constructed for each pore. Here, we use the same local descriptor as in

[71] so that we can fairly compare the proposed TD-Sparse based approach and the correlation-based approach in [71]. The local descriptor of a pore essentially captures the intensity variation in a circular neighborhood to the pore. To construct the local descriptors, the original fingerprint image is first smoothed by a Gaussian filter. Then, a circular neighborhood to each pore is cropped and rotated to keep the local ridge orientation at the pore horizontal. Finally, the intensity values of the pixels in the neighborhood are concatenated and normalized to form the local descriptor of the pore.

3.2.1 Difference Calculation by TD-Sparse Method

To calculate the differences between pores, this chapter uses the sparse representation technique rather than the correlation-based technique. Sparse representation was originally developed in signal/image modeling to solve inverse problems [91, 92] and began to be practically used with the development of theory and algorithms of techniques [93, 94]. Wright et al. [95] have recently proposed the sparse representation classifier (SRC) for robust face recognition, and obtained promising results. The basic idea of SRC is to represent an input sample by a linear combination of a set of training samples, in which the combination coefficients are restricted to be sparse. It conducts classification based either on the assumption that the coefficients corresponding to the samples of the same class have larger absolute values or on the assumption that the residual of representing the input sample with the samples from the same class is smaller. The procedure of the SRC algorithm is given in Algorithm 3.1. From the similarity measurement viewpoint, the coefficient associated with a training sample indicates the similarity between this training sample and the input sample, whereas the residual by each class implies the difference between the input sample and the samples in that class. According to the results in [95], the residuals are more robust to noise than the coefficients. Therefore, in this chapter, the differences between pores are measured by the residuals in sparse representation.

Euclidean distance (ED) is used in [95] to calculate the residuals of sparse representation (see Algorithm 3.1). As a result, the SRC in [95] is sensitive to local distortion, which is however very common in fingerprint images [63]. Therefore, for fingerprint pore matching, we propose to incorporate the tangent distance (TD) into the SRC to make it more robust to distortion.

Algorithm 3.1: The SRC algorithm [95].

1: **Input:** A set of training samples $A = [A_1, A_2, \cdots, A_k] \in R^{m \times n}$ of k classes and their class labels, a test sample $y \in R^m$, as well as an error tolerance $\varepsilon > 0$, or a free parameter $\lambda > 0$ to balance the least squares error of representation and the sparsity of the coefficients.

2: Normalize the columns of *A* to obtain unit l_2-norm .

3: Solve the l_1-regularized least squares problem (LSP):

$$\hat{x} = \arg\min_x \left\{ \|Ax - y\|_2^2 + \lambda \|x\|_1 \right\} \tag{3.1}$$

4: Calculate $\delta_i(x) \in \Re^n$, which is a vector whose only nonzero entries are the entries in *x* that are associated with class *i*.

5: Compute the residuals: $r_i(y) = \left\| y - A\delta_i\left(\hat{x}\right) \right\|_2$ $for \;\; i = 1, \ldots, k$.

6: **Output:** The category of test sample:

$$\text{identity}(y) = \arg\min_i r_i(y)$$

TD is a distance measure first proposed by Simard et al. [96] for optical character recognition (OCR). It is very effective in handling distortion problems in distance-based classification algorithms. As illustrated in Fig. 3.3, if ED is used for classification (the Pearson correlation between Fig. 3.3(a) and Fig. 3.3(b) (or Fig. 3.3(c)) is 0.92 (or 0.97) if the ED is used), the fingerprint pattern in Fig. 3.3(a) will be misclassified into prototype B in Fig. 3.3(c), but not the true prototype A with slight distortion in Fig. 3.3(b). On the contrary, TD can easily solve this problem (the Pearson correlation between Fig. 3.3(a) and Fig. 3.3(b) (or Fig. 3.3(c)) is 0.99 (or 0.92) if the TD is used) thanks to its ability to make the input pattern locally invariant to any deformation [96]. In [96], it has also been demonstrated that TD, compared with ED, is closer to the real distance between two patterns in 3-dimensional space.

(a) (b) (c)

Fig. 3.3: Examples of fingerprint segments to illustrate the effectiveness of TD compared with ED. (a) A fingerprint pattern that needs to be classified. (b) The prototype A, which is formed by rotating (a) by 10 degrees and then translating it to the left side by 5 pixels. (c) The prototype B, which represents a fingerprint pattern different from (a).

However, it is difficult to exactly calculate the TD between two patterns. As there is no analytic expression for the manifolds of the patterns, an approximation method has to be adopted. In the following, we provide a procedure [97, 98] to calculate the TD between two images, *x* and *y*. For the image $x \in \Re^{I \times J}$ (*I* and *J* represent the numbers of rows and columns, respectively), its corresponding manifold is obtained by applying transforms, $t(x, \beta)$, to it:

$$M_x = \left\{ t(x, \beta) : \beta \in \Re^{\mathrm{C}} \right\} \subset \Re^{\mathrm{I \times J}} \tag{3.2}$$

where $\beta \in \Re^{C}$ are the parameters of the transformation, and *C* is the number of transformation parameters. The approximated manifold is then calculated by Taylor expansion at $\beta = 0$:

$$\hat{M}_x = x + \sum_{k=1}^{C} \beta_k \left. \frac{\partial x}{\partial \beta_k} \right|_{\beta_k = 0} + \sum_{k=1}^{C} \mathrm{O}\left(\beta_k^{\ 2}\right) \tag{3.3}$$

where vector $v_k = \left. \dfrac{\partial x}{\partial \beta_k} \right|_{\beta_k = 0}$ is called the tangent vector. The TD between images *x* and *y* is calculated as follows:

$$TD(x,y)=\min_{\beta_k}\left\{\left\|x+\sum_{k=1}^{C}\beta_k v_k-y\right\|_2^2\right\} \tag{3.4}$$

where the tangent vectors $\{v_k\}$ can be either single sided (SD) tangent vectors, i.e. the derivative with respect to *x* or *y*, or double sided (DD) tangent vectors, i.e. the derivative with respect to both *x* and *y*.

By substituting the ED in the LSP objective function with the above TD, we get the following new objective function of the proposed TD-Sparse method:

$$\hat{x}=\arg\min_x\left\{\min_{\beta_k}\left\|Ax-\left(y+\sum_{k=1}^{C}\beta_k v_k\right)\right\|_2^2+\lambda\|x\|_1\right\} \tag{3.5}$$

Although Eq. 3.5 seems to be a two-step optimization problem, we can solve it as a classical one-step convex optimization problem by combining *A* and $\{v_k\}$ if single sided tangent vectors from the *y* side are used here. In this way, Eq. 3.5 is modified as the following l_1-regularized LSP:

$$\hat{x}'=\arg\min_{x'}\left\{\|A'x'-y\|_2^2+\lambda\|x'\|_1\right\} \tag{3.6}$$

Here, $A'=[A\ \ v_1\ \ v_2\ \ \cdots\ \ v_L]$, L is the number of tangent vectors. Those tangent vectors $[v_1\ v_2\cdots v_L]$ are formed by the differences between y and the transformations of y (rotated, translated or scaled). $x'=[x\ \ \alpha_1\ \ \alpha_2\ \ \cdots\ \ \alpha_L]$, and the length of vector x' becomes $n+L$. $[\alpha_1\ \alpha_2\cdots\alpha_L]$ are the coefficients of tangent vectors after Taylor expansion. This objective function based on TD can be easily solved by using the same method in solving Eq. 3.1. Next, we apply the above proposed TD-Sparse method to calculating the difference between pores.

Given input and template fingerprints: *S* and *T*, denote the descriptors of the pores in them by $p^S=\{p_1^S, p_2^S,\cdots p_n^S\}$ and $p^T=\{p_1^T, p_2^T,\cdots p_m^T\}$, where *n* and *m* are the number of pores in the input and template fingerprints, respectively. In order to calculate the difference between each hpore in *S* and each pore in *T*, we take each pore in *T* as a class, and for each pore in *S*, we use the linear combination of all the pores in *T* to approximate it under the sparse representation constraint. According to Eq. 3.6, the sparse representation coefficients $x_j = \{x_{j1}, x_{j2}, \cdots, x_{jm}\}$ for the j^{th} ($j = 1, 2, \cdots n$) pore p_j^S in *S* can be obtained by solving

$$x_j' = \arg\min\left\{\left\|A'x_j' - p_j^S\right\|_2^2 + \lambda\sum_{i=1}^{m}\left|x_{ji}'\right|\right\} \tag{3.7}$$

where $A' = \begin{bmatrix} A & v_1 & v_2 & \cdots & v_L \end{bmatrix}$, *A* is the basis matrix whose columns are the local descriptors of the pores in *T*. $x_j' = [x_j \quad \alpha_1 \quad \alpha_2 \quad \cdots \quad \alpha_L]$. Because non-linear distortions of fingerprints can be locally approximated by linear distortions, we apply the following transformations to p_j^S to generate v_k ($k = 1, 2, \cdots L$): translation by [-4:2:4] pixels, rotation by [$-9^\circ : 3^\circ : 9^\circ$] and scaling by [0.8:0.2:1.2]. We use the method proposed by [94] to solve Eq. 3.7. Based on the obtained representation coefficients, we can calculate the difference between the j^{th} ($j = 1, 2, \cdots n$) pore in *S* and the i^{th} ($i = 1, 2, \cdots m$) pore in *T* as follows:

$$d_{ji} = \left\| p_i^T x_{ji} - p_j^S - \sum_{k=1}^{L} \alpha_k v_k \right\|_2 \tag{3.8}$$

3.2.2 Coarse Pore Correspondence Establishment

Coarse pore correspondences are established based on the above calculated differences between pores. Fig. 3.4 plots the histograms of the differences between 100 pairs of genuine pores (i.e. the same pore in different impressions) and between 100 pairs of imposter pores (i.e. different pores). Obvious overlap can be seen in Fig. 3.4. This indicates that true pore correspondences can have larger differences than false pore correspondences. Fig. 3.5 shows two example pores, whose true corresponding pores differ more from them than another two false corresponding pores because there are mainly parallel ridges in their local neighborhood. Therefore, in order to retain as more true pore correspondences in the coarse matching results as possible, we propose to establish one-to-many coarse pore correspondences as follows.

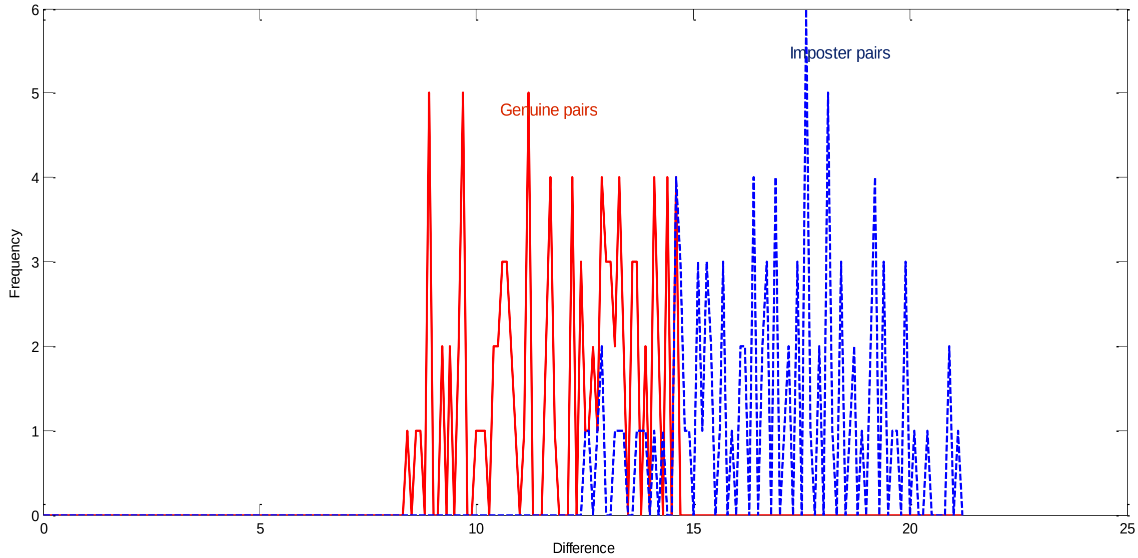

Fig. 3.4: Histograms of the differences between 100 genuine pore pairs and between 100 imposter pairs.

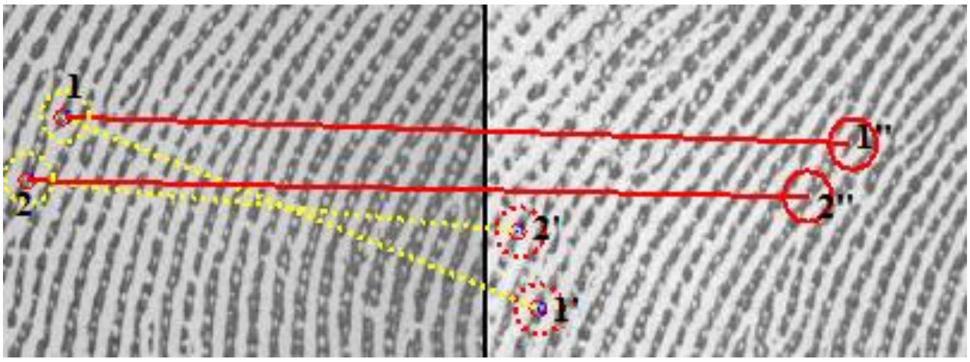

(a) (b)

Fig. 3.5: Two example fingerprint segments from the same finger which mainly consist of parallel ridges. The differences between the two pores (1 and 2) marked in (a) and their true corresponding pores in (b) (1" and 2", marked by solid circles) are larger than the differences between them and another two false corresponding pores in (b) (1' and 2', marked by dashed circles).

Given the pair-wise differences between the pores in *S* and the pores in *T*, i.e. $\{d_{ji} \mid j=1,2,\cdots,n; i=1,2,\cdots,m\}$, the minimum difference between each pore in *S* and the pores in *T* is first calculated, denoted as $d_j^{\min} = \min_i \{d_{ji} \mid i=1,2,\cdots,m\}$ ($j=1,2,\cdots,n$). The average of these minimum differences is then computed, i.e. $\bar{d} = \frac{1}{n}\sum_{j=1}^{n} d_j^{\min}$. Finally, all the pairs of pores whose differences are smaller than $\bar{d}$ compose the set of coarse pore correspondences, i.e.

$$\left\{ \left(P_l^S , P_q^T \right) \middle| \, d_{lq} < \bar{d} \right\} \tag{3.9}$$

In this way, one pore can have more than one corresponding pores in the coarse matching results. In other words, one-to-many pore correspondences are established. Fig. 3.6(a) shows the coarse pore correspondences between two example fingerprint images which are from the same finger.

3.3 Fine Pore Matching

Fine pore matching is applied to remove the false pore correspondences in the coarse pore matching results. In [71], a classical RANSAC algorithm is employed. RANSAC [100] outperforms the ICP method, another popularly used method in pore matching [75, 76], in its insensitivity to coarse alignment and outliers. It mainly includes two steps which are repeated in an iterative fashion. First, the minimal sample sets (MSSs) are randomly chosen from the dataset, and the parameters of the assumed global transformation model are estimated based on MSSs. Second, the other data in the dataset are checked to determine whether they are consistent with the model obtained from the first step. The consistent pairs form the consensus set (CS). RANSAC terminates when the probability of finding a better ranked CS drops below a certain threshold. The selection of MSSs seriously affects the accuracy and efficiency of RANSAC [101]. However, in the classical RANSAC algorithm, all samples in the dataset are chosen with the same probability and without regard to the relative reliability of different samples.

As shown in Fig. 3.4, even though there are overlap between the pore differences in genuine and imposter pairs, smaller differences generally indicate that the pore correspondences are more likely resulted from genuine pairs. Therefore, the difference between the pores in a pore correspondence naturally serves as a measure of the reliability of the correspondence. By selecting pore correspondences based on their reliability, we are enabled to more efficiently find true pore correspondences. To implement this, we adopt the Weighted RANSAC (WRANSAC) for fine pore matching. We choose pore correspondences according to the differences between the pores in the correspondences such that the pore correspondences with smaller differences are chosen with a higher probability than those with larger differences. In other words, the pore correspondences with smaller differences are assigned with larger weights. The weights of the pore correspondences are calculated in the following way. Let d_{max} be the maximum difference between all pores on the two fingerprints, i.e. $d_{\max} = \max\{d_{ji} \mid j = 1,2,\cdots n; i = 1,2,\cdots, m\}$. The weight w to the pore correspondence $\left(P_l^S, P_q^T\right)$ is then defined by

$$w = 1 - \frac{d_{lq}}{d_{\max}}, \quad d_{lq} < \bar{d} \tag{3.10}$$

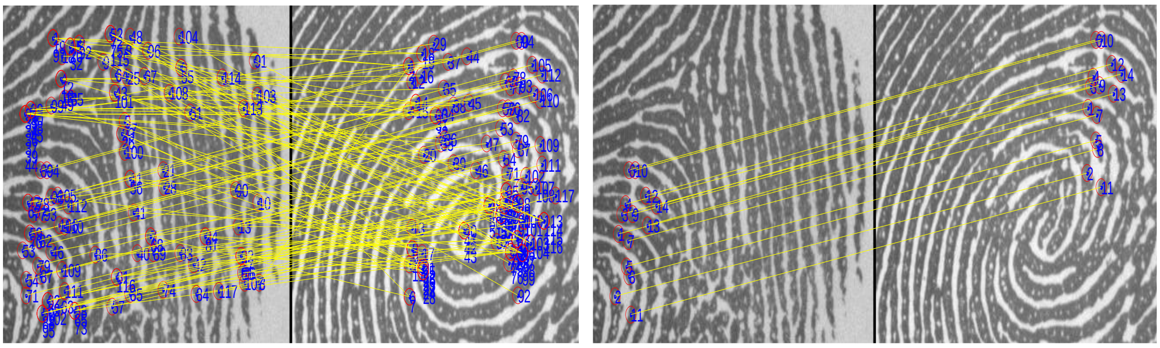

(a) (b)

Fig. 3.6: Example pore matching results. (a) Coarse pore correspondences in two fingerprint images by the TD-Sparse based method. (b) Refined pore correspondences in the two fingerprint images by WRANSAC.

Algorithm 3.2: The proposed TDSWR pore matching algorithm.

1: **Input:** Training samples A' consist of the pores in the template fingerprint T and their tangent vectors $[v_1\ v_2 \cdots v_L]$, test sample p_i^T from the input fingerprint S, a free parameter $\lambda > 0$ to balance the least squares error of representation and the sparsity of the coefficients.

2: Solve the modified l_1-regularized least squares problem (MLSP):

$$x_j' = \arg\min \left\{ \left\| A' x_j' - p_j^S \right\|_2^2 + \lambda \sum_{i=1}^{m} \left| x_{ji}' \right| \right\}$$

3: Calculate the difference between the j^{th} ($j = 1, 2, \cdots n$) pore in S and the i^{th} ($i = 1, 2, \cdots m$) pore in T:

$$d_{ji} = \left\| p_i^T x_{ji} - p_j^S - \sum_{k=1}^{L} \alpha_k v_k \right\|_2$$

4: Establish coarse pore correspondences:

$$\left\{ \left(P_l^S, P_q^T \right) \middle| d_{lq} < \bar{d} \right\}$$

$$\bar{d} = \frac{1}{n} \sum_{j=1}^{n} d_j^{\min}$$

$$d_j^{\min} = \min_i \{ d_{ji} \mid i = 1,2,\cdots,m \}, \quad j = 1,2,\cdots,n .$$

5: Refine coarse pore correspondences by using WRANSAC algorithm:

(a) Weight calculation for each coarse pore correspondence:

$$w = 1 - \frac{d_{lq}}{d_{\max}}, \quad d_{lq} < \bar{d}, \quad d_{\max} = \max\{ d_{ji} \mid j = 1,2,\cdots n; i = 1,2,\cdots,m \}$$

(b) Selection of MSSs according to weight.

(c) Model parameter calculation and affine transformation of coarse pore pairs on template fingerprint.

(d) CS establishment.

(e) Final refined pore correspondences once the termination conditions are reached, otherwise, go to step (b).

6: **Output:** Final refined pore correspondences:

$$\left\{ \left(P_x^S, P_y^T \right) \mid x \in l, y \in q \right\}$$

Pore correspondence refinement by WRANSAC proceeds as follows. First, we choose three pairs of corresponding pores to form the MSSs, because we assume that an affine transformation occurs to the fingerprints, and three pore pairs are sufficient to determine the six parameters of an affine model. The MSSs are chosen according to the weights of the pore correspondences. Based on the chosen MSSs, we estimate the six parameters of the affine model by solving a set of linear equations.

Second, we calculate the CS among the coarse pore correspondences under the estimated model parameters. Specifically, the pores in the template fingerprint are transformed according to the obtained model parameters. Then, the distances between them and the pores in the test fingerprint are calculated. The pore pairs whose distances are below a given threshold are taken to be matched. A coarse pore correspondence is taken as an element in the CS if the two pores in the correspondence are still matched after transformation.

The above two steps are repeated until either of the termination conditions is satisfied, and the refined pore correspondences can be obtained once the termination conditions are reached. In this chapter, the same two termination conditions as in [71] are used, i.e. the maximum number of iterations N_m (in our experiments, $N_m = 1,000$) and the sufficient number of iterations N_s. The sufficient number of iterations is given by:

$$N_s = \log(1-p) / \log\left(1-(1-\varepsilon)^3\right) \tag{3.11}$$

where *p* is the probability that at least one chosen correspondence set MSSs in the iterations is free from false pore correspondences (i.e. outliers), and ε is the percentage of outliers over the entire set of coarse correspondences with respect to the transformation obtained in the current iteration. *p* is set by experience (in our experiments, *p*=0.99). ε is closely related to the selection of MSSs. Because pore correspondences with smaller differences are more likely to be the correct correspondences, selecting MSSs based on the above defined weights enables a faster selection of the correct MSSs, which then gives a lower percentage of outliers, i.e. a smaller ε. According to

Eq. 3.11, less iteration is then required, i.e. N_s is smaller.

Thanks to the WRANSAC algorithm and the weights we proposed, the above fine pore matching method can find true pore correspondences not only more efficiently, but also more effectively. Fig. 3.6(b) gives the final pore correspondences obtained from applying WRANSAC to the coarse pore correspondences shown in Fig. 3.6(a), in which many false pore correspondences are successfully removed. Algorithm 3.2 summarizes the proposed TDSWR pore matching method.

3.4 Experimental Results and Analysis

3.4.1 Databases

Two databases of high resolution fingerprint images were used in the experiments. The first database, denoted as DBI, is the same database as the one used in [71], which contains 1,480 fingerprint images from 148 fingers (five images collected for each finger in each of two sessions separated by a time period of about two weeks). The images in DBI have a spatial size of 320 pixels by 240 pixels which covers a small fingerprint area (about 6.5 mm by 4.9 mm on fingertips). The fingerprint images in the second database (denoted as DBII) were collected in the same way, but with a larger image size, i.e. 640 pixels by 480 pixels. Pores in these fingerprint images were extracted by using an improved version of the algorithm in [70].

To compare the fingerprint recognition accuracy of the proposed TDSWR method and state-of-the-art methods, including the minutiae and ICP based method [75, 76] (denoted by MICPP), direct pore matching method [71] (denoted by DP), and classical SRC based pore matching method (denoted by SRDP) we proposed in [162], we conducted the following matches for each method on both DBI and DBII. 1) Genuine matches: each of the fingerprint images in the second session was matched with all the fingerprint images of the same finger in the first session, resulting in 3,700 genuine match scores. 2) Imposter matches: the first fingerprint image of each finger in the second session was matched with the first fingerprint images of all the other fingers in the first session, resulting in 21,756 imposter match scores. Note that the pore match scores in our experiments were defined as the number of pairs of final matched pores in fingerprints, which was different from the one used in [71]. Based on the obtained match scores, the equal error rates (EER) were calculated for each method.

3.4.2 Robustness to the Instability of Extracted Pores

In fingerprint pore matching, the instability of pores caused by fingerprint quality (dry or wet) is a crucial issue because it seriously affects the matching results. Fig. 3.7(a) shows the extracted pores (marked by red dots) in two fingerprint images captured from the same finger at different times. We can see that some pores do not show up which makes fingerprint pore matching a challenging problem. MICPP only matches the pores that are included in a neighborhood (circled in Fig. 3.7(a)) to each aligned and matched minutiae pair (connected by lines in Fig. 3.7(a)). It is thus sensitive to the instability of pores because the number of reproduced pores in a small region is obviously smaller than that in a large region. On the contrary, TDSWR directly matches pores in a hierarchical way and all of the available pores in the fingerprint images are considered. By applying the MICPP and TDSWR methods to the fingerprints images in Fig. 3.7(a), 15 and 83 pores are matched, respectively, as shown in Fig. 3.7(b) and Fig. 3.7(c). It can be seen that TDSWR is more robust to the instability of pores than MICPP.

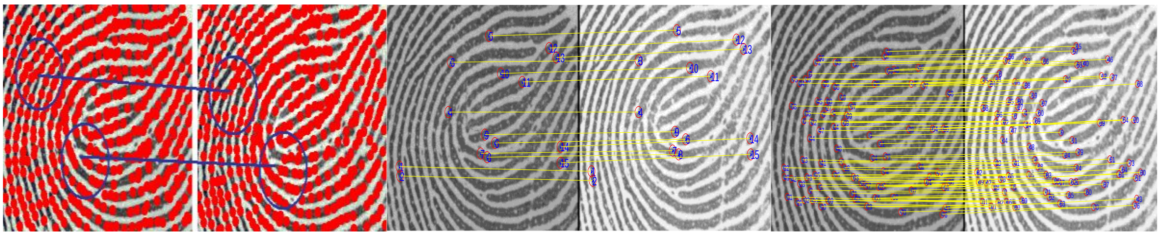

(a) (b) (c)

Fig. 3.7: Example pore matching results of MICPP and TDSWR. (a) Two example fingerprint images with extracted pores and corresponding minutiae. (b) Final pore correspondences obtained by MICPP. (c) Final pore correspondences obtained by TDSWR.

Here, it should be noted that the circled neighborhood for MICPP set in this chapter is with radius 45. We select such radius by testing different neighborhood radiuses, such as 15, 30, 45, 60, 75, and 90. We found when using small neighborhood (with radius 15 or 30), the number of matched pores is small due to the few number of pore in a small neighborhood. While increasing the radius of neighborhood (45, 60, 75, and 90), more and more false pore correspondences are obtained by MICPP because the local alignment estimated from the mated minutiae cannot be applied to large regions. The middle neighborhood radius 45 is finally chose based on the number of detected matched pore pairs.

3.4.3 Effectiveness in Pore Correspondence Establishment

Fig. 3.8 gives the pore correspondences found by different methods in an example genuine pair of fingerprint images in DBI. Figs. 3.8(a-c) show the first 20 coarse pore correspondences (red dashed lines denote the false ones) obtained by the correlation based method, the classical SR based method, and the TD-Sparse method, respectively. It can be seen that there are 15, 7, and 3 false pore correspondences in the results of the three methods, respectively. Table 3.1 reports the average number of true pore correspondences among the first 20 coarse pore correspondences (denoted as $\overline{N}_{Top\,20}$) in 100 pairs of genuine fingerprint images randomly chosen from DBI. These results demonstrate that the proposed TD-Sparse based method can more accurately determine the coarse pore correspondences than both correlation based and SR based methods, because it can better distinguish different pores and is more robust to noise and non-linear distortion which are very common in fingerprint images.

Fig. 3.8(d) and Fig. 3.8(e) show the final pore correspondences by applying the classical RANSAC and the WRANSAC to the coarse pore correspondences established by the TD-Sparse method. WRANSAC found 41 pore correspondences, whereas RANSAC found only 27 pore correspondences. Obviously, WRANSAC is more effective in refining pore correspondences. Moreover, according to our experimental results on DBI, on average, WRANSAC converges in 174 iterations, whereas RANSAC converges in 312 iterations. Hence, WRANSAC is also more efficient than RANSAC.

Table 3.1: Average number of true pore correspondences among the first 20 coarse pore correspondences ($\bar{N}_{Top20}$) in 100 genuine fingerprint pairs randomly selected from DBI.

Method	$\bar{N}_{Top20}$
Correlation based method	8
SR based method	11
TD-Sparse based method	14

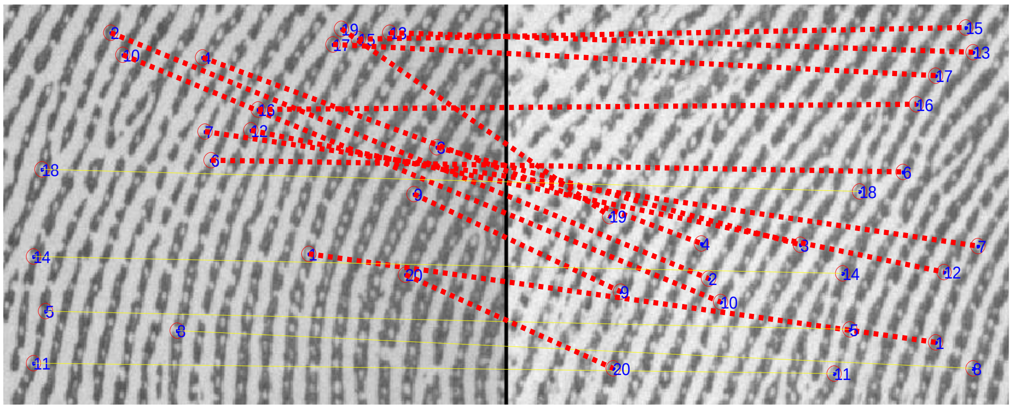

(a)

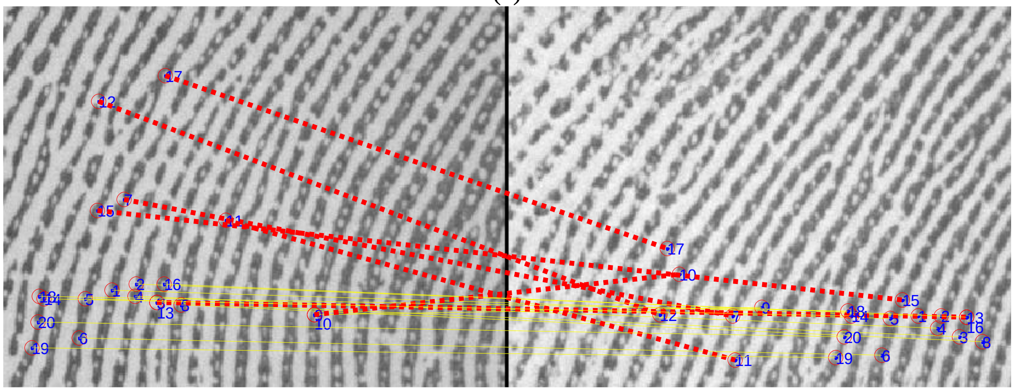

(b)

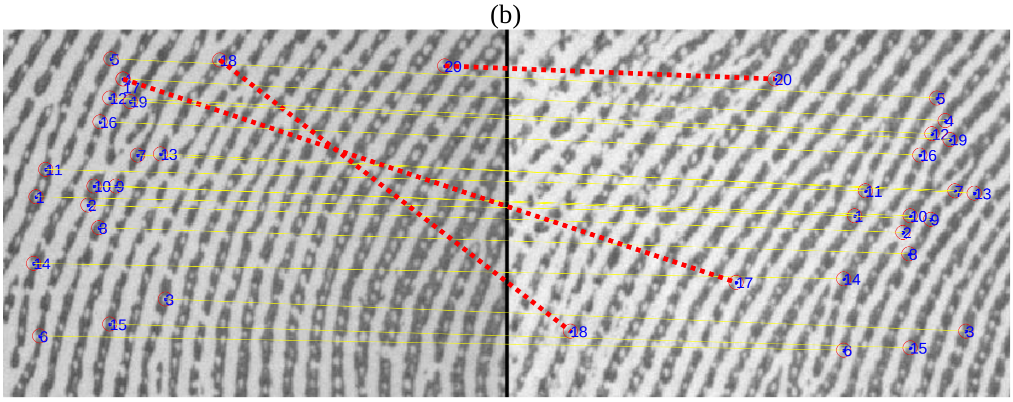

(c)

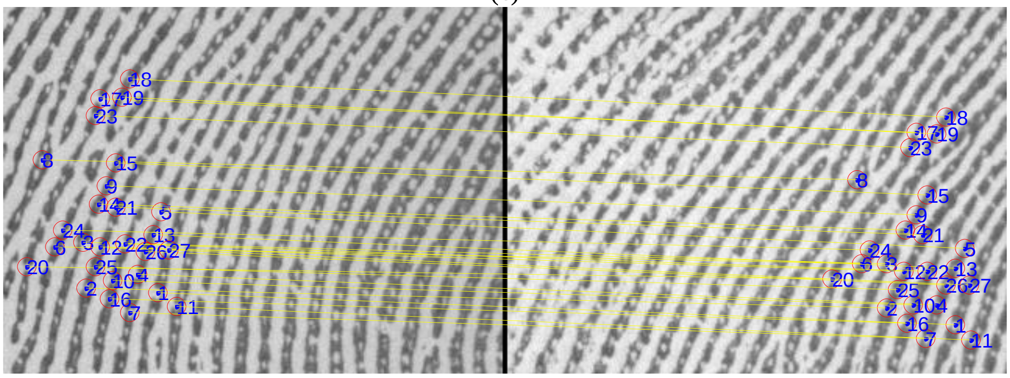

(d)

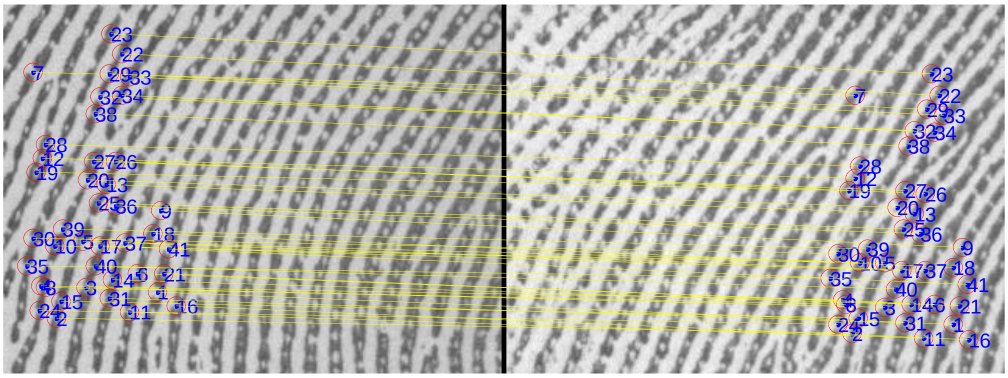

(e)

Fig. 3.8: Example pore correspondence establishment results. The first 20 coarse pore correspondences obtained by (a) correlation, (b) SR, and (c) TD-Sparse based methods. Final pore correspondences obtained by applying (d) RANSAC and (e) WRANSAC to the coarse pore correspondences established by the TD-Sparse method.

3.4.4 Fingerprint Recognition Performance

In order to illustrate the importance of one-to-many coarse pore correspondences for accurate fingerprint recognition, we compare the EERs on DBI by using one-to-many TD-Sparse (denoted as 1toM_TD-Sparse), one-to-one TD-Sparse (denoted as 1to1_TD-Sparse) and one-to-one correlation (denoted as 1to1_Correlation) based methods to establish coarse pore correspondences and using RANSAC to refine the pore correspondences. Here, we choose RANSAC algorithm because there are no weights available for 1to1_Correlation method in [71]. The results are presented in Table 3.2. As can be seen, the lowest EER is obtained by 1toM_TD-Sparse, which shows the effectiveness of one-to-many coarse pore correspondences in improving fingerprint recognition accuracy.

We finally compare the fingerprint recognition performance of the proposed TDSWR method, the MICPP, DP, and SRDP methods on DBI and DBII. Fig. 3.9 shows the ROC curves of these methods, and the corresponding EERs are listed in Table 3.3. It can be seen that TDSWR outperforms both MICPP and DP by decreasing the EER by one order of magnitude on both DBI and DBII. Compared with SRDP, TDSWR has also improved the EER by more than 50% and 45%

on DBI and DBII, respectively. This fully demonstrates the effectiveness of TD over ED for fingerprint pore matching.

Table 3.2: EER of pore matching with different coarse pore correspondence establishment methods.

Database / EER (%) / Method	DBI
1to1_Correlation	15.42
1to1_TD-Sparse	5.82
1toM_TD-Sparse	4.45

Table 3.3: EER of different pore matching methods.

Database / EER (%) / Method	DBI	DBII
MICPP	30.45	7.83
DP	15.42	7.05
SRDP	6.59	0.97
TDSWR	3.25	0.53

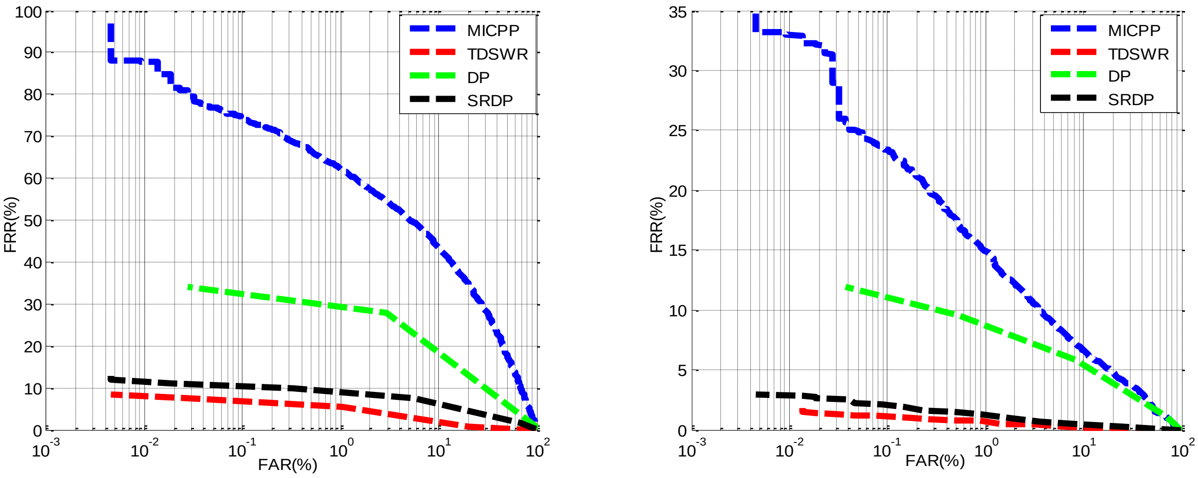

(a) (b)

Fig. 3.9: ROCs of different pore matching methods on (a) DBI and (b) DBII.

We believe that the improvement achieved by the proposed TDSWR method owes to the following three factors. First, the hierarchical strategy makes the matching method more robust to the instability of pores. Second, the TD-Sparse method used to find coarse pore correspondences is not only robust to noise, which has been demonstrated in [95], but also robust to fingerprint distortion by using TD instead of ED in sparse representation. Third, the one-to-many coarse pore correspondence establishment scheme together with the WRANSAC based refinement make it more effective and efficient to find the correct pore correspondences in fingerprints.

3.4.5 TDSWR Applied in Fingerprint Minutiae Matching

The proposed TDSWR is also suitable for minutiae matching in fingerprints. Fig. 3.10 shows an example of fingerprint matching results based on minutiae. From the extracted result in Fig. 3.10(a), we can see that there are missing (solid circled), spurious (dashed circled) and inaccurate extracted (solid rectangled) minutiae in both compared fingerprints. Our proposed method can effectively establish the coarse correspondences, as shown in Fig. 3.10(b), there are 5 wrong correspondences in 24 coarse ones. 15 true correspondences are finally selected out after refinement, as shown in Fig. 3.10(c). Fig. 3.11 also shows the fingerprint recognition performance (ROC) of minutiae-based matching in DBII by using the proposed TDSWR method. The EER is about 11%, which further demonstrates the effectiveness of our proposed method for fingerprint matching.

This example matching also demonstrates that our proposed TDSWR method can be used for other image matching problems. It is because this approach firstly constructs a local descriptor at the location of each feature point, and then establishes coarse correspondences and refines the coarse pairs to get final result. The proposed TD-Sparse and WRANSAC methods are useful for any coarse matching and fine matching. Therefore, this method can be modified to solve different image matching problems by constructing different local descriptor or using different coarse (or fine) matching methods.

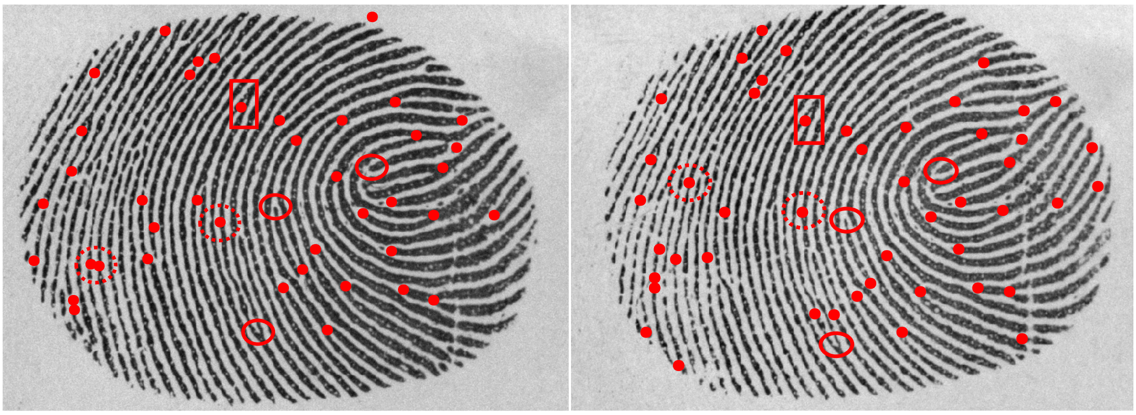

(a)

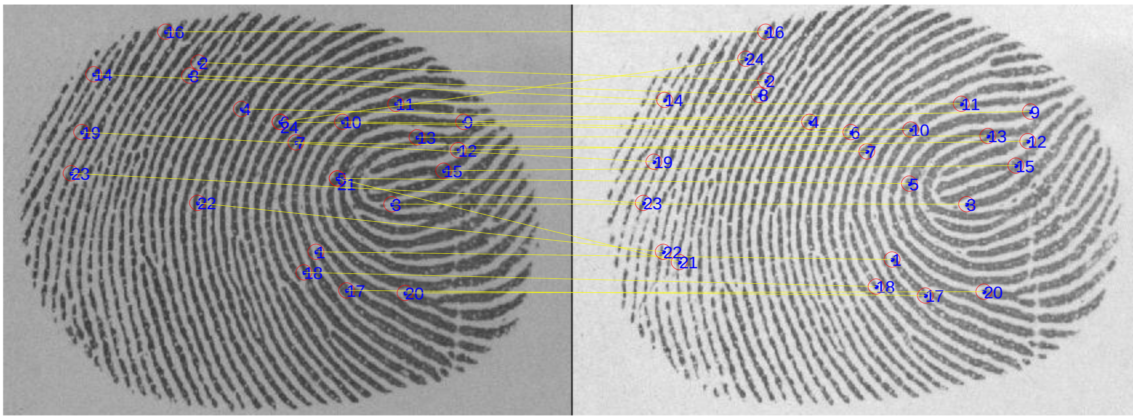

(b)

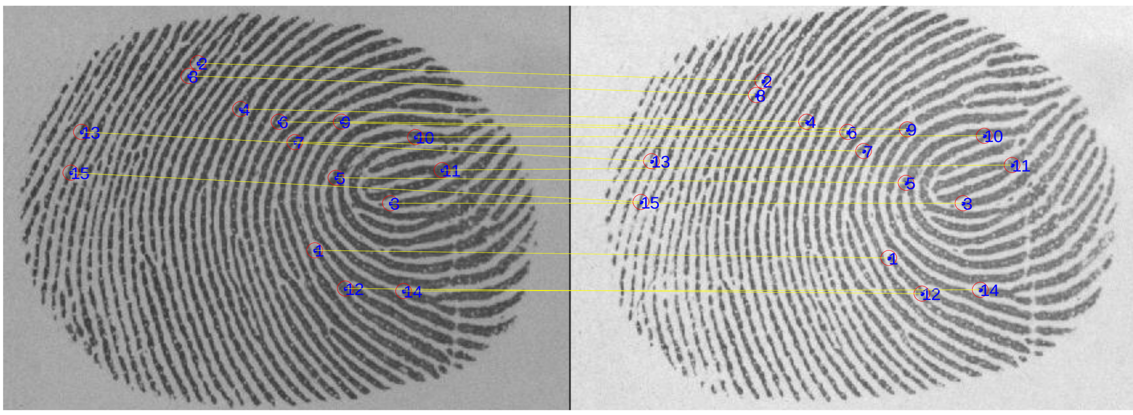

(c)

Fig. 3.10: Example matching results of TDSWR based on minutiae. (a) Two example fingerprint images with dotted extracted minutiae (41 in the left print and 47 in the right print). (b) Coarse minutiae correspondences (24 initial obtained minutiae pairs). (c) Final minutiae correspondences (15 true minutiae pairs).

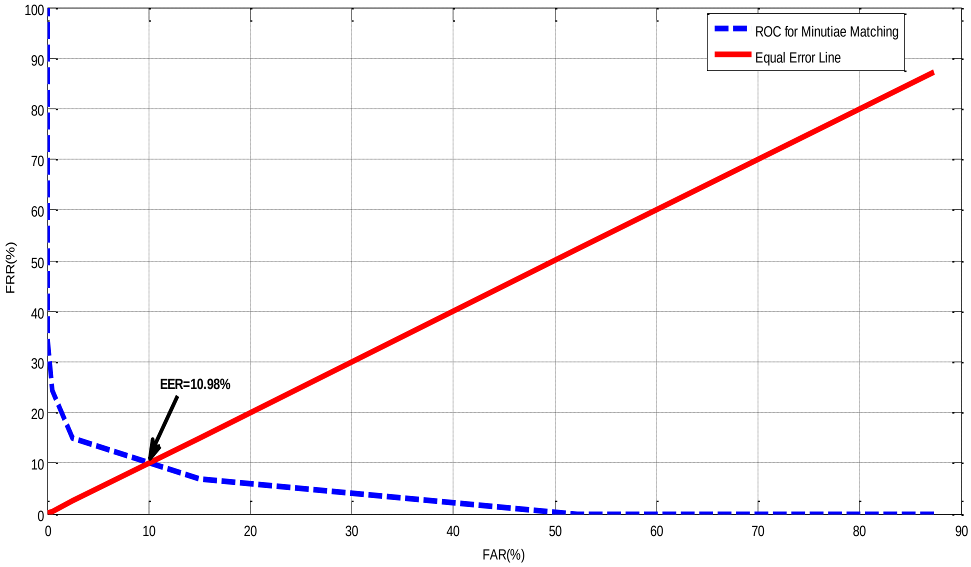

Fig. 3.11: ROC for minutiae-based matching using TDSWR in DBII.

3.5 Summary

This chapter has proposed a novel hierarchical fingerprint matching method, namely TDSWR which mainly applied in sweat pore, by introducing the TD-Sparse based method for coarse pore correspondence establishment and WRANSAC for refinement. The proposed method measures the differences between pores based on the residuals obtained by tangent distance and sparse representation technique, which makes our method more robust to noise and local distortions in fingerprints when compared with the existing DP and SRDP method. It then establishes one-to-many coarse pore correspondences, and assigns to each correspondence a weight based on the difference between the pores in the correspondence. The final pore correspondences are obtained by adopting WRANSAC to refine coarse pore correspondences. The experimental results demonstrate that the proposed method can more effectively establish pore correspondences and finally reduce the EER by one order of magnitude in both of the two fingerprint databases used in the experiments (the best improvement on the recognition accuracy is up to 92%). However, the high computational complexity is one of the limitations of the proposed method. How to further improve the efficiency of the proposed pore matching method is among our future work. One possible solution is first aligning two fingerprints to estimate the overlapping area between them and then matching only the pores lying in the overlapping area.

Chapter 4
Touchless Multi-view Fingerprint Acquisition Device

Touchless fingerprint capture devices have the advantage over traditional touch-based approaches of being hygienic and preventing distortions resulting from the contact of fingers. Single-view acquisition systems bring in problems such as scene difference and a limited effective area. This chapter thus presents a touchless multi-view fingerprint capture system that acquires three different views of fingerprint images at the same time. This device is designed by optimizing parameters regarding the captured fingerprint image quality and device size. A fingerprint mosaicking method is put forward to splice together the captured images of a finger to form a new image with larger useful print area. Optimization design of our device is demonstrated by introducing our design procedure and comparing with current touchless multi-view fingerprint acquisition devices. The efficiency of our device is further proved by comparing recognition accuracy between mosaicked images and touch based fingerprint images. In the chapter, advantages of touchless multi-view imaging and comparisons of current touchless multi-vide imaging device are firstly introduced in section 4.1. The details of our proposed touchless multi-view fingerprint acquisition device are presented in section 4.2. In section 4.3, we briefly introduced a fingerprint image mosaicking algorithm which is used for stitching the multiple fingerprint images captured from different views into one single fingerprint image. Performance analysis and comparison is given in section 4.4. Section 4.5 concludes the chapter.

4.1 Introduction

Nowadays, fingerprint technique has been widely used in both forensic and civilian applications. Compared with other biometric features, fingerprint-based biometric is the most proven technique and has the largest market shares. Although fingerprint recognition has been studied for many years and much progress has been made, the performance of state-of-the-art matchers is still much lower than the expectations of people and theory estimation [9]. Up to now, processing low quality latent prints still needs human intervention. In addition to the requirement for higher accuracy and speed, many new requirements are also raised along with increasing adoption of fingerprint technique in civilian applications, such as template security, hygiene and so on.

Fingerprint images can be acquired in off-line or on-line mode. The so-called ink-technique and extraction of latent fingerprints in crime scenes are examples of off-line acquisition. Nowadays on-line acquisition techniques have been widely used. Common on-line acquisition techniques include optical, solid-state, thermal and ultrasound [27]. Optical devices work in either touch-based or touchless mode. Frustrated total internal reflection (FTIR), as a well-known touch-based fingerprint imaging technique, is used in most of government and forensic applications due to its excellent image quality and low cost. Touchless optical fingerprint imaging is actually not a novel technique. It uses cameras to directly image the fingertip. It has the advantages of hygiene, no latent prints, and no distortion caused by pressure. As its image quality is lower than that of FTIR images and its size is bigger than that of solid-state sensors, this type of fingerprint devices is currently seldom found in the market. However, in recent years, with emergence of more applications, popularity of multimodal biometrics, and development of fingerprint algorithms, there is necessity of reconsidering touchless fingerprint imaging technique.

Earlier works about touchless fingerprint imaging devices began from single-camera mode [45, 81, 102-105]. Song et al. [81] designed a touchless fingerprint device using a monochrome CCD camera and double ring-type illuminators with blue LEDs. They stated that good quality images can be obtained by using the ring-type illuminators and some algorithmic amendments. Products of touchless fingerprint sensors from companies (e.g. Mitsubishi [102], TST Biometrics [103] and Lumidigm [104]) are on sale. Chen [105] described a device that captures 3D shape of finger by using structured lights with one camera and one projector. Kumar [45] used a simple web camera to capture very low resolution fingerprint images. These kinds of devices all face the problem of view difference due to curvature of the finger shape. In real fingerprint recognition systems, the performance is degraded by the limited common area between fingerprints caused by view difference.

To deal with the above mentioned problem, multi-view touchless sensing techniques have been proposed [35, 40, 83, 106, 107]. Typically, TBS [35] proposed a 3D multi-camera touchless fingerprint device named Surround Imager™ by using five cameras to capture nail-to-nail fingerprint images at one time and provided the reconstructed 3D finger shape, as shown in Fig. 4.1 [85]. In their paper, they gave a brief description of the device design and related algorithms about 3D reconstruction and recognition. However, the details of algorithms have not been given and performance evaluation has not been reported. Later, they continued to improve their device and developed new versions of products by using three cameras at one time [107]. The detail specifications of the devices and algorithms for image processing are yet not available. Kim et al [83] suggested using a single camera and two planar mirrors to form the multi-view fingerprint imaging device. The side views of the finger reflected by these mirrors are captured by the central camera to form multi-views of fingerprint images. This device has the advantage of low cost, but the hardware design is very complex. For instance, the depth of field (DOF) of the central camera should be large enough to cover the three views of finger with high clarity. The setting of mirror and finger should be carefully considered due to the different size of finger. Such system has two difficulties: (i) Dividing the whole image (as shown in Fig. 4.2) into three segments manually. Constant threshold is not suitable to different size of fingers, as shown in Fig. 4.2. (ii) Stereo calibration for 3D reconstruction. Current techniques for stereo calibration are mostly based on separate pictures captured by different cameras. The effective area in side-view images provided by mirror-reflected device is normally smaller than the one offered by multi-camera based device (see Fig. 4.1(a) and Fig. 4.2). Table 4.1 summarizes the strengths and weaknesses of these two typical touchless multi-view fingerprint imaging systems.

Table 4.1: Comparison of strengths and weaknesses of two typical touchless multi-view fingerprint imaging devices.

Device	Strengths	Weaknesses
Surround Imager™	Cover larger effective area; Possible to achieve 3D reconstruction;	Relatively Expensive;
Mirror-reflected imaging device	Low cost;	High hardware designing complexity; Manually segmentation of ROI; Limited effective area in side-view images reflected by mirrors;

(a) (b)

Fig. 4.1: Example images [85]. (a) Different views of fingerprint images captured by Surround Imager™, (b) Illustration of reconstructed 3D finger shape.

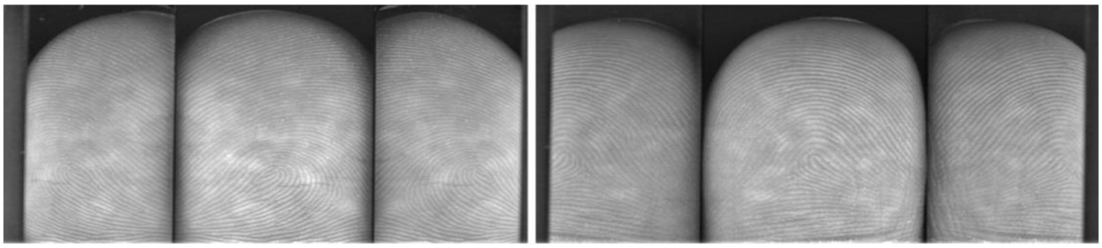

(a) (b)

Fig. 4.2: Fingerprint images of two different fingers captured by the mirror-reflected device [83].

Due to the drawbacks of mirror-reflected imaging technique, multi-camera mode is adopted in this chapter to design our fingerprint acquisition device. Meanwhile, considering the drawbacks and difficulties to get detail specifications of existing multi-camera mode devices, as well as the unavailability of large scale touchless multi-view fingerprint databases in the public domain, this chapter designed a touchless multi-view fingerprint capture device using multi-camera mode with optimized device parameters. Both image quality and device size are considered in designing the capture device. We established a database with 541 fingers. Based on the established database, we studied a mosaicking technique using SIFT (Scale Invariant Feature Transformation) feature and classical RANSAC (RANdom SAmple Consensus) algorithm to give example of application of captured fingerprint images.

4.2 Fingerprint Acquisition

With the motivation of designing a cheaper and more optimized touchless multi-view fingerprint capture device, we studied and selected the system parameters in this section. The schematic diagram of the device is shown in Fig. 4.3. Cameras are focused on the finger. LEDs are used to light the finger and are arranged to give uniform brightness. A hole is designed to place the finger with fixed position. The main factors which influence the captured image quality, device size, and size of overlapping region between adjacent cameras mainly include the camera and lens configuration, distance between finger and lens, color of light source, and camera numbers and arrangement. The device proposed in this chapter is designed based on the camera JAI CV-A50. We next discussed the design of our device in detail as follows.

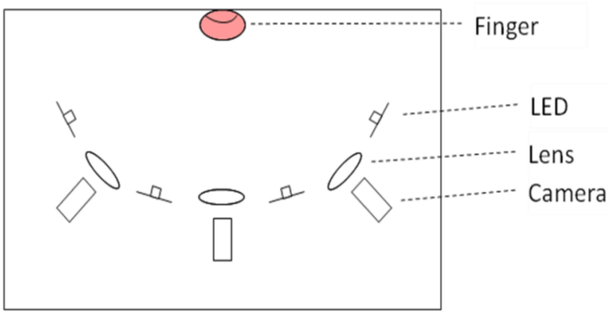

Fig. 4.3: Schematic diagram of the proposed touchless multi-view fingerprint acquisition device.

4.2.1 Lens Selection and Distance Setting

To calculate the differences between pores, this chapter uses the sparse representation technique

In order to capture fingerprint images with high quality and minimize the size of device, it is very important to select suitable lens and set appropriate distance between fingers and lens. Because these two factors have impact on the captured image resolution, size of the effective fingerprint area and the height of the device.

Different fingerprint features can be robustly extracted from different resolution images [18]. For traditional touch-based automated fingerprint identification systems, ~500dpi and ~800dpi are required for minutiae and sweat pores, respectively as we discussed in Chapter 2. For touchless-based systems, there is no survey showing which resolution is suitable. In [35], the resolution is larger than 500dpi (700dpi in center part and minimum of 500dpi on image boarders). In [83], the resolution of captured image is ~500dpi.

In this chapter, we tried several kinds of resolutions to find an optimal one. Example fingerprint images at three kinds of resolution: ~750dpi, ~500dpi, and ~400dpi are shown in Fig. 4.4. The corresponding lens focal length and object-to-lens distance is (25mm, 105mm), (16mm, 145mm), and (12mm, 91mm), respectively. The image size is all restricted to 576 pixels by 768 pixels. We finally set our device lens focal length and object-to-lens distance as (12mm, 91mm) based on the following three reasons. Firstly, we found that ridges on fingerprint images can be extracted at all of the above mentioned resolutions, as shown in Fig. 4.5. Secondly, the size of effective area is the largest one when resolution is at 400dpi. Thirdly, the minimum object-to-lens distance is reached when resolution is ~400dpi.

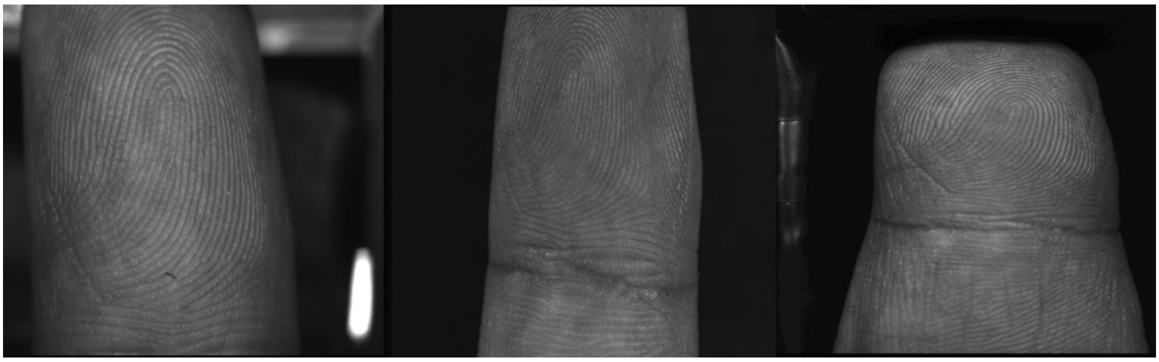

(a) (b) (c)

Fig. 4.4: Fingerprint images with respect to different resolutions. (a) ~750dpi. (b) ~500dpi. (c) ~400dpi.

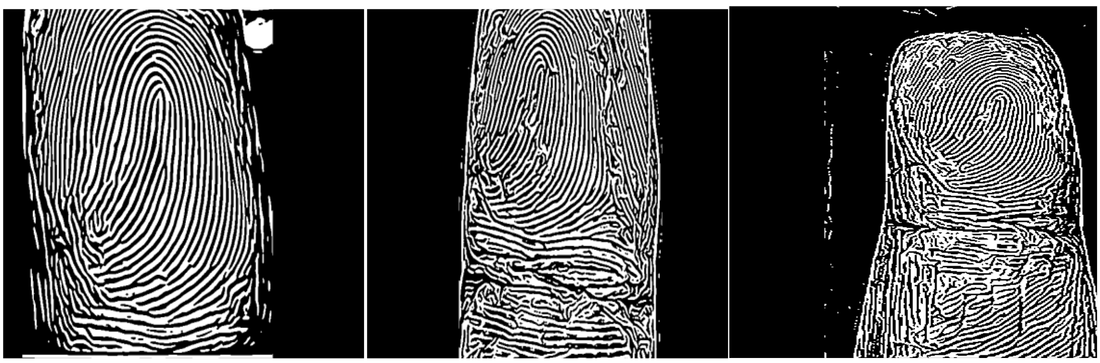

(a) (b) (c)

Fig. 4.5: Binarized fingerprint images with respect to different resolutions. (a) ~750dpi. (b) ~500dpi. (c) ~400dpi.

4.2.2 Light Source Selection

Human skin has different luminous reflectance to different light sources [108]. Proper illuminator will help us to obtain touchless fingerprint images with high ridge-valley contrast. Among various kinds of light sources, blue LED and green LED are most popular ones. In [35], authors demonstrated that green light provides a higher contrast than red and blue lights. In [109], authors studied how to get high-contrast contactless fingerprint images from aspects of polarization states, illumination wavelength, detection wavelength, and illumination direction. They offered systematic evidence that blue LED is the best choice among infrared LED, red LED, green LED and blue LED. This chapter thus captured several fingerprint images using blue LED and green LED as illuminator, binarized them using the same algorithm and parameters.

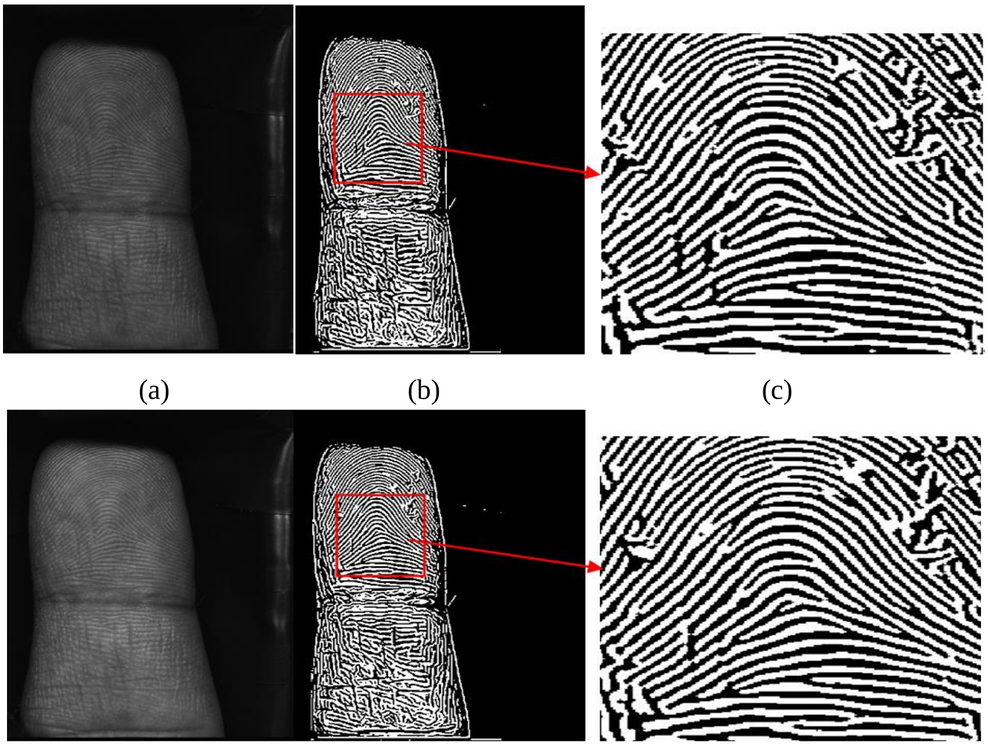

(a) (b) (c)

(d) (e) (f)

Fig. 4.6: Fingerprint images captured under different light sources. (a) Original image captured by using blue LED. (b) Binarized image of (a). (c) Zoomed-in segment on (b). (d) Original image captured by using green LED. (e) Binarized image of (d). (f) Zoomed-in segment on (e).

Fig. 4.6 shows an example images. We found that there is little difference between blue LED and green LED when binarizing the images by the same algorithm, as shown in Fig. 4.6(c) and Fig. 4.6(f). The zoomed-in segment of binarized fingerprint images using blue LED is similar with the one using green LED. Indicated by the strong evidence shown in [109], we finally chose blue LED as the light source in this chapter.

4.2.3 Camera Number and Arrangement

The number of cameras directly decides the cost of the device. The smaller the number of cameras is, the cheaper the device will be. Moreover, too many views of images will aggravate the computational complexity of algorithms since there are more redundant information needs to handle with the growing of image views. Whereas, too few cameras cannot provide a sufficiently large view of the finger and result in small overlapping region between side and frontal images. Given the value of resolution r and the size of the image $w*h$, we can easily calculate the size of measured area of the finger $W*H$ by Eq. 2.1 introduced in Chapter 2. When we set resolution as ~400dpi and image size as 576*768 pixels in our device, the measured area will be 36.58mm * 48.77mm. It is large enough to cover the size of most fingers, which means that the full view of the finger can be captured by each camera in our device, as the example images shown in Fig. 4.8, one camera can provide the full view of the finger. However, the shape of human's fingers is curved, which leads to different distances from different parts to the lens. From Fig. 4.7, we can see that the distance from side parts to lens (i.e., D_2 or D_3) is larger than the distance from central part to lens (i.e., D_1). Perspective distortion is thus caused by these distance differences. As illustrated in Fig. 4.8, the right view of the finger disappeared when capturing images from the left side of the finger, while the left view of the finger was gone when see it from the right camera. To alleviate the perspective distortion problem in side parts of fingers, three cameras, one central camera and two side cameras, are used in our device to capture different views of the finger, as shown in Fig. 4.3.

In a word, we fixed our capturing device with three cameras by considering the device cost and providing a sufficiently large view of the finger simultaneously.

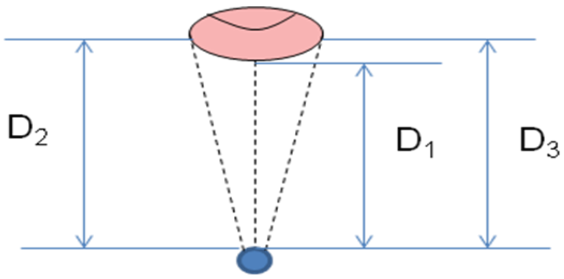

Fig. 4.7: Distances between lens and different parts of the finger.

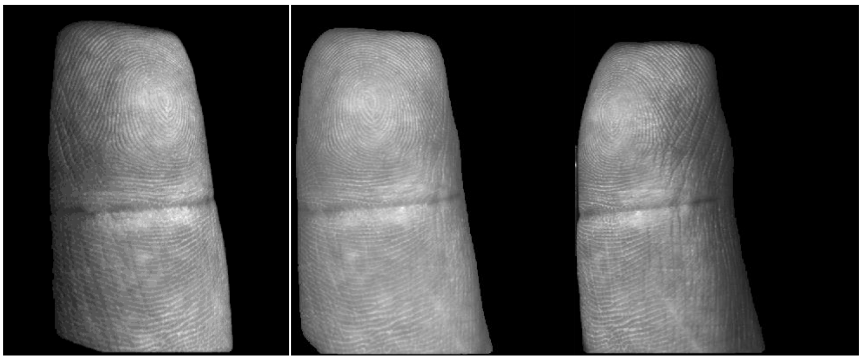

Fig. 4.8: Example images captured by three cameras (left, frontal, right).

The placement of camera is important since it affects the size of overlapping area and the final mosaic image size. In Surround Imager™, the angle between adjacent cameras is around 45°, while in the mirror-reflected device, the angle of mirrors is set to 15°empirically. In our design, we tried angles of 15°, 30°, and 45°. Intuitively, the smaller the angle between adjacent cameras is, the larger the overlapping region is. However, the side view of fingers cannot be captured if the angle is too small. As the example images shown in Fig. 4.9, when the angle is set as 15°, the image captured by the left side camera is almost the same as the one captured by the central camera. Finally, we set the angle between central camera and side camera as roughly 30°in our device.

(a) (b)

Fig. 4.9: Example fingerprint images captured by (a) left and (b) central cameras when the angle between them is 15°.

To summarize, we designed the multi-view touchless fingerprint capture device shown in Fig.4. 3 with specific parameters mentioned above. The three view images of a finger captured by our device are shown in Fig. 4.10.

Fig. 4.10: Original images of a finger captured by our device (left, frontal, right).

4.3 Fingerprint Mosaicking

As shown in Fig. 4.10, we can get left-side, frontal, right-side fingerprint images at one time by our device, from which we observed that the geometrical resolution of the image decreases from the fingerprint center towards the side and the contrast of ridge and valley is not high. To overcome the drawbacks of view difference and enlarge the size of effective area, one solution is to combine these three views of images into one single image. Thus, fingerprint mosaicking is studied in this chapter.

Fingerprint image mosaicking is a technique for integrating different view of images into a single image with larger undistorted fingerprint area. The procedure of fingerprint image mosaicking mainly includes feature extraction, transform estimation, stitching line selection and post processing. In our proposed method, we firstly preprocess the original image, extract the scale invariant feature transformation (SIFT) feature point, and establish initial correspondences by point wise matching method. Then, the parameters of thin plate spline (TPS) model are estimated for aligning the side and frontal images. After that, the stitching line is selected from the overlapping region of adjacent images. The mosaicked fingerprint image is finally generated after smoothing. The overview flow chart of the algorithm is presented in Fig. 4.11 and details of the proposed approach are described as follows.

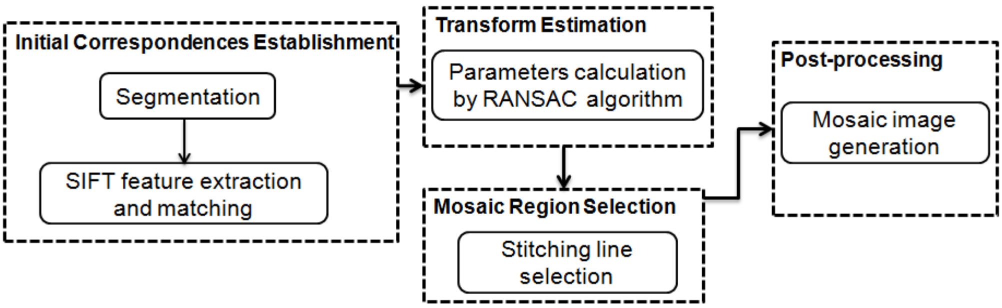

Fig. 4.11: The overall flow chart of the proposed fingerprint mosaicking method.

4.3.1 Initial Correspondences Establishment

To extract more accurate fingerprint features, we should segment the image into foreground and background firstly. The iterative thresholding segmentation method [117] is adopted, which can easily separate the ROI region from the background. This method selects the threshold to segment the foreground and background region in iterative fashion. In our situation, the iteration stops once the difference between the current threshold and the last one is smaller than 0.005. Finally ROI is extracted by the threshold. Fig. 4.12(b) and Fig. 4.12(e) show the segmentation results of Fig. 4.12(a) and Fig. 4.12(d).

Features frequently-used in fingerprint image mosaicking and matching contain minutiae, ridge map, and SIFT feature [83, 110-115]. In this chapter, we chose to use SIFT feature in our algorithms for the following three reasons. Firstly, due to the very low ridge-valley contrast in the fingerprint image captured by touchless imaging techniques, minutiae and ridge features are hard to correctly extract, as shown by the example in Fig. 4.13. Secondly, because of the errors introduced in thinning ridges and localizing minutiae, minutiae and ridge based mosaicking cannot reach pixel-level accuracy. Thirdly, SIFT feature is robust to low image quality and deformation variation [110]. Moreover, SIFT feature describes the local texture features exactly in pixel level and is rich in quantity [112].

SIFT [116, 118] was popular in object recognition and image retrieval. It provides feature which is invariant to scale, rotation and affine transforms. There are four main steps to extract SIFT features. (i) The scale-space extrema is detected from images generated by applying multi-scales of difference of Gaussian (DoG) functions to the input image; (ii) The accurate location of keypoint is determined according to the measurement of their stability; (iii) The major orientation of each keypoint is calculated to achieve rotation-invariant keypoint descriptor; (iv) SIFT feature with four properties, i.e., spatial location (x, y), scale (s), orientation (θ) and keypoint descriptor (*kd*), is finally generated. Figs. 4.12(c) and 4.12(f) show the SIFT points extracted from the example fingerprint images in Figs. 4.12(a) and 4.12(d). There are totally 7,534 and 6,956 SIFT points, respectively.

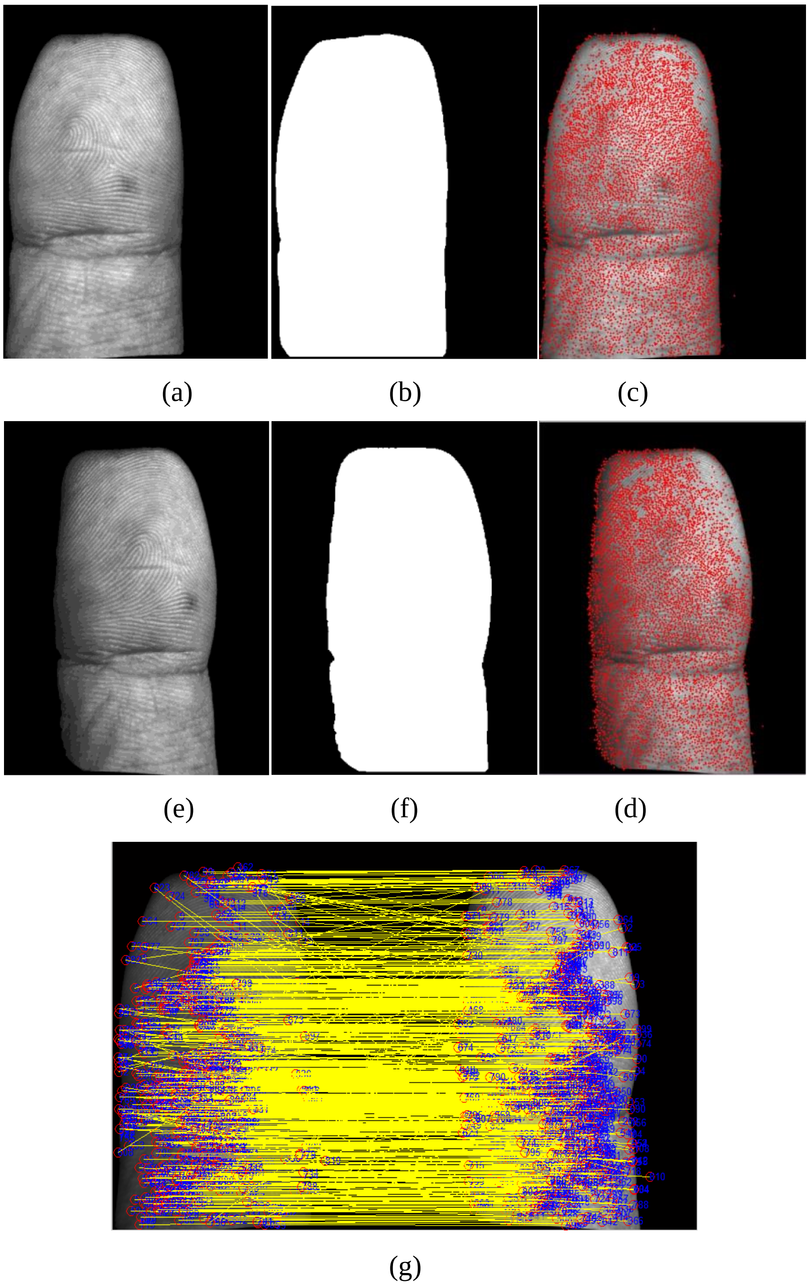

Fig. 4.12: Initial correspondences Establishment. (a) Original frontal image. (b) Segmentation result of (a) by iterative thesholding method. (c) Extracted SIFT points from (a). (d) Original left-side image. (e) Segmentation result of (d) by iterative thesholding method. (f) Extracted SIFT points from (d). (g) Initial correspondences establishment by point wise matching.

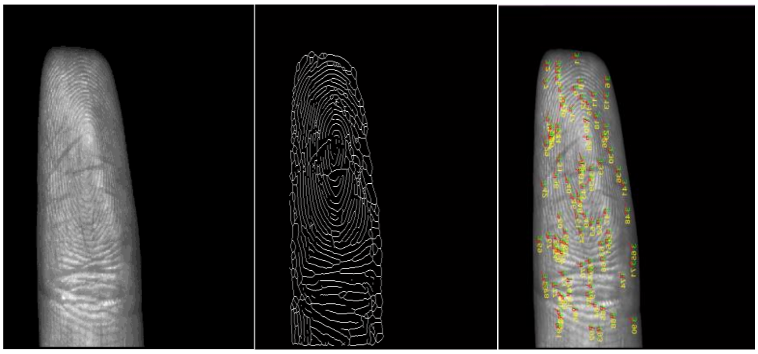

(a) (b) (c)

Fig. 4.13: Example fingerprint image with very low ridge-valley contrast. (a) Original image. (b) Ridge map. (c) Extracted minutiae.

After SIFT feature extraction, a point wise matching method is adopted to find correspondences between the feature sets of two images. The method is performed by comparing the associated descriptors of SIFT points. More specifically, given two SIFT feature sets P_1 and P_2 extracted from two images I_1 and I_2, we calculate the inner product between descriptor of each feature point in P_2 and descriptor of each feature point in P_1. For each feature point in P_1, we can find its top-2 closest points in P_2, whose distances to the feature point are labeled as d_1 and d_2. We then compute the ratio d_1/d_2. If the value of the ratio is sufficiently small, the point in P_1 is considered to match with the closest point in P_2. 811 pairs of SIFT points are matched by applying this method to Figs. 4.12(a) and 4.12(d), as shown in Fig. 4.12(g).

4.3.2 Transform Estimation

From Fig. 4.12(g), we can see that there are false correspondences. To estimate exact parameters of transform model between two images, we apply the classical RANSAC algorithm [100], which is insensitive to initial alignment and outliers, to calculate the optimal model parameters in an iterative fashion. The main idea of the classical RANSAC algorithm is introduced in Chapter 3, section 3.3. Finally, the optimal transform model parameters and consensus set (CS) are both provided. It is notable that the model used in this method depends on the deformation form of the matched images. Due to the curved surface of finger and distortions introduced by cameras, we chose TPS model in the RANSAC algorithm. This model is popularly used in fingerprint domain [83, 115, 63]. Fig. 4.14 gives the CS when RANSAC. TPS model acted on the initial correspondences of Fig. 4.12(g), which demonstrated the effectiveness of the algorithm.

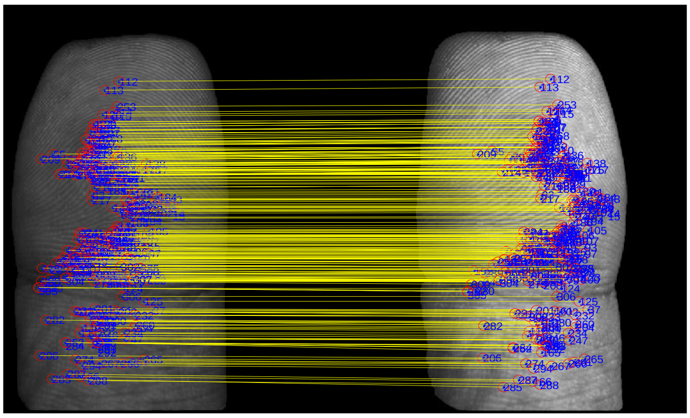

Fig. 4.14: CS of Fig. 4.12(g) obtained by RANSAC with TPS model.

4.3.3 Mosaic Region Selection

Once the transform model parameters are obtained, we should determine how to stitch them to generate the final mosaic image. The approach we proposed consists of two stages. In the first phase, we extract the overlapping region of the two images. The width of the overlapping region is constrained by the maximal and minimal column coordinates given in the transformation estimation step. As shown in Fig. 4.15, the overlapping region on the frontal and left side images is framed by blue lines. In the second phase, we segment the overlapping region into sub-blocks with size of 21*21 pixels, and then calculate the correlation between the sub-block in left side image and the corresponding sub-block in frontal image. The location of the stitching line is defined as the center line of the sub-block which offered the largest correlation value. The red line in Fig. 4.15 shows the final stitching line.

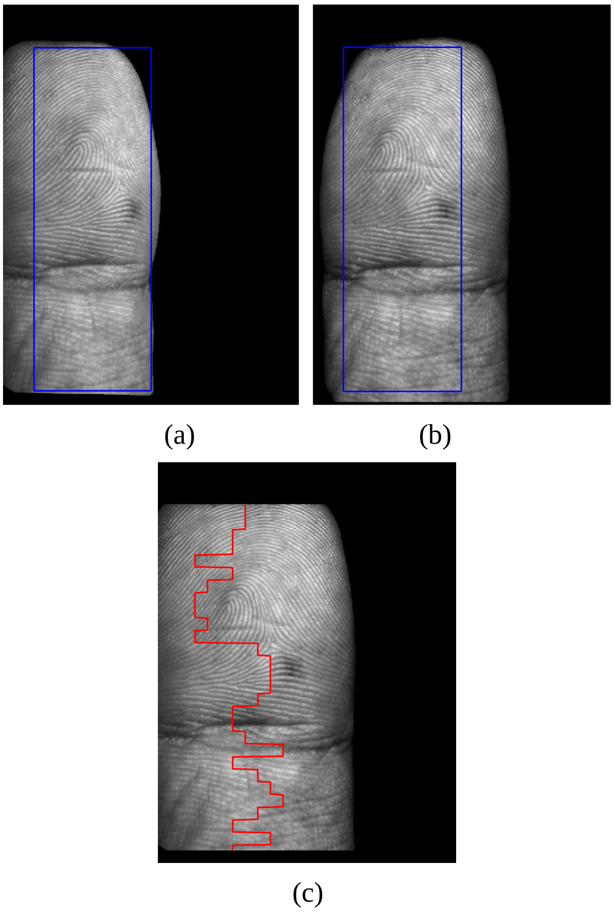

Fig. 4.15: Stitching line extraction. (a) Original left-side image with rectangled overlapping region. (b) Original frontal image with rectangled overlapping region. (c) The extracted stitching line.

4.3.4 Post-process

Due to the intensity difference of images captured by separate cameras, normalization is necessary to make the mosaicked image smooth. Here, we used the MAX_MIN strategy to all of the images based on the intensities of their overlapping regions. Then, a Gaussian smoothing is applied to the mosaicked image to get the final result, as shown in Fig. 4.16.

Fig. 4.16: Final mosaicked image for the three images in Fig. 4.10.

4.4 Experimental Comparison and Performance Analysis

Generally, touch based plain fingerprint image has the advantage of high ridge-valley contrast but the disadvantage of small print size, whereas touchless multi-view fingerprint imaging technique permits large print size but low image quality. To find out whether the multi-view technique compensates the drawbacks of touchless imaging at certain degree, we compared recognition accuracy of touchless based images and touch based fingerprint images on databases of touch based fingerprint images (collected by U.ARE.U4000) and touchless multi-view fingerprint images which are collected from 215 fingers, each 4 examples. Fig. 4.17 shows examples of our collected data. We used the SIFT based matching method introduced in section 4.3 and took the size of CS (consensus set) as the match score. Another conventional fingerprint feature—minutia was adopted and matched by using the method introduced in [111]. The fusion results by the weighted sum (WSUM) rule [71] were also given. Fig. 4.18 shows the receiver operating characteristic (ROC) curves on touch-based and touchless multi-view fingerprint images. As can be seen from Fig. 4.18(a), touch-based fingerprint recognition outperforms single-view touchless based fingerprint recognition, whereas comparable equal error rates (EERs: ~3.5% and ~4%, respectively) are obtained for touch-based and mosaicked touchless fingerprint images when SIFT feature is used. When adopting minutiae for recognition, as shown in Fig. 4.18(b), better performance is achieved for touch-based images than for mosaicked touchless images. However, comparable performance is achieved between mosaicked touchless images and touch-base images when fusing SIFT feature and minutiae, as the results shown in Fig. 4.18(c) with EERs of ~0.9% and ~0.4%, separately.

(a) (b)

Fig. 4.17: Examples of fingerprint images from the same finger. (a) Touch based fingerprint image. (b) Frontal touchless fingerprint image.

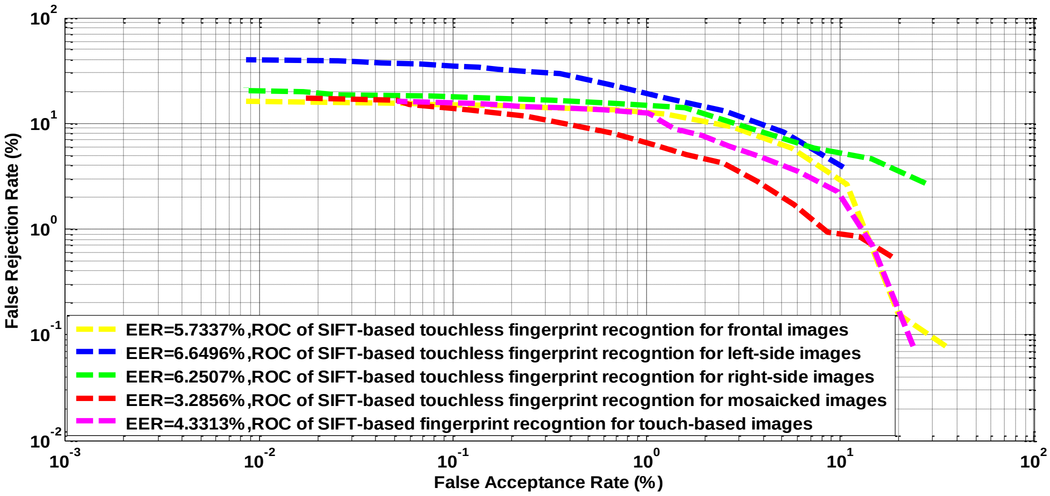

(a)

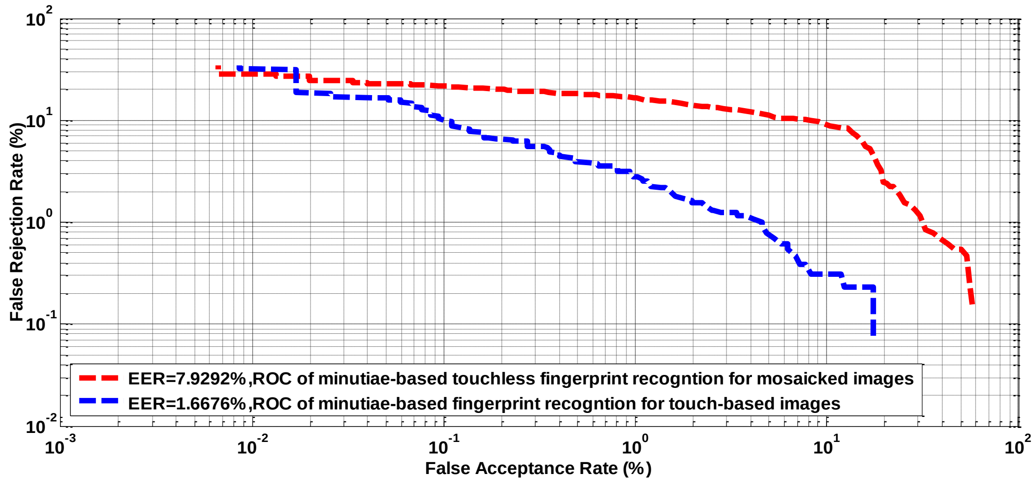

(b)

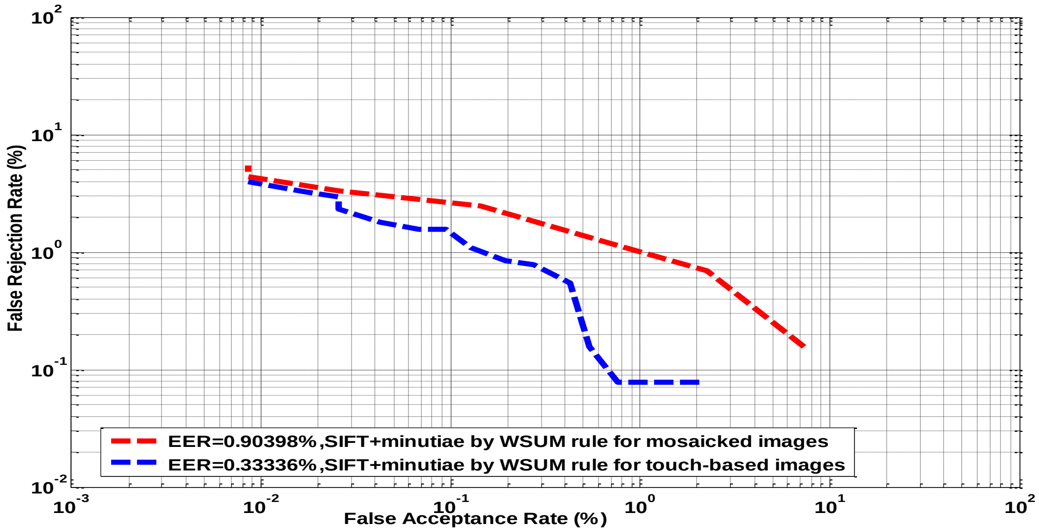

(c)

Fig. 4.18: Comparison of ROC curves for recognition with touchless images and touch based fingerprint images. (a) Results with single-view touchless images, mosaicked touchless fingerprint images and touch based fingerprint images by using SIFT feature. (b) Results with mosaicked touchless fingerprint images and touch based fingerprint images by using minutiae. (c) Results with mosaicked touchless fingerprint images and touch based fingerprint images by fusing SIFT and minutiae features.

4.5 Conclusion

This chapter has proposed a touchless multi-view fingerprint image acquisition device and associated fingerprint mosaicking method. The advantage of multiview imaging is that it obtains more fingerprint information quickly while touchless imaging has the advantages of hygiene, avoiding fingerprint deformation, and not producing latent prints. However, touchless imaging does suffer from low ridge-valley contrast and perspective distortion between images of different views. Therefore, we designed our device by optimizing several factors which affect the captured image quality and device size. We then proposed a mosaicking method to get expanded fingerprint images with larger effective area. When mosaicking, we used the SIFT feature which is robust to low ridge-valley contrast. Experimental results show the effectivenss of our device by comparing recognition accuracy between mosaicked images and touch based fingerprint images.

Nonetheless, the current system still has some drawbacks which are inevitable to touchless imaging techniques. For some fingers, the image quality of the device is much lower than that of touch-based devices and some fingers are so tilted that some part of the fingerprint is out of the depth of field. There are either very narrow or wide ridges in one image due to the curve surface of finger. Such low quality fingerprints and large variations of ridge frequency call for a very robust feature extraction algorithm (e.g. minutiae extraction). Considering the fact that the area of touchless fingerprints is generally larger than that of touch-based fingerprints, we believe that future work will enable us to extract more distinctive information from touchless fingerprints than from touch-based fingerprints. We further foresee that the current system can be improved in the following three ways. First, a more robust feature extraction algorithm is required to deal with fingerprint images of very low quality and with large variations of ridge frequency. Second, we can obtain greater accuracy by the addition of non-minutiae information (e.g. finger shape, finger crease feature, image-based features, 3D information etc.). Finally, we propose to explore tighter fusion schemes, such as fusion at the feature or match score level.

Chapter 5

3D Fingerprint Image Generation Technique

In the last chapter, we have built a touchless multi-view acquisition device which capturing three different views of images simultaneously. Such 2D fingerprint images can be used to reconstruct their corresponding 3D finger shape using the binocular stereo vision theory in computer vision domain. This chapter thus studies the 3D fingerprint reconstruction technique, which offers a solution for 3D fingerprint image generation and application when only multi-view 2D images are available. For 3D fingerprint reconstruction, the difficulties and stresses focus on correspondence establishment based on 2D touchless fingerprint images and the finger shape model estimation. In the chapter, several popular used features, such as scale invariant feature transformation (SIFT) feature, ridge feature and minutiae, are employed for correspondence establishment. To extract these fingerprint features accurately, an improved fingerprint enhancement method has been proposed by polishing orientation and ridge frequency maps according to the characteristics of 2D touchless fingerprint images. Therefore, correspondences can be established by adopting hierarchical fingerprint matching approaches. By an analysis of 440 3D point cloud finger data (220 fingers, 2 pictures each) collected by a 3D scanning technique, i.e., the structured light illumination (SLI) method, the finger shape model is estimated. Also, it is found that the binary quadratic function is more suitable for the finger shape model than the other mixed model tested in this chapter. In our experiments, the reconstruction accuracy is illustrated by constructing a cylinder. Furthermore, results obtained from different fingerprint feature correspondences are analyzed and compared. Backgrounds of fingerprint reconstruction techniques are firstly introduced in Section 5.1. In Section 5.2, the procedures of the proposed 3D fingerprint reconstruction system are briefly introduced. Section 5.3 is devoted to the proposed methods to establish fingerprint feature correspondences. The approach to estimating the finger shape model is described in Section 5.4. Experimental results and reconstructing error analysis are given in

Section 5.5. We summarized this chapter in Section 5.6.

5.1 Backgrounds

As one of the most widely used biometrics, fingerprints have been investigated for more than a century [18]. Advanced AFRSs are available in the market everywhere and most of them capture fingerprint image by using touch-based technique since it is easy to obtain images with high ridge-valley contrast. However, touch-based imaging technique introduces distortions and inconsistencies to the images due to the contact of finger skin with device surface. In addition, the curved 3D finger surface flattens into 2D plane during image acquisition, destroying the 3D nature of the fingers. To deal with these problems, 3D fingerprint imaging techniques start to be considered [35, 119-124]. Usually, these techniques capture fingerprint images at a distance and provide the 3D finger shape feature simultaneously. The advent of these techniques brings new challenges and opportunities to existing AFRSs.

Currently, there are three kinds of popular 3D imaging techniques: multi-view reconstruction [35, 119, 120], laser scanning [121, 128, 129], and structured light scanning [122-124]. Among them, the multi-view reconstruction technique has the advantage of low cost but the disadvantage of low accuracy. Laser scanning normally achieves high resolution 3D images but costs too much and the collecting time is long [121, 128, 129]. As mentioned in [129], the currently available commercial 3D scanning systems cost from $2,500 to $240,000 USD. The time of scanning a turtle figurine (18*cm* long) is from 4 to 30 minutes for different scanners [128]. The status (wet or dry) of objects also affects the accuracy of 3D images due to surface reflection. The wetter the surface is, the lower the accuracy will be [121]. Different from the multi-view reconstruction and laser scanning, structured light imaging has a high accuracy as well as a moderate cost. However, it also takes much time to collect 3D data and suffers from the instability problem such that one needs to keep still when projecting some structured light patterns to the human finger [122-124]. Thus, it is necessary and important to study the reconstruction technique based on multi-view 2D fingerprint images when considering the cost, friendliness, as well as the complexity of device design. It is well known that the 3D spatial coordinates of an object are available from its two different plane pictures captured at one time according to binocular stereo vision theory in computer vision domain if some camera parameters and the corresponding matched pairs are provided [119]. In [35], the authors briefly introduce the 3D reconstruction method since it is the same as those methods used to reconstruct any other type of 3D objects. There are several drawbacks with adopting general methods for 3D fingerprint reconstruction. For instance, it is time-consuming for the reason that the coordinate of each pixel need to be calculated. Only the 3D coordinates of correspondences which represent the same portion of the skin between two neighbor image pair can be calculated. 3D visualization of finger is unavailable if correspondences cannot be found between two neighbor image pair.

To overcome the above mentioned disadvantages, a new 3D fingerprint reconstruction system using feature correspondences and prior estimated finger model is proposed in this chapter. Comparative little research has been carried out into touchless fingerprint matching due to the characteristics of touchless fingerprint imaging, and hardly any work can be found for finger shape model analysis. This chapter, for the first time, analyzes touchless fingerprint features for correspondences establishment and studies the model of human finger. 3D fingerprints are then reconstructed based on the images captured by our own designed touchless multi-view fingerprint imaging device introduced in the last Chapter. Fig. 5.1 shows the schematic diagram of our designed acquisition device and an example of 2D fingerprint images. Finally, 3D fingerprint reconstruction results based on different feature correspondences are given and compared with that of manually labeled correspondences. It is concluded that such reconstruction results are useful in fingerprint recognition domain.

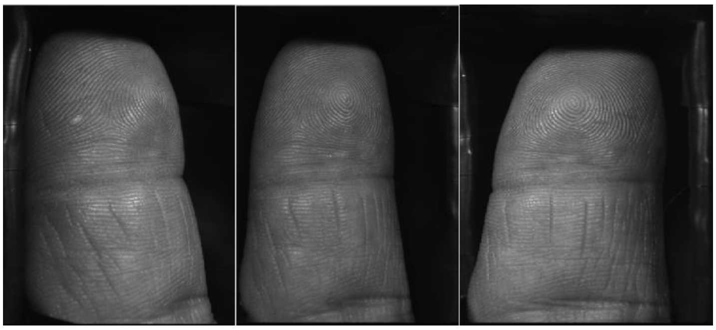

Fig. 5.1: Images of a finger captured by our designed device introduced in Chapter 4 (left, frontal, right).

5.2 3D Fingerprint Reconstruction Technique

According to the theory of binocular stereo vision in computer vision domain [119], the 3D information of an object can be obtained from its two different plane pictures captured at one time. As shown in Fig. 5.2(a), given two images *Cl* and *Cr* captured at one time, the 3D coordinate of A(*X, Y, Z*) can be calculated if some camera parameters (*fl* (focal length of the left camera), *fr* (focal length of the right camera), *Ol* (principal point of the left camera), *Or* (principal point of the right camera), etc.) and the matched pair $((a_l(u_l, v_l)) \leftrightarrow (a_r(u_r, v_r))$,where $a_*(*)$ represents a 2D point in the given images *Cl* or *Cr* , u_* is the column-axis of the 2D image and v_* is the row-axis of the 2D image) are provided. Once the shape model and several calculated 3D coordinates of the 3D object are known, the shape of the 3D object can be obtained after interpolation. As can be seen in Fig. 5.2(b) shown, the triangle in 3D space is obtained after computing 3D coordinates of three vertices and fitting by triangle model. Therefore, the reconstruction method is divided into five parts, including the camera parameters calculation, correspondences establishment, 3D coordinates computation, shape model estimation, and interpolation. The flow chart of the reconstruction system is shown in Fig.5. 3.

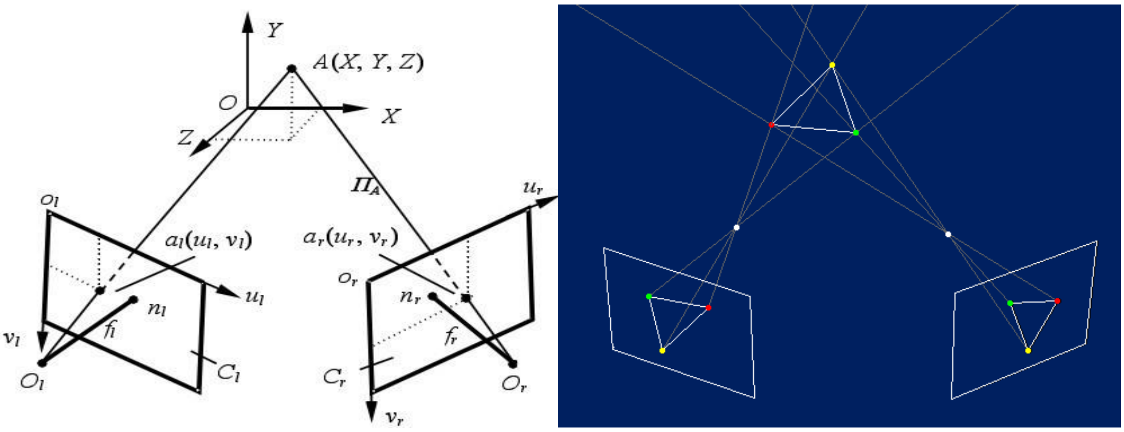

(a) (b)

Fig. 5.2: An illustration of constructing a 3D triangle based on binocular stereo vision. (a) 3D coordinates calculation on 3D space, (b) 3D triangle reconstruction.

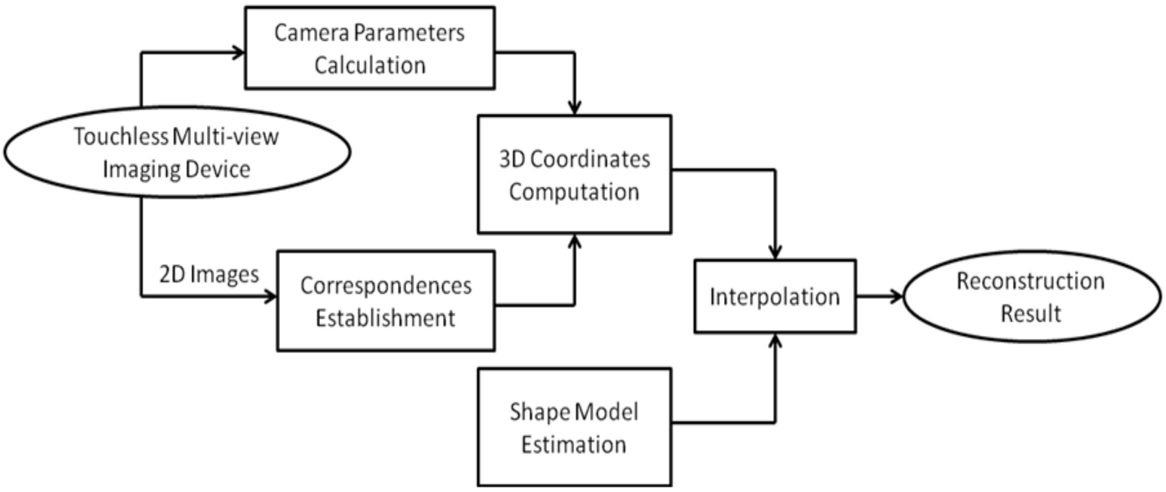

Fig. 5.3: The flow chart of our reconstruction algorithm.

Camera calibration is the first step for 3D reconstruction. It provides the intrinsic parameters (Focal Length, Principal Point, Skew, and Distortion) of each camera and extrinsic parameters (Rotation, Translation) between cameras necessary for reconstruction. It is usually implemented off-line. In this chapter, the methodology proposed in [125] and the improved algorithm coded by Bouguet [126] is employed. The free codes we used can be obtained from the website [126]. It can be noted that there are three cameras used in our fingerprint capturing device. The position of the middle camera is chosen as the reference system because the central part of the fingerprint is more likely to be captured by this camera, where the core and the delta are usually located. The frontal image captured by the middle camera is also selected as the texture image when generating the final 3D fingerprint image. To permit the frontal view of finger being captured by the middle camera of the device, a simple guide is given for users to correctly use the device.

Correspondences establishment is of great importance to the 3D reconstruction accuracy, it is then introduced in detail in Section 5.3.

Once camera parameters and matched pairs between fingerprint images of different view are both obtained, the 3D coordinate of each correspondence can be calculated by using the stereo triangulation method coded by J.Y. Bouguet [126].

Since it is very hard to identify all of the correspondences which represent the same portion of the skin between two neighboring fingerprint image pairs, it is very important to calculate the 3D finger shape for 3D fingerprint visualization. This chapter for the first time analyzes finger shape models and presents them in detail in Section 5.4.

Based on the calculated 3D coordinates of limited feature correspondences and the estimated shape model, a 3D finger shape can be finally reconstructed by interpolation. Here, we adopted the classical approach, namely, multiple linear regression using least squares [133, 134], for interpolation due to its simplicity and effectiveness.

5.3 Fingerprint Feature Correspondence Establishment

Fingerprints are distinguished by their features. Different fingerprint features can be observed from different resolution fingerprint images. There are three frequently-used features for low resolution fingerprint images, namely Scale Invariant Feature Transformation (SIFT) feature, ridge map and minutiae [45, 83, 110-115]. This chapter thus tries to extract such features and establish correspondences between different views of fingerprint images.

5.3.1 Correspondence Establishment based on SIFT Feature

SIFT [116] is popular in object recognition and image retrieval since it is robust to low quality image. For touchless fingerprint images, it has the characteristic of low ridge-valley contrast. This feature makes true correspondences can be established when minutiae and ridge features cannot be correctly extracted. Moreover, it is robust to deformation variation and rich in quantity [110, 112]. Fig. 5.4(b) and Fig. 5.4(d) show the examples of the extracted the extracted 1,911 and 1,524 SIFT features, respectively. 108 pairs are matched by using the point wise matching method to Fig. 5.4(a) and Fig. 5.4(c), as shown in Fig. 5.4(e). From Fig. 5.4(e), we can see that there exist false correspondences and hence a refined algorithms need to be employed to select true ones. To this end, the classical RANSAC algorithm [100] is utilized. It should be noted that the TPS model which is popularly used in fingerprint domains [63, 83, 114] is adopted in the RANSAC algorithm due to the curved surface of finger and distortions introduced by cameras. Fig. 5.4(f) gives the final selected true correspondences when RANSAC with TPS model acts on the initial correspondences of Fig. 5.4(e).

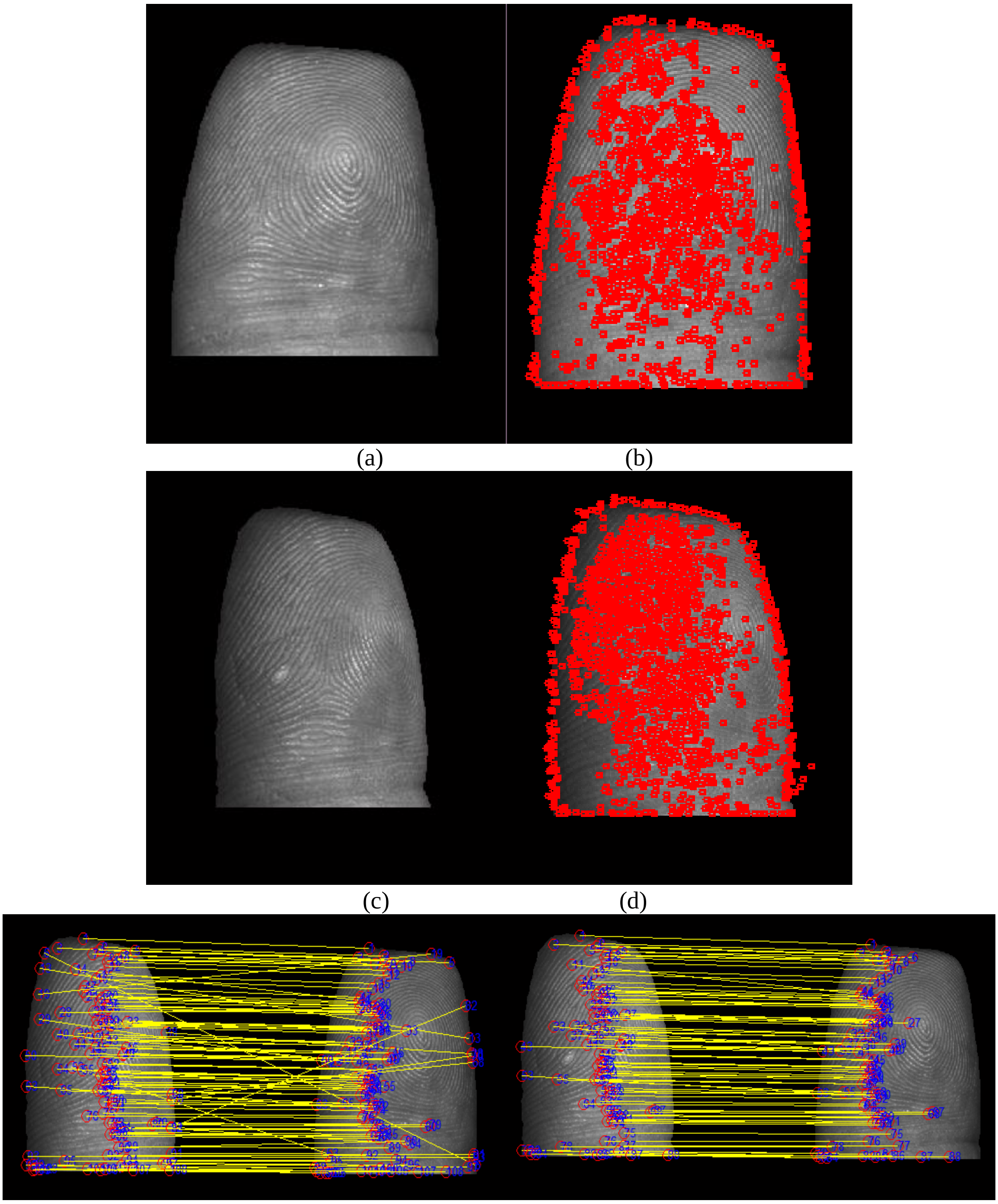

(a) (b)

(c) (d)

(e) (f)

Fig. 5.4: Example of correspondences establishment based on SIFT features. (a) Original frontal image, (b) Extracted SIFT feature from (a), (c) Original left-side image, (d) Extracted SIFT feature from (c), (e) Initial correspondences established by point wise matching, (f) Final correspondences after refining by RANSAC method.

5.3.2 Correspondence Establishment based on Ridge Map

Before establishing correspondence between ridge maps, ridges must be extracted and recorded. In general, ridge map refers to the thinning image where ridges are one-pixel-width, ridge pixels have value 1 and background pixels have value 0. Fig. 5.5 shows the flowchart of steps for ridge map extraction. However, touchless fingerprint images have low ridge-valley contrast and their ridge frequency increases from center to side, as shown in Fig. 5.4(a) and Fig. 5.4(c). These make it difficult to extract the ridge map accurately due to the difficulty of fingerprint enhancement. Currently, there are a number of fingerprint enhancement approaches, such as Gabor filter-based, STFT-based, DCT-based and Diffusion filter-based methods [58, 135-142]. Among them, Gabor filter based method is the simplest and the most traditional one. It is finally adopted in this chapter. Fingerprint images are enhanced by a bank of Gabor filters generated from given fingerprint orientation and frequency. Orientation and frequency maps play an important role in the enhancement approach. This chapter thus tries to improve the orientation map and frequency map so as to acquire better enhanced results.

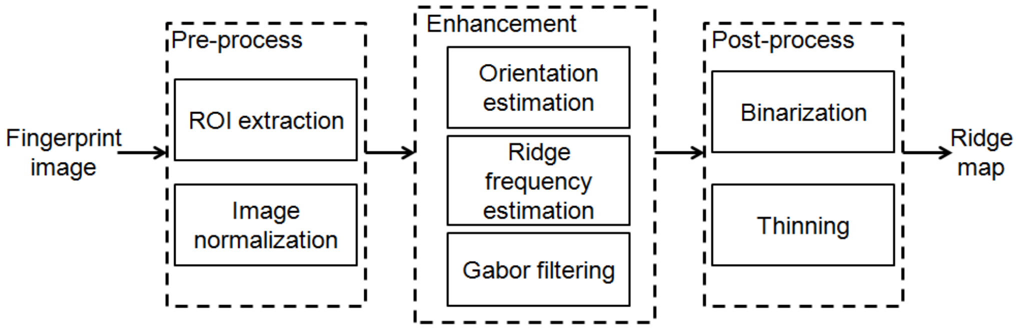

Fig. 5.5: Flowchart of ridge map extraction.

As introduced in [18], gradient-based ridge orientation estimation method is the simplest and most intuitive one. It is efficient and popularly used in fingerprint recognition domains. However, it also has some drawbacks, such as sensitivity to noise when orientation is estimated at too fine a scale or accuracy is decreased if smooth factors are used, as shown in Fig. 5.6(a) (red rectangle) and Fig. 5.6(b) (green rectangle). To keep the estimation accuracy of a good quality area and correct the orientation where noises exist, a method is proposed to act on original orientation map to improve the orientation map. The main steps include: (i) Part the original orientation map into eight uniform regions. Small blocks in the uniform regions represent the wrong estimated orientation results (see Fig. 5.7(a), red circled); (ii) Sort uniform regions with the same color in a descending manner, such regions whose size is smaller than the mean size of all regions with the same color are set to zero (see Fig. 5.7(b), dark regions in ROI); (iii) Assign values to the points with zero value set by step (ii) according to the nearest neighbor method. The improved orientation map is obtained by following these three steps. Fig. 5.6(c) shows our improved orientation map based on Fig. 5.6(a) and Fig. 5.7(c) gives the partition map according to Fig. 5.6(c). The results show that the estimation accuracy of a good quality area is kept and the wrong orientation area is corrected (Fig. 5.6(c), rectangle).

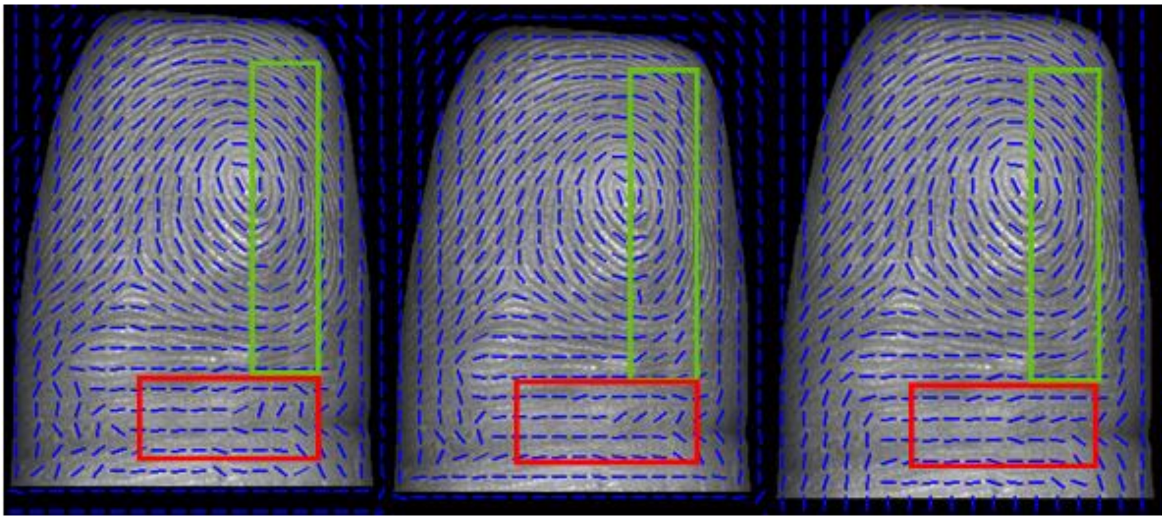

(a) (b) (c)

Fig. 5.6: Fingprint ridge orientation maps. (a) Original orientation map, (b) Smoothed orientation map of (a), (c) Improved orientation map by our proposed method.

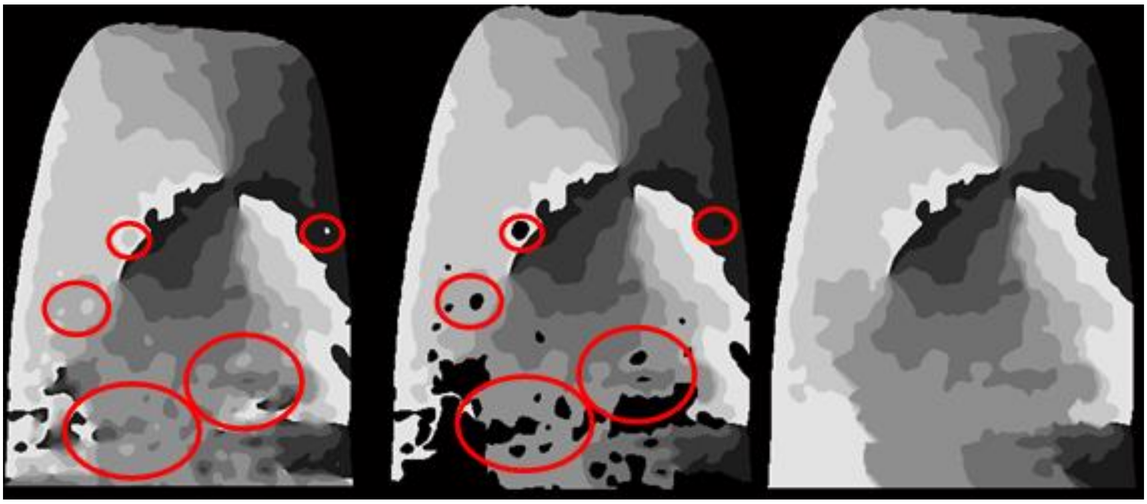

(a) (b) (c)

Fig. 5.7: Partition results according to orientation map. (a) Partition result according to original orientation map, (b) Partition result according to our improved orientation map.

Frequency maps record the number of ridges per unit length along a hypothetical segment and orthogonal to the local ridge orientation. The simplest and most popular ridge frequency estimation method is x-signatures based method [18]. However, this kind of method does not work with blurry or noisy fingerprint areas. In this situation, interpolation and filtering is used to post-process the original estimated frequency map. For touchless fingerprint images, frequency maps are harder to estimate than touch based fingerprint images due to the low ridge-valley contrast of touchless fingerprint images and simple interpolation or filtering is invalid when the frequency is wrongly estimated in neighborhoods. By observing the ridges on touchless fingerprint images, we find their frequency increases from the central part to the side part for horizontal section and decreases from the fingertip to the distal interphalangeal crease for vertical section, as shown in Fig. 5.8 (ridge frequency is calculated with blocks of 32*32 pixels). This phenomenon can be explained from touchless capturing technique and the observation of the human finger. As shown in Eq. 5.1, M is the optical magnification. p and q are the lens-to-object and lens-to-image distances, respectively. For a fix q, a large p will lead to a small magnification M. It is obvious that smaller M on the side parts than on the central part of the finger will be obtained since the distance from side parts to lens (D_2 or D_3 shown in Fig. 4.7 of last Chapter) is larger than the distance from central part to lens (D_1 shown in Fig. 4.7 of last Chapter). The smaller the magnification M is, the larger the ridge frequency will be. Thus, it is larger in the central part of ridge period than side-view ones for the horizontal section. The vertical distribution of ridge period increases from the fingertip to the distal interphalangeal crease because p increases from tip to the center part of the finger and ridges are wider near the distal interphalangeal crease than other parts by observation.

$$M = \frac{q}{p} \tag{5.1}$$

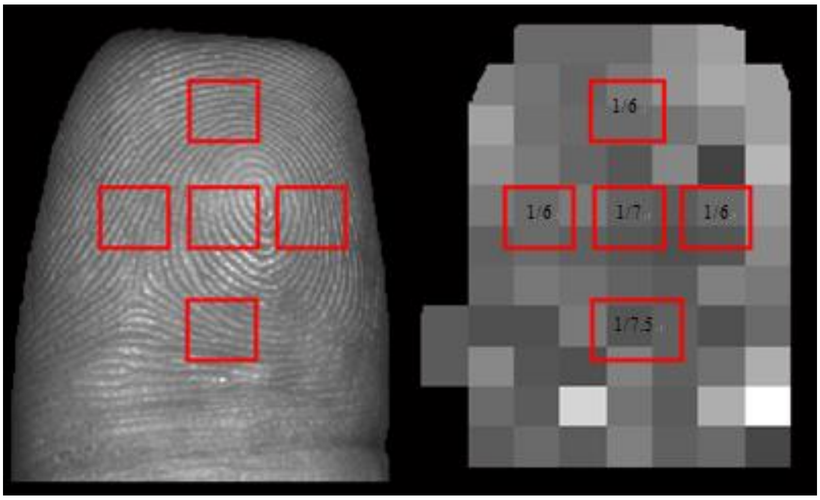

(a) (b)

Fig. 5.8: Frequency variation of touchless fingerprint images. (a) Original touchless fingerprint image, (b) Corresponding frequency map.

According to the distribution of ridge frequency of touchless fingerprint images, we proposes to use monotone increasing function (logarithmic function) to fit the ridge period (1/ridge frequency) map along vertical direction and quadratic curve along horizontal direction. The improved ridge period map is finally achieved by fitting original ridge period map with a mixed model of logarithmic function and quadratic curve.

Once the orientation and ridge frequency maps are calculated, a series of Gabor filter can be generated based on them. The enhanced fingerprint image was then obtained, as shown in Fig. 5.9. After binarizing the enhanced fingerprint image by simple threshold method and morphology approaches, the final ridge map is acquired. Fig. 5.9(a) and Fig. 5.9(b) show the ridge map of Fig. 5.4(a) enhanced by using the original orientation map and the original ridge frequency map interpolated by mean value of the frequency map. Fig. 5.9(c) and Fig. 5.9(d) show the ridge map of Fig. 5.4(a) enhanced by using our improved orientation map and ridge frequency maps. Better results by using the improved orientation and ridge frequency maps are achieved when comparing Fig. 5.9(c), Fig. 5.9(d) with Fig. 5.9(a), Fig. 5.9(b) (red rectangles). It is notable the pre-process steps of ROI extraction and normalization followed the method proposed in last Chapter.

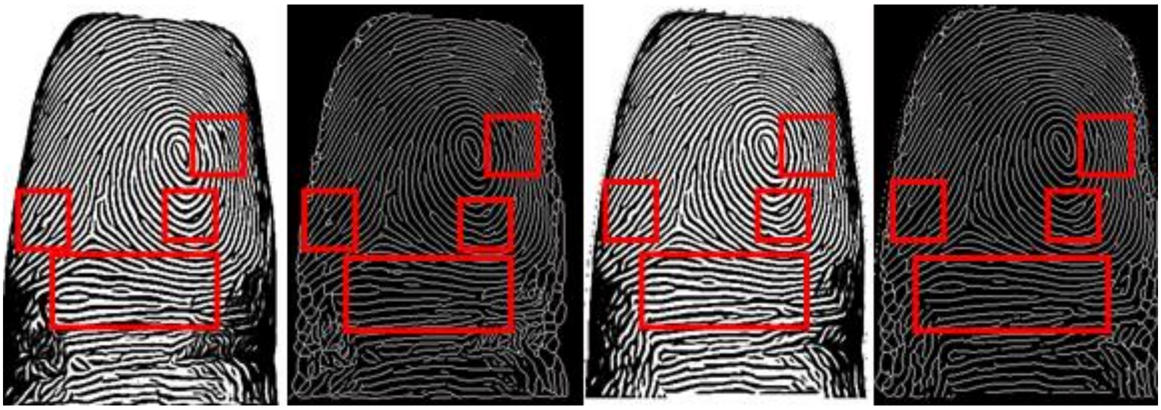

(a) (b) (c) (d)

Fig. 5.9: Ridge maps. (a) Ridge map of Fig. 5.4(a) enhanced by using original orientation and ridge frequency maps, (b) Thinned ridge map of (a), (c) Ridge map of Fig. 5.4(a) enhanced by using improved orientation and ridge frequency maps, (d) Thinned ridge map of (c).

Before correspondences establishment, ridges are record at tracing starting from minutiae where ridges are disconnected. Due to the existence of noise, ridge image often has some spurs and breaks. In some cases of insignificant noise, the ridge structure can be correctly recovered by removing short ridges or connecting broken ridges. However, in other cases of strong noise, it is difficult to recover the correct ridge structure by removing short ridges or connecting broken ridges. In such cases, we remove all related ridges. Finally, the down sampled ridge point coordinates of each ridge are recorded in a list.

Coarse alignment of two ridge maps is done by using the global transform model calculated in section 5.3.1 when SIFT feature matched. Ridges in ridge maps are then matched by adopting the Dynamic Programming (DP) method. As shown in Fig. 5.10 and Table 5.1, $\{a_1,a_2,\ldots,a_{10}\}$ represents a ridge line in the template ridge map and $\{b_1,b_2,\ldots,b_8\}$ denotes a ridge line in the test ridge map. For any ridge in template and test ridge maps, the Euclidian distance between each pair of compared ridge lines is calculated. The status will be 1 if the distance of a pair of ridge points is smaller than a threshold (it is set to 5 points in this chapter), otherwise, the status will be 0. The DP method is adopted to find matched ridge pairs with largest number. Coarse ridge correspondences are then established after DP. RANSAC algorithm introduced in last chapter is then adopted to select true ones from the coarse set. Fig. 5.11 shows the results of the established ridge correspondences.

Table 5.1: Record of status among ridge points in Fig. 5.10.

	a_1	a_2	a_3	a_4	a_5	a_6	a_7	a_8	a_9	a_{10}
b_1	0	0	0	0	0	0	0	0	0	0
b_2	0	0	0	0	0	0	0	0	0	0
b_3	0	0	0	0	1	0	0	0	0	0
b_4	0	0	0	0	0	1	1	0	0	0
b_5	0	0	0	0	0	0	1	1	0	0
b_6	0	0	0	0	0	0	0	1	0	0
b_7	0	0	0	0	0	0	0	0	1	0
b_8	0	0	0	0	0	0	0	0	0	0

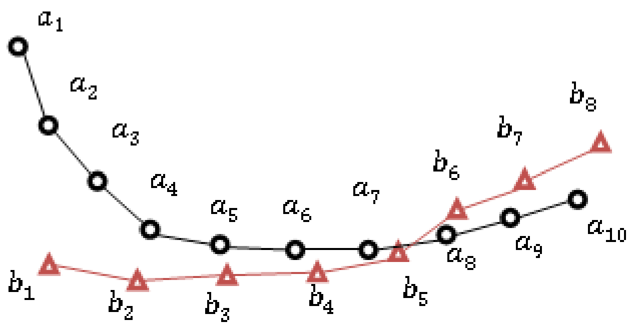

Fig. 5.10: Correspondences establishment between two ridges.

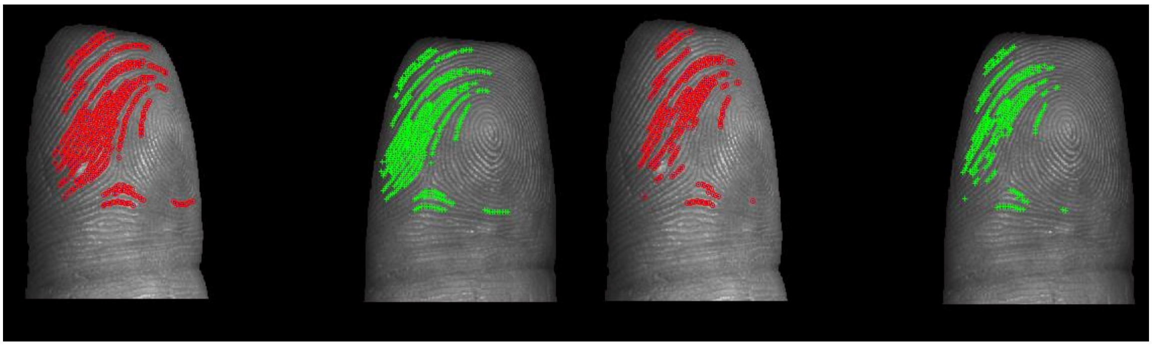

(a) (b)

Fig. 5.11: Ridge correspondence establishment. (a) Initial correspondences, (b) Final correspondences after RANSAC.

5.3.3 Correspondence Establishment based on Minutiae

Due to their distinctive ability, minutiae are widely used for fingerprint recognition and also considered in the chapter. They are extracted from the ridge map calculated in section 5.3.2. An example of extracted minutiae using the method introduced in [50] is shown in Fig. 5.12.

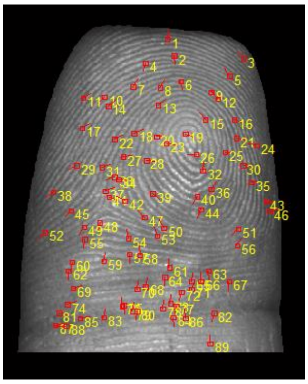

Fig. 5.12: Example of minutiae extraction result.

Since the transformation model is obtained when establishing SIFT correspondences, minutiae sets can be coarsely aligned by the calculated transformation model. Then, initial minutiae correspondences are established by the nearest neighbour method, and the final result is achieved by the RANSAC algorithm with a TPS model. This kind of minutiae correspondences establishment is demonstrated in Fig. 5.13.

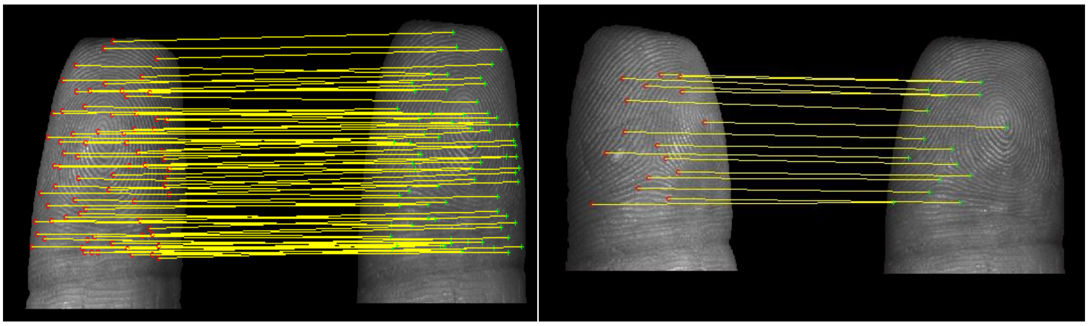

(a) (b)

Fig. 5.13: Minutiae correspondences establishment. (a) Initial correspondences, (b) Final correspondences after RANSAC.

5.4 Finger Shape Model Estimation

To reconstruct the finger shape, it is necessary to know the shape model after certain 3D points of the finger are calculated. Unfortunately, exact model for human's finger shape is not directly available, and hence, it should be estimated. To this end, we propose to estimate the finger shape model by analyzing 440 3D point cloud data collected from human fingers (220 fingers, 2 pictures each) in this chapter. The 3D point cloud data are defined as the depth information of each point on the finger. They are collected by one camera together with a projector using the Structured Light Illumination (SLI) method [122, 130]. The structure diagram of the collection device is shown in Fig. 5.14. 13 structured light stripes generated by a computer are projected onto the finger surface by using the Liquid Crystal Display (LCD) projector. The camera then captures the fingerprint images formed with projected stripes on it. 3D point cloud data, which consists of depth information of each point on the finger, can be calculated using transition and phase expansion techniques [131]. Since this technique is well studied and proved to acquire 3D depth information of each point on the finger with high accuracy [122-124, 130-132], 3D point cloud data obtained using this technique are taken as the ground truth of the human finger to build the database for finger shape model estimation.

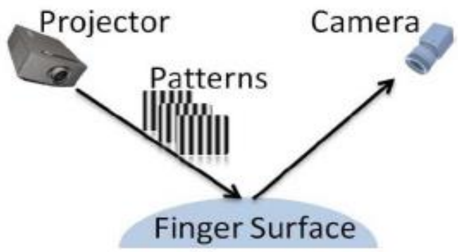

Fig. 5.14: Structure diagram of device used to capture 3D point cloud data of human finger [122].

Fig. 5.15(a) displays an example of 3D point cloud data we collected from a thumb. We randomly selected and drew the horizontal profile and the vertical profile of the 3D point cloud data, as shown in Fig. 5.16 (green labeled), while the vertical profile can be represented by a quadratic curve or a logarithmic function (see Fig. 5.16(b)). Thus, both of the binary quadratic function

$$f_1(x, y) = Ax^2 + By^2 + Cxy + Dx + Ey + F \tag{5.2}$$

and the mixed model with parabola and logarithmic function

$$f_2(x, y) = Ax^2 + Bx + C\ln(y) + D \tag{5.3}$$

are chosen to fit all of our collected 440 3D point cloud finger data by the regression method [133, 134]. Note that, in Eq. 5.2 and Eq. 5.3, *A*, *B*, *C*, *D*, *E*, and *F* represent the coefficients of the function, x is the variable of column-coordinate of the image and y is the variable of row-coordinate of the image. Fig. 5.15(b) gives the fitting result of Fig. 5.15(a) (denoted by *V*) by the binary quadratic function (denoted by $\tilde{V}_{Eq.2}$), while Fig. 16(c) gives the fitting result of Fig.

5.15(a) by the mixed model (represented by $\tilde{V}_{Eq.3}$). Table 5.2 gives the errors measured by the mean distance and the standard variation between the estimated finger shape and the original 3D point cloud data in Fig. 16(a). It can be seen that the error between V and $\tilde{V}_{Eq.2}$ is smaller than the one between V and $\tilde{V}_{Eq.3}$. Next, the errors between the 3D point cloud data and their corresponding fitting results of all 440 fingers we collected are computed. It can be seen from Fig. 5.17 that the binary quadratic function is more suitable for the finger shape model since smaller errors are obtained between the original 3D point cloud data and their corresponding fitting results by the binary quadratic function. For this reason, the binary quadratic function is chosen as the finger shape model in this chapter.

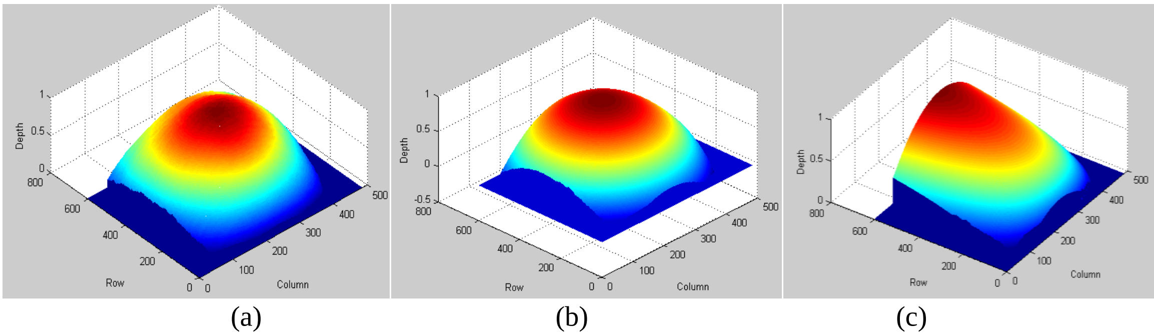

Fig. 5.15: Example 3D finger point cloud data and its fitting results by different models. (a) 3D point cloud data of a thumb, (b) Fitting result of (a) by binary quadratic function, (c) Fitting result of (a) by a mixed model with parabola and logarithmic function.

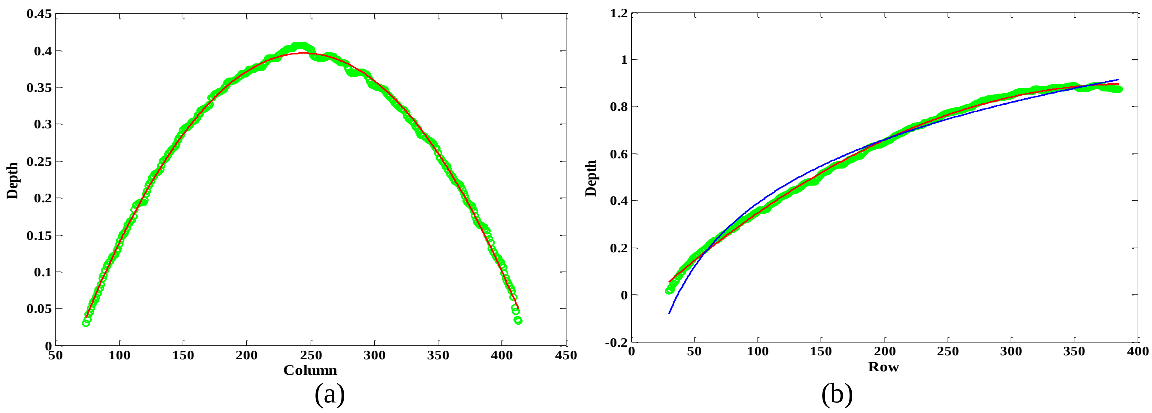

Fig. 5.16: Randomly selected profiles of Fig. 5.15(a). (a) Horizontal profile, green line depicts real data, red line is fitting by Parabola, (b) Vertical profile, green line depicts real data, red line is fitting by Quadratic Curve, blue line is fitting by Logarithmic Function.

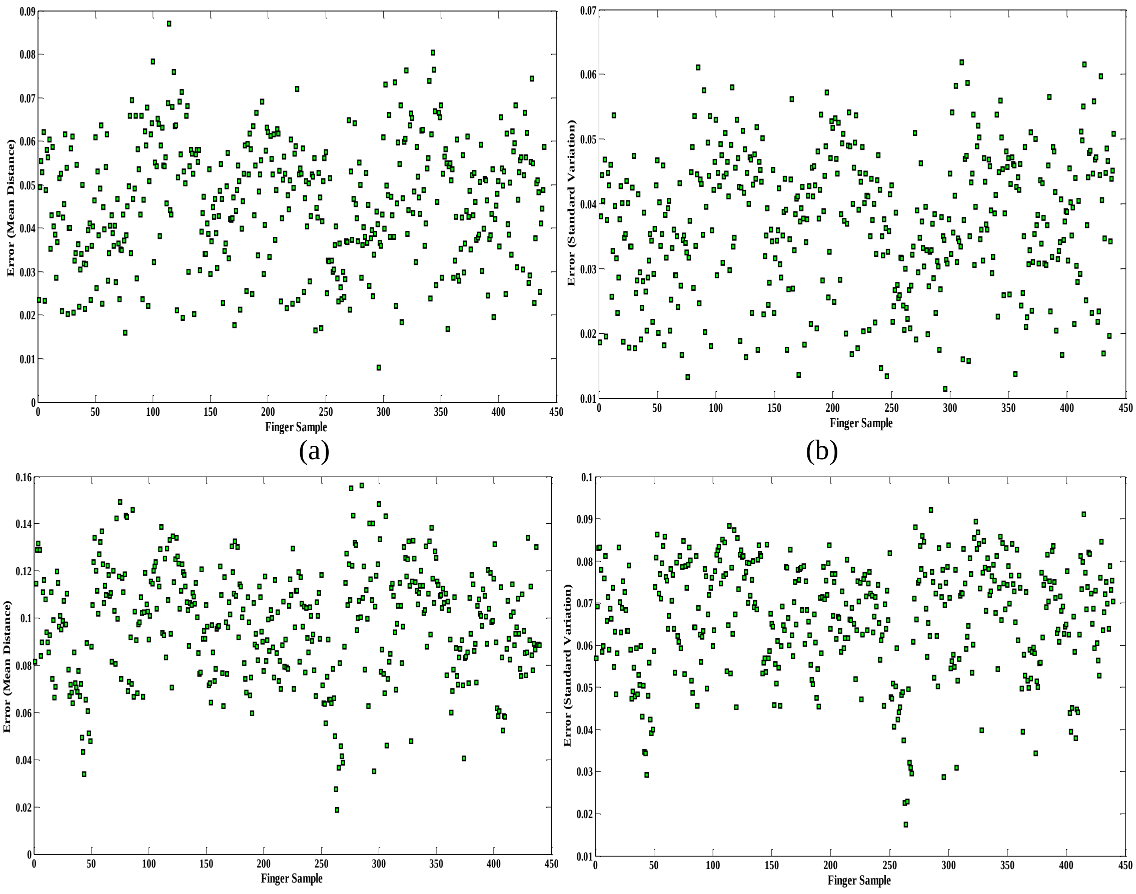

Fig. 5.17: Errors between the original 3D point cloud data of all 440 fingers we collected and their corresponding fitting results by different models. (a) Errors represented by the mean distance between the original 3D point cloud data and their corresponding fitting result by binary quadratic function, (b) Errors represented by the standard variation between the original 3D point cloud data and their corresponding fitting result by binary quadratic function, (c) Errors represented by the mean distance between the original 3D point cloud data and their corresponding fitting result by the mixed model, (d) Errors represented by the standard variation between the original 3D point cloud data and their corresponding fitting result by the mixed model.

Table 5.2: Mean distance and standard variation of error map between estimated finger shape and real finger shape of example images in Fig. 5.15.

Index Factor / **Fitting Model Function**	**Mean Distance** $mean\left(V-\tilde{V}\right)$	**Standard Variation** $std\left(V-\tilde{V}\right)$
$f_1\left(x,y\right)$	0.024	0.019
$f_2(x,y)$	0.082	0.057

5.5 Experimental Results and Analysis

5.5.1 3D Fingerprint Reconstruction System Error Analysis

Reconstruction and system errors are inevitable. To acquire these errors, the reconstruction of an object with standard cylinder shape and of radius 10*mm* is given. The example object is shown in Fig. 5.18(a). The surface of the object is wrapped by a grid chapter to facilitate feature extraction. Three 2D pictures (left-side, frontal, and right-side) of the cylinder are then captured by the proposed touchless multi-view imaging device. Fig. 5.18(b) and Fig. 5.18(c) show two grouped images (left-side & frontal, right-side & frontal). As mentioned in section 5.2, there are five main steps in our reconstruction technique. Camera parameters are firstly calculated off-line. The corner features of the wrapped grid chapter are then labeled and their correspondences between grouped images are established manually, as shown in Fig. 5.18(b) and Fig. 5.18(c). Fig. 5.18(d) and Fig. 5.18(e) illustrate the calculated 3D coordinates corresponding to the matched pairs shown in Fig. 5.18(b) and Fig. 5.18(c) based on the given camera parameters and feature correspondences. Shape model estimation is unnecessary since the cylinder model is known as a prior knowledge. By using the calculated 3D coordinates and the known shape model of cylinder, the cylindrical surface is finally generated by interpolation based on the multiple linear regressions using the least squares method [132, 133]. Fig. 5.18(f) and Fig. 5.18(g) are the reconstructed cylinders shown by a 3D display software called Imageware 12.1. This software is used for 3D point cloud data display and analysis. The error maps shown in Fig. 5.18(h) and Fig. 5.18(i) are also obtained by this software too. From Fig. 5.18(f) and Fig. 5.18(g), we can see that the radius of reconstructed cylinders from 40 3D points of Fig. 5.18(d) and Fig. 5.18(e) are ~9.91*mm* and ~9.84 *mm* compared with the real radius 10*mm*. Fig. 5.18(h) and Fig. 5.18(i) give the error maps of 3D points corresponding to Fig. 5.18(d) and Fig. 5.18(e) when fitting by cylinder shape with radius of 10*mm*. The error ranges are [-0.07*mm* ~ 0.06*mm*] and [-0.1*mm* ~ 0.06*mm*] respectively. The results demonstrate that the reconstruction error of our device is within ~0.2*mm*.

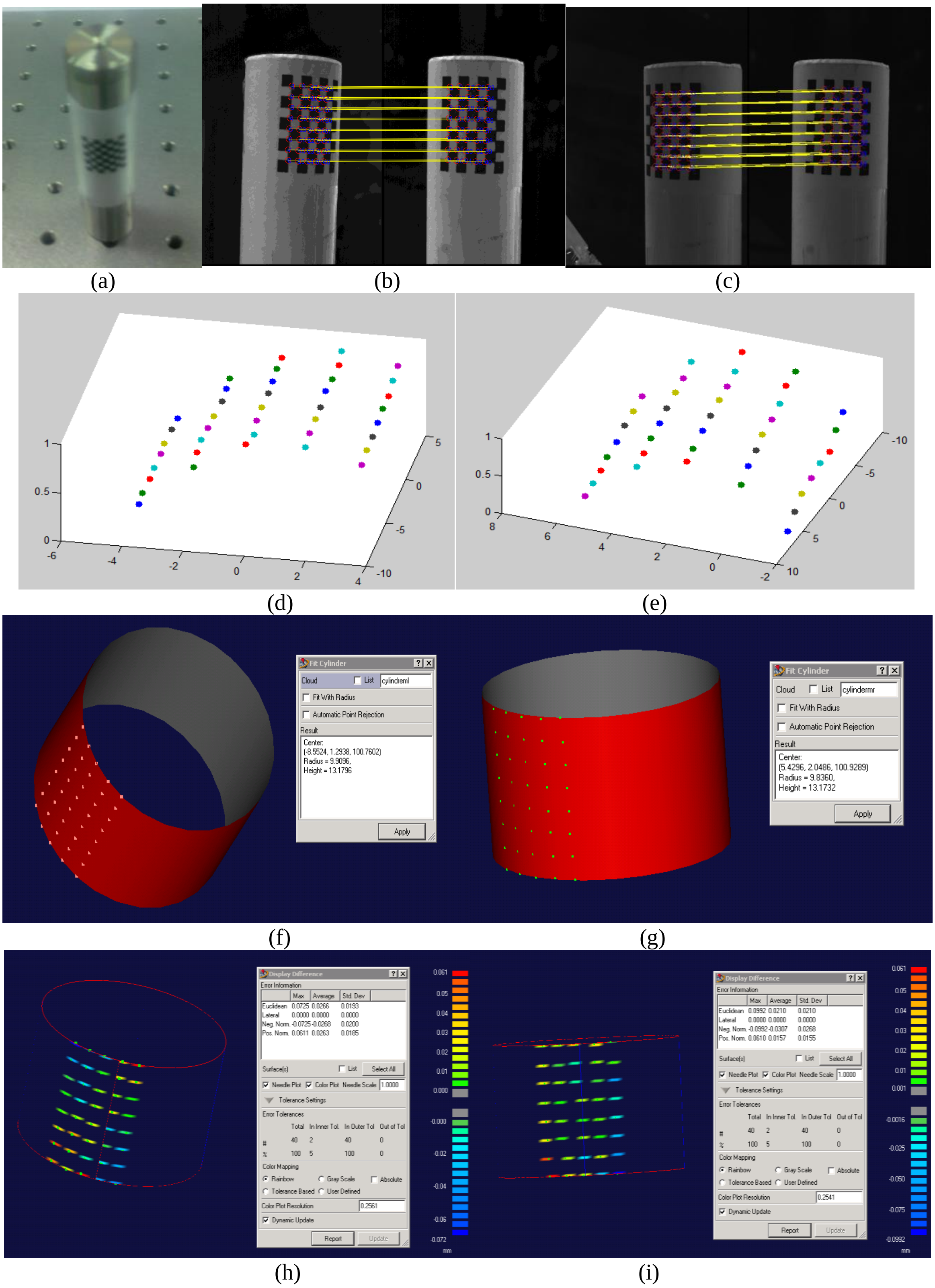

Fig. 5.18: Reconstruction accuracy analysis of cylinder shape object. (a) Original cylinder shape object wrapped with grid chapter, (b) Correspondences established between left-side and frontal images captured by our device, (c) Correspondences established between right-side and frontal images captured by our device, (d) 3D space points corresponding to (b), (e) 3D space points corresponding to (c), (f) Fitting result corresponding to (d), (g) Fitting result corresponding to (e), (h) Error map corresponding to (d) when fitting by cylinder shape with radius of 10*mm*, (i) Error map corresponding to (e) when fitting by cylinder shape with radius of 10*mm*.

5.5.2 Comparison and Analysis of Reconstruction Results based on Different Fingerprint Feature Correspondences

By following the five steps we introduced in section 5.2, reconstructed 3D fingerprint images can be obtained. Since there are three fingerprint images captured at one time and the central camera is selected as the reference system, the proposed reconstruction consists of two parts (left-side camera and central camera, right-side camera and central camera) according to binocular stereo vision theory. Thus, we combined two parts of our system before the fourth steps by normalizing the calculated depth value of correspondences into [0, 1]. Here, the Min-Max strategy of normalization is used. This combination is adopted for two reasons. One is that there are parts of overlapping region between two adjacent fingerprint images, the distribution of correspondences may focus on a small part of fingerprint images. Larger areas of fingerprint image can be covered by discrete correspondences through combining two parts of our system. The other is that it is very simple to accomplish and system error of combining two parts before model fitting is alleviated. Table 5.3 then shows the reconstruction results based on three different fingerprint feature correspondences we used of an example images shown in Fig. 5.19. We can see that the results are different corresponding to different feature matched pairs due to quite different numbers and distribution of established fingerprint feature correspondences and the existence of false correspondences.

Fig. 5.19: Example fingerprint images captured by our device (left, middle, right).

To investigate which features are more suitable for 3D fingerprint reconstruction, we also manually labeled fingerprint correspondences, as shown in Fig. 5.20. The histogram of error map between reconstructed results in Table 5.3 and Fig. 5.20 is shown in Fig. 5.21. The results show that for single feature used, a reconstruction result based on SIFT features achieves the best result, while the ridge feature-based is the worst one. When combining with other features, best reconstruction results can be generated if all three features of correspondences are used. However, comparable results are obtained by using SIFT and minutiae. Considering the computational complexity, it is recommended to simply use SIFT and minutiae.

Table 5.3: Reconstruction results from different fingerprint feature correspondences of Fig. 5.19.

Results / Used feature	Established correspondences	Reconstructed 3D fingerprint image
SIFT feature	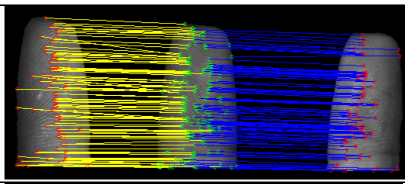	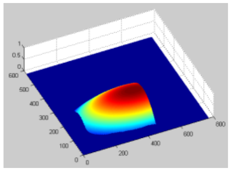
Minutiae	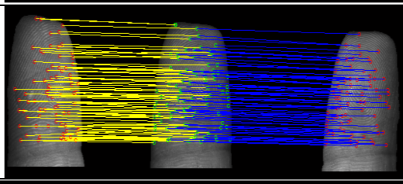	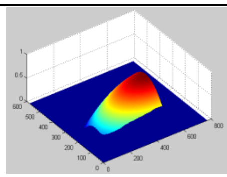
Ridge feature	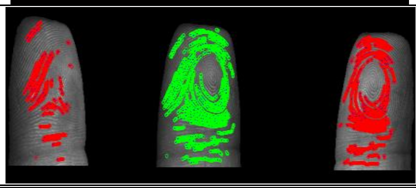	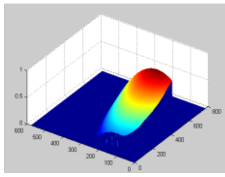
Feature Combination	**Reconstructed 3D fingerprint image**	
SIFT feature and minutiae	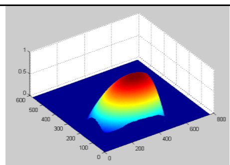	
SIFT and ridge feature	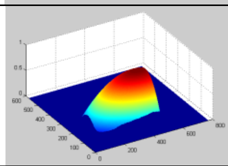	
Minutiae and ridge feature	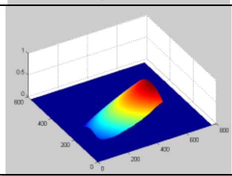	
SIFT feature, minutiae and ridge feature	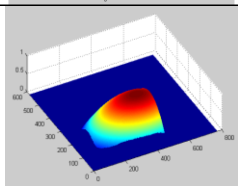	

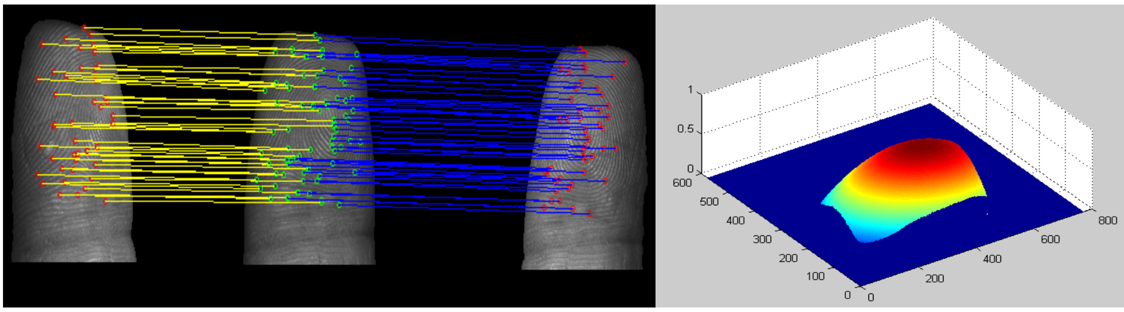

(a) (b)

Fig. 5.20: Reconstruction of 3D finger shape of Fig. 5.19. (a) Manually labeled correspondences between fingerprint images, (b) Reconstructed 3D finger shape based on (a).

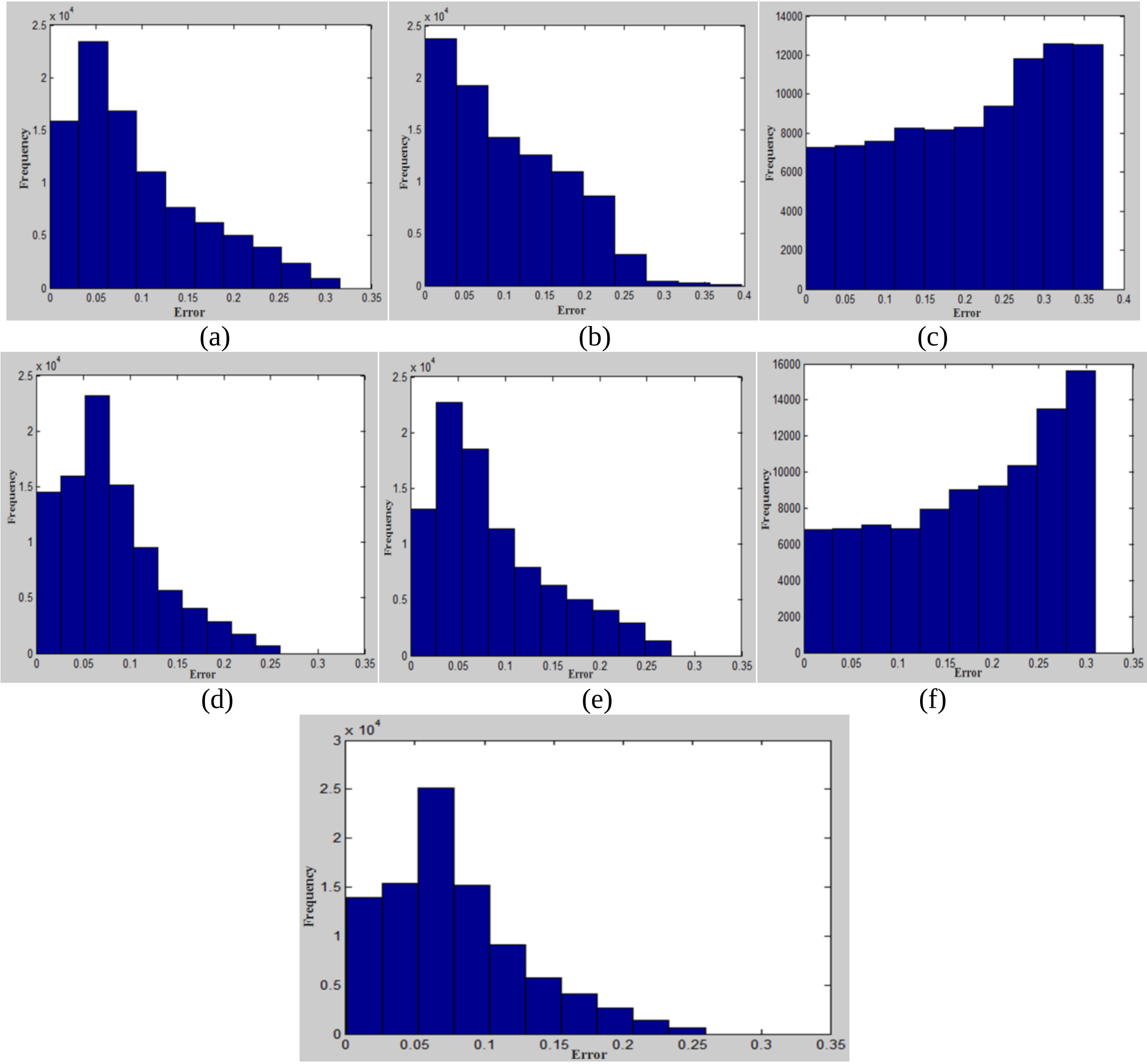

(a) (b) (c)

(d) (e) (f)

(g)

Fig. 5.21: Histogram of error maps between reconstructed results in Table 5.3 and Fig. 5.20(b). (a) Histogram of err map between Fig. 5.20(b) and reconstruction result by using SIFT feature only, (b) Histogram of err map between Fig. 5.20(b) and reconstruction result by using minutiae only, (c) Histogram of err map between Fig. 5.20(b) and reconstruction result by using ridge feature only, (d) Histogram of err map between Fig. 5.20(b) and reconstruction result by using both SIFT feature and minutiae, (e) Histogram of err map between Fig. 5.20(b) and reconstruction result by using both SIFT feature and ridge feature, (f) Histogram of err map between Fig. 5.20(b) and reconstruction result by using both minutiae and ridge feature, (g) Histogram of err map between Fig. 5.20(b) and reconstruction result by using SIFT feature, minutiae and ridge feature.

5.5.3 Validation of Estimated Finger Shape Model

Since the final 3D finger shape is obtained after interpolation according to the prior estimated finger shape model, we compared the reconstruction result with the 3D point cloud data of the same finger to verify the effectiveness of the model. From the results shown in Fig. 5.21, it can be seen that the profile of finger shape reconstructed from multi-cameras is similar to the 3D point cloud data even though not as accurate as it. The real distance between upper left core point and the left down delta point is also calculated and shown in Figs. 5.22(a) and (c), the values are 0.357 and 0.386 respectively. As a result, it is concluded that the estimated finger shape model is effective even though there is error between the reconstruction result and the 3D point cloud data.

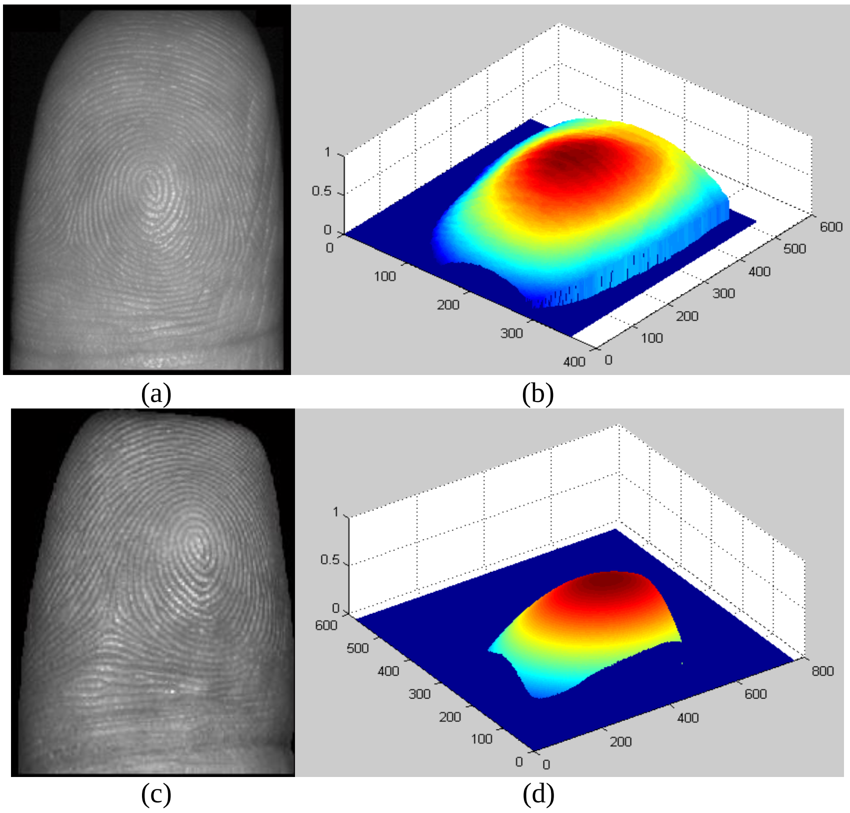

Fig. 5.22: Comparison of 3D fingerprint images from the same finger but different acquisition technique. (a) Original fingerprint image captured by the camera when collecting 3D point cloud, (b) 3D point cloud collected by one camera and a projector using the SLI method, (c) Original fingerprint image captured by our device, (d) Reconstructed 3D fingerprint image with labeled correspondences.

5.5.4 Reconstruction System Computation Time Analysis

There are six main parts included in our reconstruction system from image acquisition to result generation, as the block diagram shows in Fig. 5.3. The reconstruction method is implemented by Matlab on Fujitsu notebook embedded Intel Core 2 Duo CPU, T9600 (2.80GHz) processor. For image acquisition, it consumes no more than 100ms to capture three views of fingerprint images since the frame rate of each camera is 30 frames/sec. Because both of the camera parameters calculation and shape model estimation are done off-line, they do not occupy any time in the whole system. The correspondences establishment step consists of feature extraction and matching, which consumes considerable time. This time is variable for different images. The average time statistically calculated in our database is then used to represent. They are ~60.3sec. and ~24.32sec., respectively. It takes ~0.31sec. to compute the 3D coordinates of feature correspondences. For interpolation, the code included in the matlab toolbox is employed and the consumption time is ~1.21sec. To summarize, it takes ~1.5min. to generate a 3D image by using the proposed system. It is believed, however, this time will be largely reduced once compiling the code by C/C++ language and using the multithread processing technique.

5.6 Summary

This chapter investigates a 3D reconstruction technique based on limited feature correspondences in 2D fingerprint images captured by our own designed multi-view touchless fingerprint imaging device. Specific to the characteristics of low ridge-valley contrast of touchless fingerprint images, we improved fingerprint enhancement method, so as to extract more robust fingerprint features. Then, three frequently used features, i.e., SIFT feature, ridge feature and minutiae, which have characteristics of different numbers and various distributions, are considered for correspondence establishment. Correspondences are finally established by adopting the hierarchical fingerprint matching approaches. The finger shape model in this chapter is estimated by analyzing 3D point cloud finger data collected by one camera and a projector using the SLI method. Results show that the binary quadratic function is more suitable for the finger shape model compared with another mixed model proposed in the chapter. By reconstructing a standard cylinder object, it is shown that it is reasonable and feasible for the adopted methodology of reconstruction technique and the capturing device. The comparison and analysis of 3D fingerprint reconstruction results from different fingerprint feature correspondences illustrates best reconstruction results can be generated if all three features of correspondences are used. However, it is recommended to simply use SIFT and minutiae since comparable results are achieved by using them. The effectiveness of the estimated finger shape model is verified by comparing the reconstructed 3D finger shape with the corresponding 3D point cloud finger data.

Chapter 6

3D Fingerprint Recognition Using Curvature Features

Human finger is a three-dimensional object. More information will be provided if 3D fingerprint images are available compared with 2D fingerprints. Since we obtained the 3D fingerprint images according to the reconstruction technique introduced in the last chapter, this chapter explores 3D fingerprint features and their applications for personal authentication. We define the 3D finger structural features, such as curve-skeleton and overall maximum curvatures, as Curvature Fingerprint Features in this chapter and investigate their distinctiveness for user authentication. These features are also used to assist fingerprint matching and make contribution to fingerprint recognition by combining with 2D fingerprint features. A series of experiments are conducted to evaluate 3D fingerprint recognition technique based on our established database with 541 fingers. Results show that an EER ~15% can be achieved when using 3D curve-skeleton for recognition. The overall maximum curvatures can be used for human gender classification and an EER of ~19% is obtained on our database. Promising EER of 3.4% is realized by including curve-skeleton feature into fingerprint recognition which indicates the prospect of 3D fingerprint recognition.

6.1 Introduction

As one of the most widely used biometrics, fingerprint has been investigated for more than a century [18]. Effective AFRSs are available with the rapid development of fingerprint acquisition devices and the advent of many advanced fingerprint recognition algorithms. However, they are almost based on 2D fingerprint features, even though the fact is that human finger is a 3D object. There are distortions and deformations introduced and 3D information lost when 2D fingerprint images are used, which cannot perfectly meet people's demands in accuracy, computational complexity. Develop user-friendly AFRSs with high precision and high efficiency is still an open issue in fingerprint recognition domain.

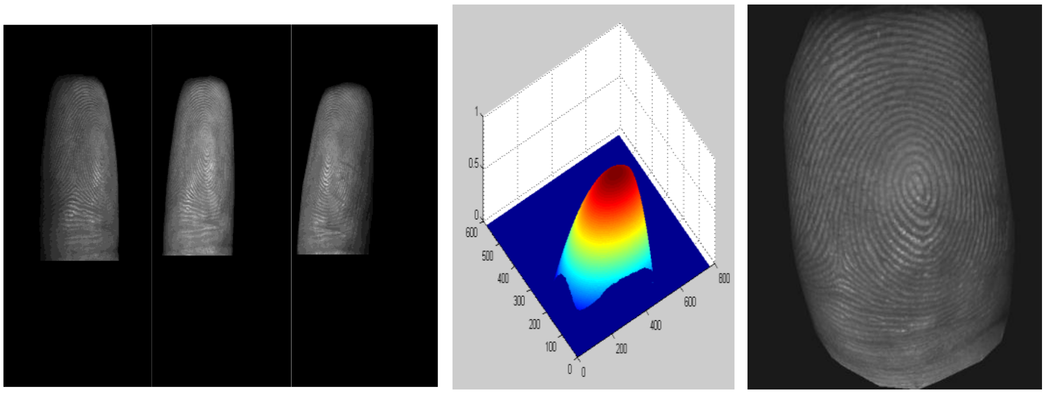

(a) (b) (c)

Fig. 6.1: Example of 2D and reconstructed 3D fingerprint images. (a) Preprocessed images of a finger captured by our device used to reconstruction (left, frontal, right), (b). Reconstructed 3D finger shape, (c) 3D fingerprint image.

With the expansion of acquisition technology, 3D biometric authentication techniques come into researchers' view in recent years, such as 3D face [143, 144], 3D ear [145-147] and 3D palmprint recognition [132, 148-150]. For 3D fingerprints, even though there are some works about 3D fingerprint image acquisition and processing [35, 122], they did not investigate the utility of 3D fingerprint features and did not report any experimental results of user authentication using the acquired biometric information. This has motivated us to explore the utility of 3D fingerprint features and the possibility of combining them with 2D features for fingerprint recognition. Fig. 6.1 gives an example 3D fingerprint image obtained from last Chapter. The contributions of this chapter include: i) This chapter, for the first time, investigates features on 3D fingerprint images, including Curvature Features for fingerprint recognition, the corresponding feature extraction and matching methods are proposed. More specifically, the 3D finger Curvature Features, such as curve-skeleton, overall maximum curvatures are firstly defined as Curvature Features, and then extracted, finally Iterative Closest Point (ICP) in 3D space is adopted to matching; ii) By analyzing their distinctiveness, 3D fingerprint Curvature Features are used for different applications. We found curve-skeleton are suitable for assisting fingerprint recognition while overall surface can be used for gender classification. Fusion strategy is employed to combine 2D and 3D fingerprint matching results to figure out the effectiveness of improving recognition accuracy by including 3D fingerprint features.

6.2 Definition of Curvature Features in 3D Fingerprint Images

Fingerprints are distinguished by their features. In general, fingerprint features in 2D images are classified into three levels [12]. Level 1 features are defined as the macro details of fingerprints such as singular points and global ridge patterns, e.g. deltas and cores. They are mainly used for fingerprint classification or indexing rather than recognition since they are not very distinctive. Level 2 features are minutiae (ridge endings and bifurcations). These features are the most distinctive and stable ones, which are used in almost all AFRSs [12, 18, 57]. Level 3 features often refer to the dimensional attributes of the ridges including sweat pores and ridge edge features, which are used to assist more robust fingerprint recognition.

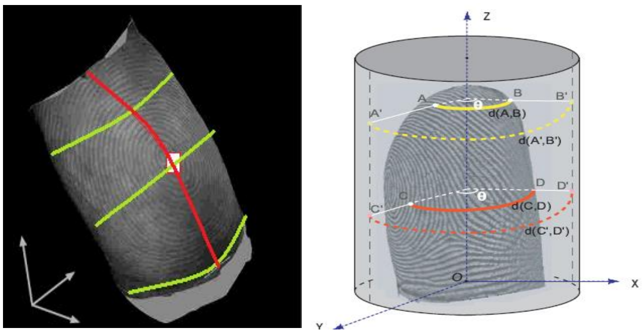

Fig. 6.2: Fingerprint image in 3D space.

Fig. 6.2 shows a fingerprint image in 3D space, we can got that the above defined fingerprint features spread over different scales of depth. For example, core points are located in the center part of the finger with almost the highest depth value. Level 2 and Level 3 features which are closely related with the distribution of ridges actually possess more attributes in 3D space (e.g. depth value, ridge orientation along depth direction). Thus, in 3D fingerprint image, features are coarse than Level 1 features can be obtained (e.g. the contour of the finger). We defined such structural information in 3D fingerprint images as Curvature Fingerprint Features in our chapter. They provide information of overall structure of humans' fingers and indicate the distribution of other features, such as the curve-skeleton [151] and overall maximum curvatures. The curve-skeleton feature depicts the thinned contour of finger shape, as shown in Fig. 6.2 (green and red lines). The overall maximum curvatures describe the maximal horizontal curvature and the maximal vertical curvature of the finger.

6.3 Curvature Features Extraction and Matching

6.3.1 Curvature Feature Extraction

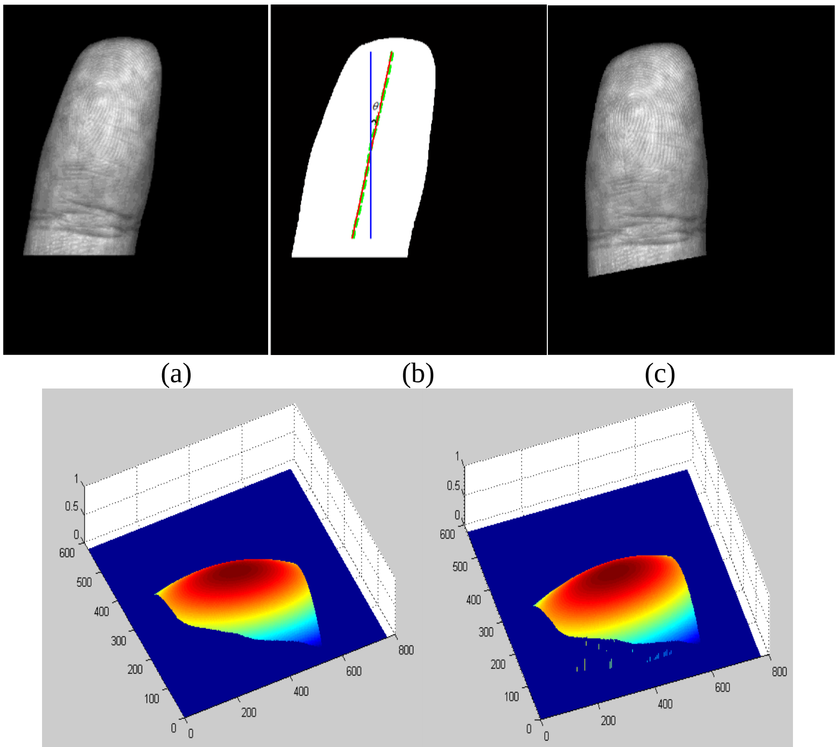

(a) (b) (c)

(d) (e)

Fig. 6.3: Position Correction. (a) Original tilted fingerprint image, (b) ROI extraction of (a), (c) Fingerprint image after pose correction, (d) Original 3D finger shape, (d) Corrected 3D finger shape.

Since our 3D fingerprint image is reconstructed from multi-view fingerprint images, there is a one-to-one correspondence between the 3D points and the 2D fingerprint image pixels. Preprocessing such as ROI extraction and pose correction can be done in 2D fingerprint images, and implemented in 3D situation. The iterative thresholding segmentation method we introduced in Chapter 4 is used in this chapter to extract ROI (see Fig. 6.3(b)). Since it is difficult to control the way users putting their fingers when collecting fingerprint images (tilted fingerprint images, see Fig. 6.3(a)), pose correction is necessary. We proposed to correct the fingerprint images by following steps: i) Find the center point of each row in ROI through horizontal scanning (green dash line in Fig. 6.3(b)); ii) Fit these center point set X by a line $Y = aX$ (red solid line in Fig. 6.3(b)), a is the slope of this line; iii) Calculate the angle between the fit line and the vertical axis (see blue line in Fig. 6.3(b)) $\theta = 90^{\circ} - \tan(a)$; iv) Rotate the original image by angle θ anti-clockwise. The corrected image is finally obtained, as shown in Fig. 6.3(c).

Given a corrected 3D fingerprint image, stable and unique features are expected to be extracted for the following pattern matching and recognition. 3D depth information reflects the overall structure of human finger. However, there are many invalid points in the whole 3D finger shape due to the structure of human finger. Wrinkles and Scars in finger also affect local structure of finger shape. Thus we proposed to extract curve-skeleton of finger shape. As shown in Fig. 6.4, Different 3D objects are almost fully represented by their curve-skeletons.

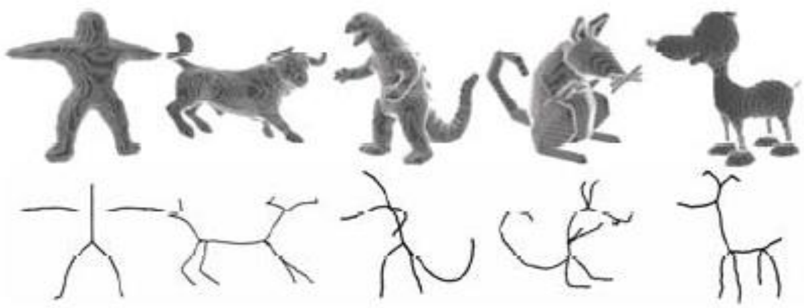

Fig. 6.4: Examples of curve-skeletons of different 3D objects.

Since 3D finger shape model is close to binary quadratic function, profile of horizontal section can be fitted by parabola and reflects the changes of finger width, while vertical profile depicts variation tendency of depth from fingertip to distal interphalangeal crease. The curve-skeleton of 3D fingerprint image we used here is a medial axis/surface approach. It consists of representative vertical and horizontal lines. Since each horizontal profile is parabola-like shape, we extracted the extreme value of each fitted parabola line to form the representative vertical line (blue line in Fig. 6.5(a)). Three representative horizontal lines are selected at a certain step length (100). The distal interphalangeal crease is chosen as the base line (see green line in Fig. 6.5(a)). Fig. 6.5(b) shows the curve-skeleton we extracted from 3D finger depth map. For overall maximum curvatures, they can be easily calculated since our 3D finger shape is reconstructed by model fitting. The coefficients of the binary quadratic function control the maximal horizontal and vertical curvatures of 3D finger, namely the parameters of *A* and *B* in Eq. 5.2. Thus, these two coefficients of the binary quadratic function are maintained to represent the maximal horizontal and vertical curvatures, namely the defined overall maximum curvatures.

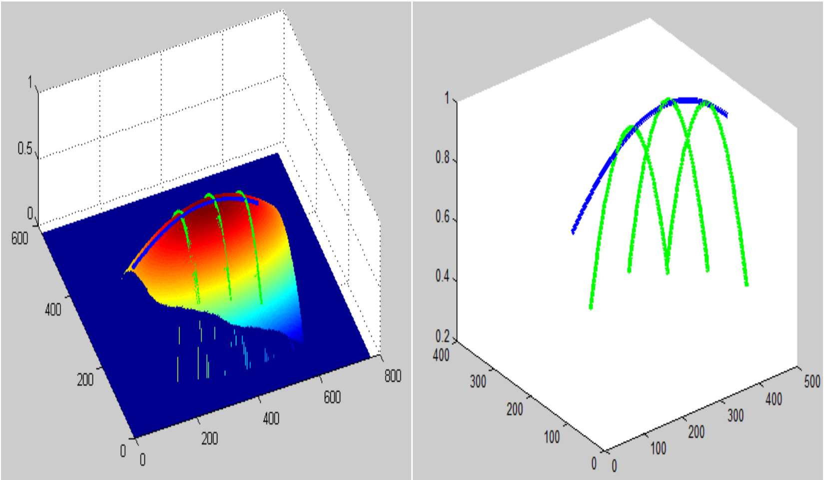

(a) (b)

Fig. 6.5: Examples of curve-skeleton for 3D finger. (a) 3D finger shape, (b) Extracted curve-skeleton.

6.3.2 Curvature Features Matching

From Fig. 6.5(b), we can see that curve-skeleton consists of several 3D lines. Intuitively, the iterative closest point (ICP) algorithm is suitable for solving such matching problem. ICP method [117] is widely used in many 3D object recognition systems for matching. In this chapter, we slightly modified the ICP method to measure the distances between two sets of points. The algorithm is given in the box below and Fig. 6.6 shows an example of matching two curve-skeletons by our modified ICP method.

1. Input: Model point set: D_1; Test point set D_2;
2. Parameters initialization: stop criterion for distance Td=0.1; intial rotation matrix R_0=I; initaltranslation vector $T_0=[0\ 0\ 0]^T$;
3. While (new correspondences set found between D_1 and D_2))

   { [corr, D_i]=dsearchn(D_1 , D_2);

   $K_i=D_i>Td$;

   Discard corr(K_i);

   Update R_i, T_i;

   $D_2=R_i* D_2+T_i$;}
4. Output: distance vector D, registered D_2, rigid transform paramters: R and T.

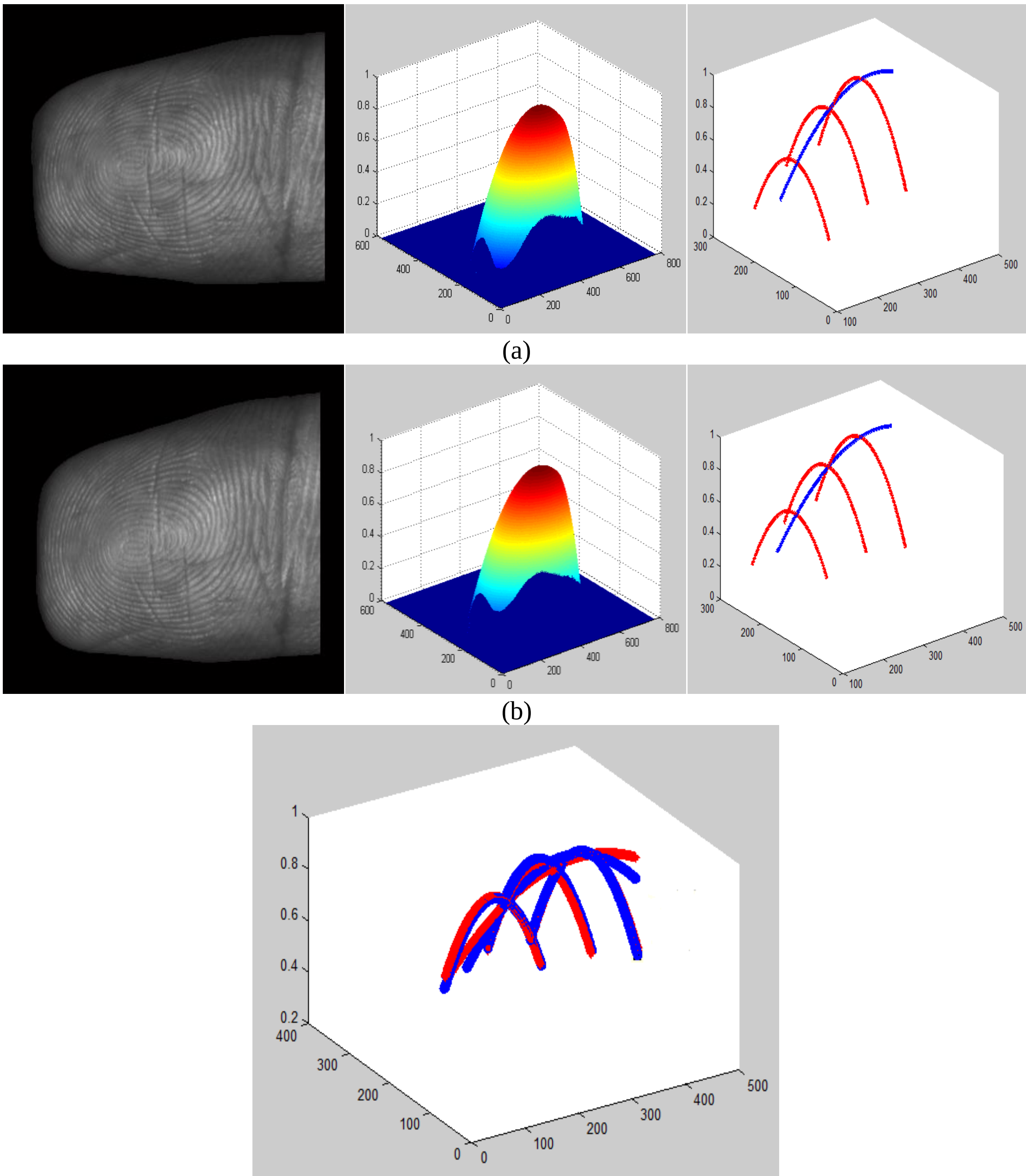

(a)

(b)

(c)

Fig. 6.6: Example of curve-skeleton matching by ICP method. (a) The model 2D fingerprint image, 3D finger shape, and extracted curve-skeleton feature, (b) The test 2D fingerprint image, 3D finger shape, and extracted curve-skeleton feature, (c) Matching result by ICP method.

Overall maximum curvatures are represented by single values, which can be taken as match scores directly. Thus, they can be compared directly after they are extracted.

6.4 Case Studies

6.4.1 Database

It is notable that our 3D fingerprint images consist of the reconstruction results from a touchless multi-view fingerprint imaging device introduced in Chapter 4 and the 3D reconstruction techniques we proposed is introduced in Chapter 5. Our experiments are then implemented on our reconstructed 3D fingerprint Database with 541 fingers, including 223 female fingers and 318 male fingers. For each finger, there are 2 pictures which captured at separate sessions from one week to several months.

6.4.2 Case 1: Curve-skeleton based Recognition

To study the distinctiveness of curve-skeleton features of human fingers, we show examples of matching results of different gender and different fingers. As shown in Table 6.1, examples of curve-skeletons from a female and a male with thumb, index finger and little finger captured at different sessions are given.

We then matched them by ICP method. The percentage of matched points (Pm) and the mean distance between matched pairs (Mdist) are taken as the match score. We firstly matched the curve-skeletons from the same finger but captured at different time, as listed in Table 6.2. Results show that the mean distance between matched pairs are smaller than 1 and the percentage of matched points are larger than 70%. Fig. 6.7 also shows the matching results of different gender and finger types, the match scores are listed in Table 6.3. The results show that big difference existed between different fingers and different genders in curve-skeleton, since such feature reflects the finger width feature and curvatures of fingers.

Fingerprint recognition experiment based on curve-skeletons is then implemented on our established database. Fig. 6.8 shows the ROCs of different match score indexes. The EERs were obtained from 541 genuine scores and 292,140 imposter scores (generated from 541 fingers, 2 pictures of each finger). From the results, we can see that an EER of around 15% can be obtained when matching 3D fingerprint curve-skeleton feature by simple ICP algorithm. The index of mean distance between matched pairs is better than the percentage of matched points. Curve-skeleton feature of 3D fingerprint image can be used to distinguish different fingers even though it is not as accurate as other higher level fingerprint features.

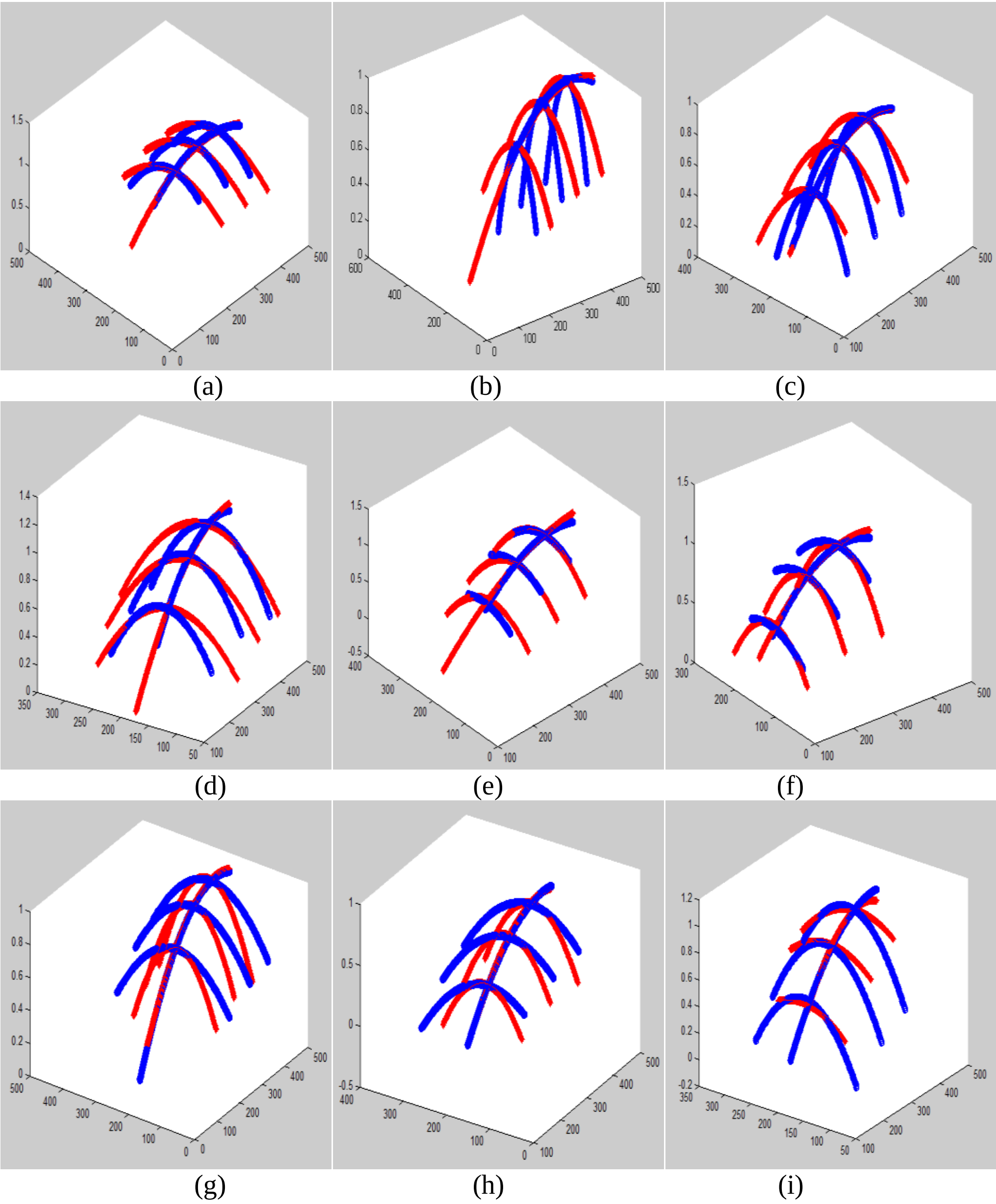

Fig. 6.7: Example of matching results of curve-skeletons from different gender and finger types. (a) Matching result of [(male, thumb)--(male, index finger)] in Table 6.1, (b) Matching result of [(male, thumb)--(male, little finger)] in Table 6.1, (c) Matching result of [(male, index finger)--(male, little finger)] in Table 6.1, (d) Matching result of [(female, thumb)--(female, index finger)] in Table 6.1, (e) Matching result of [(female, thumb)--(female, little finger)] in Table 6.1, (f) Matching result of [(female, index finger)--(female, little finger)] in Table 6.1, (g) Matching result of [(male, thumb)--(female, thumb)] in Table 6.1, (h) Matching result of [(male, index finger)--(female, index finger)] in Table 6.1, (i) Matching result of [(male, little finger)--(female, little finger)] in Table 6.1.

Since both 2D fingerprint features and 3D structural features are provided simultaneously by 3D fingerprint images, we aim to study whether improved performance can be achieved by combining 2D and 3D fingerprint features. For 2D fingerprint features, we selected minutiae due to their distinctiveness and popularity. It was extracted and matched by the method proposed in [111]. The percentage of matched minutiae pairs was taken as the match score (MS_{2D}). Meanwhile, the curve-skeleton feature was chosen as the 3D structural fingerprint feature and mean distance between matched pairs was taken as the match score (MS_{3D}). A simple adaptive weighted sum rule is used to combine the 2D and 3D matching scores. The combined score can be expressed as:

$$MS_{2D+3D} = w / MS_{3D} + (1-w) \times MS_{2D} \quad w \in [0,1] \tag{6.1}$$

The weight *w* is adaptively tuned to provide the best verification results at step length of 0.01.

Fig. 6.9 shows the ROCs achieved by using minutiae and curve-skeleton separately, as well as their combination. It is notable that minutiae clearly outperforms curve-skeleton in terms of accuracy. However, the best result is achieved when combining minutiae and curve-skeleton feature where an EER of 3.4% is obtained. This experiment fully demonstrates that higher accuracy can be achieved if 3D fingerprint images are used compared with 2D fingerprint recognition.

Table 6.1: Examples of extracted Curve-skeletons from different gender and different fingers.

Finger Type \ Gender		Male		Female	
		Orignial 2D image	Curve-skeleton	Orignial 2D image	Curve-skeleton
Thumb	Session 1 (a1)		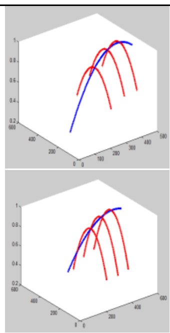	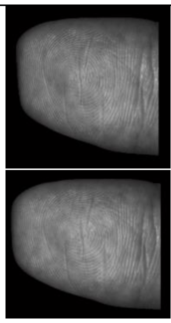	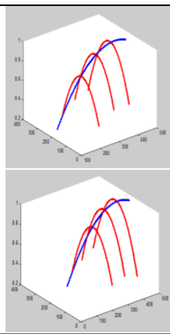
	Session 2 (a2)				
Index Finger	Session 1 (b1)	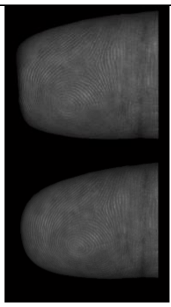	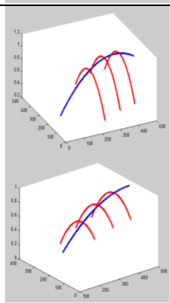	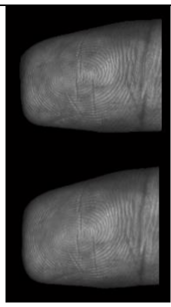	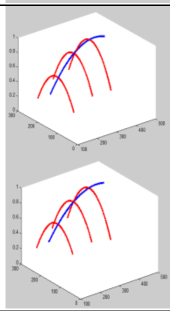
	Session 2 (b2)				
Little Finger	Session 1 (c1)	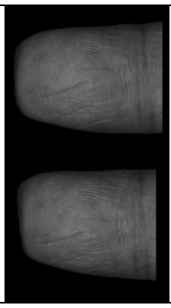	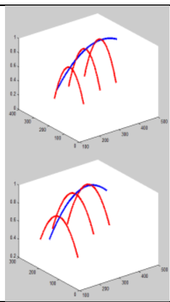	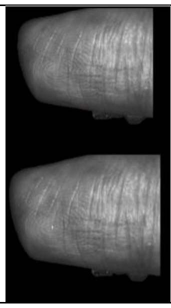	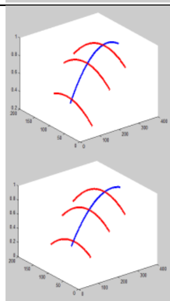
	Session 2 (c2)				

Table 6.2: Matching results based on Curve-skeletons from the same finger but different session.

Finger Type \ Gender	Thumb	Index Finger	Little Finger
	(a1)—(a2)	(b1)—(b2)	(c1)—(c2)
Male	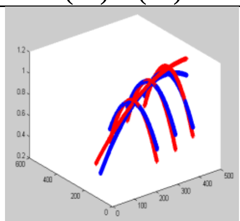	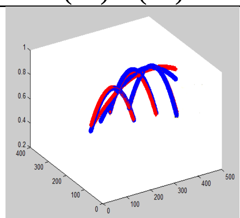	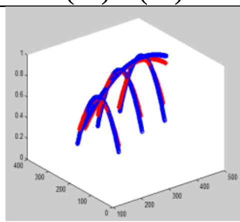
	Pm=74%; Mdist=0.20	**Pm=93%; Mdist=0.39**	**Pm=79%; Mdist=0.25**
Female	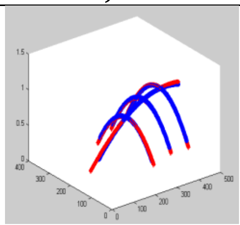	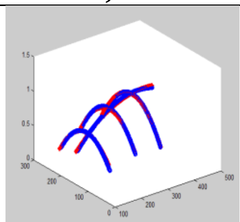	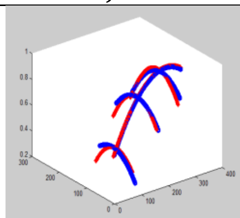
	Pm=94%; Mdist=0.72	**Pm=97%; Mdist=0.09**	**Pm=90%; Mdist=0.32**

Table 6.3: Matching scores corresponding to Fig. 6.7.

Index \ Label	(a)	(b)	(c)	(d)	(e)	(f)	(g)	(h)	(i)
Pm (%)	57	38	53	55	45	62	50	53	57
Mdist	8.3	13.7	2.9	6.8	14.8	3.1	4.0	4.1	4.6

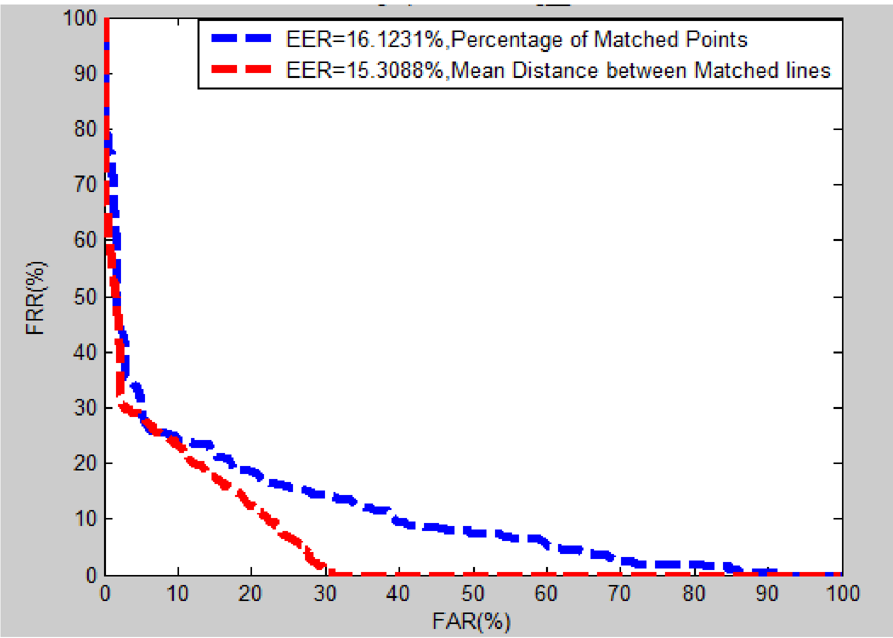

Fig. 6.8: ROC curves for 3D fingerprint matching by ICP with curve-skeleton feature.

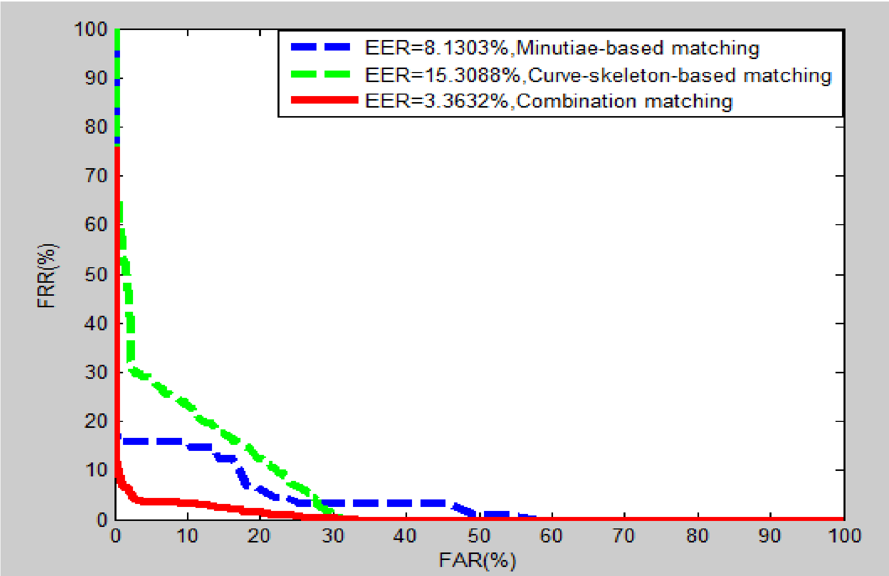

Fig. 6.9: ROC curves for fingerprint matching by different fingerprint features.

6.4.3 Case 2: Overall Maximum Curvatures based Gender Classification

Since our 3D fingerprint images are generated by reconstruction where binary quadratic function is taken as the finger shape model, two parameters are used to depict the overall finger shape curvature. Fig. 6.10 shows the values of maximal horizontal Curvature feature and maximal vertical Curvature feature in our database. We found both of these Curvature features are very small. They cannot be used for personal authentication. Thanks to the composition of database of different gender, we investigated whether this feature is useful for gender classification. We then plot the distribution maps of norm Curvature Features separated by gender, as shown in Fig. 6.11. The ROCs are also shown in Fig. 6.11. From the figure, we found that the vertical maximum curvature can reach an EER of around 19%, while horizontal maximum curvature disabled to classify genders. It shows that there is little difference in the horizontal profile no matter male or female but the vertical profile is different.

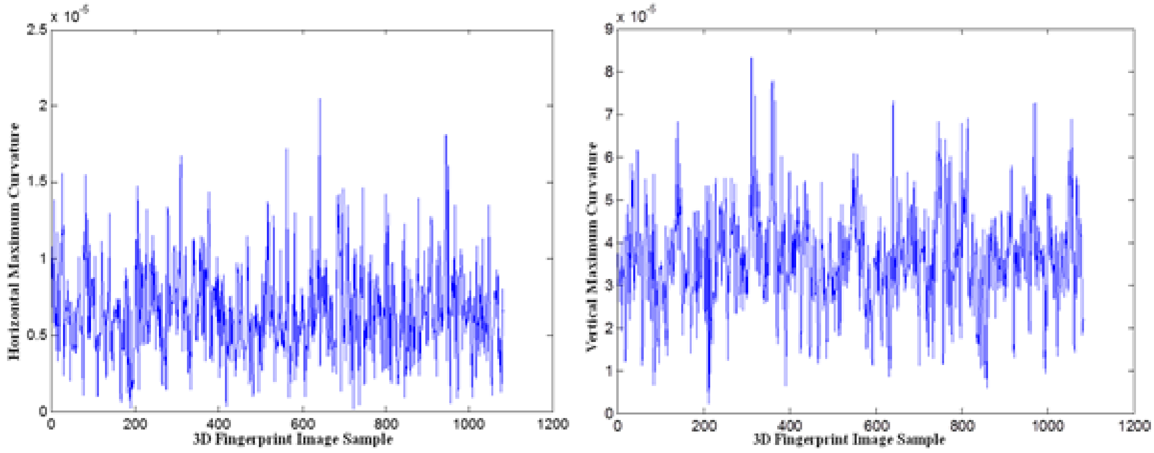

(a) (b)

Fig. 6.10: Values of overall maximum curvature on our database. (a) Horizontal maximum curvature, (b) Vertical maximum curvature.

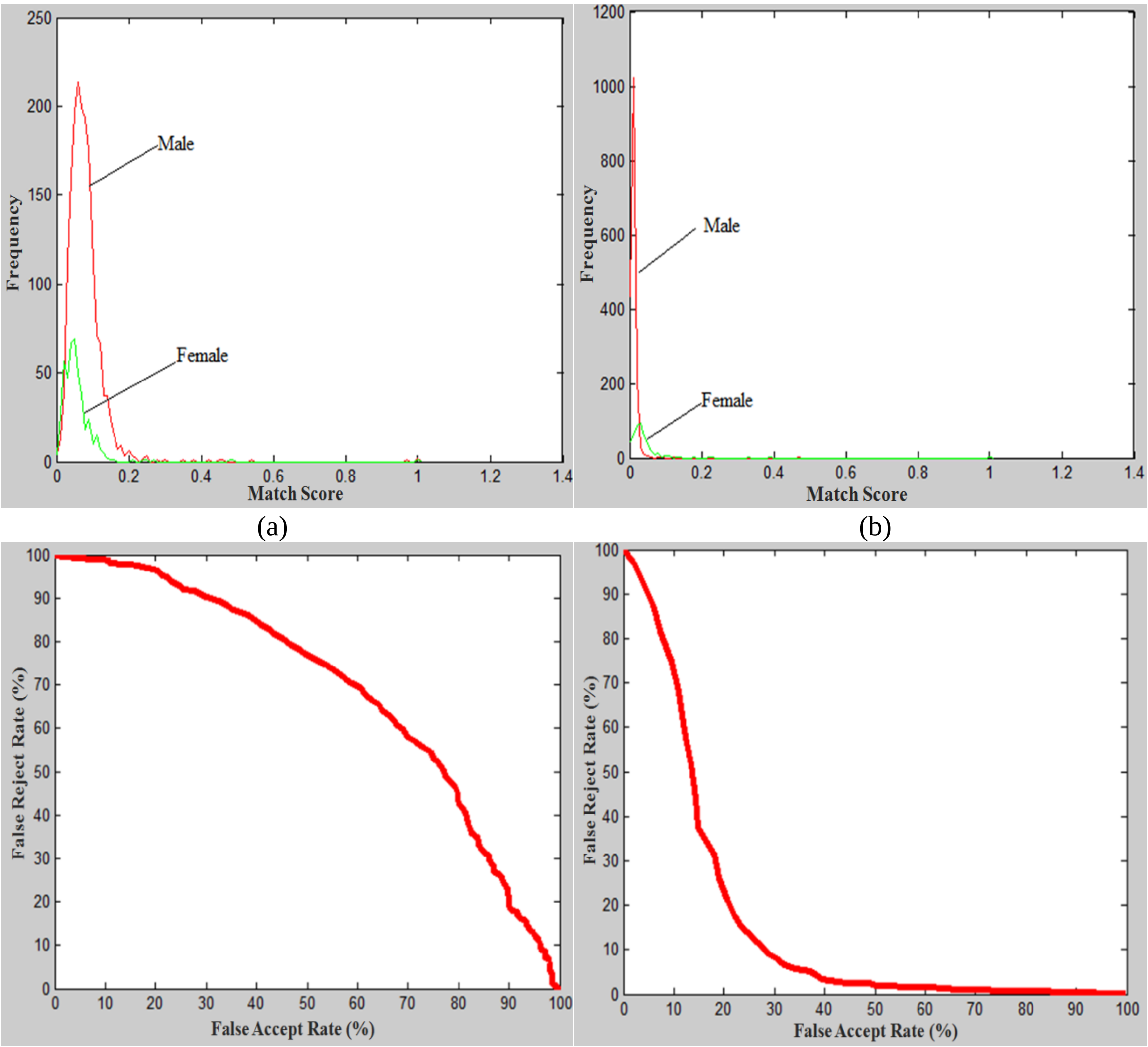

(a) (b)

(c) (d)

Fig. 6.11: Overall Curvature Features for gender classification. (a) Distribution map of horizontal maximum curvature for different gender, (b) Distribution map of vertical maximum curvature for different gender, (c) ROC curve of (a), (d) ROC curve of (b).

6.5 Summary

This chapter further studied the application of 3D fingerprint image reconstructed by the method proposed in the last chapter. Thanks to the availability of 3D fingerprint images, more features can be extracted. Fingerprint features which are coarser than Level 1 features—Curvature Fingerprint Features, are firstly defined in this chapter. These features are then used for assisting fingerprint recognition and gender classification. Experimental results show that an EER of ~15% can be achieved when using 3D curve-skeleton for recognition. The sectional maximum curvatures can be used for human gender classification and with EER of ~19% is obtained in our database. An EER of 3.4% is realized by including Curvature Features into fingerprint recognition which demonstrates the effectiveness of 3D fingerprint recognition. Simple feature extraction and matching algorithm are used in this chapter. We believe that higher accuracy can be achieved if more advanced feature extraction and matching methods are proposed in the future. Discovering the relationship between different levels of fingerprint features and proposing more powerful fusion strategy will further improve 3D fingerprint recognition performance.

Chapter 7
User Authentication Based on Touchless Multi-view Images

Touchless-based fingerprint recognition technology is thought to be an alternative to touch-based systems to solve problems of hygienic, latent fingerprints and maintenance. However, there are few studies about touchless fingerprint recognition systems due to the lack of large database and the intrinsic drawback of low ridge-valley contrast of touchless fingerprint image. This chapter thus proposes an end to end solution for user authentication systems based on touchless fingerprint images in which multi-view strategy is adopted to collect images and robust fingerprint feature of touchless image is extracted for matching with high recognition accuracy. More specifically, some preprocessing steps are firstly acted on original images and briefly described in section 7.2. Distal Interphalangeal Crease (DIP) based feature is then extracted and matched to recognize the human's identity in which part selection is introduced to improve matching efficiency. It is presented in section 7.3. Performance analysis and experimental comparison is given in section 7.4. The experiments are conducted on two sessions of touchless multi-view fingerprint image database with 541 fingers acquired about two weeks apart. Acceptable EER can be achieved by using the proposed DIP-based feature, which is much better than touchless fingerprint recognition by using Scale Invariant Feature Transformation (SIFT) and minutiae features. The given fusion results show that it is effective to combine DIP-based feature, minutiae and SIFT feature for touchless fingerprint recognition systems. We finally conclude the chapter in section 7.5.

7.1 Introduction

Personal identification based on human fingers has been applied for forensics and civilian for decades. It has the largest market shares and brightest perspective among various biometric feature-based recognition systems [1]. Even though there are lots of research achievements and products in fingerprint recognition domain, the performance still cannot reach the expectations of people and theory estimation [9]. Human intervention is necessary when handling low quality fingerprint images. Other new requirements also emerged with the increasing introduction of fingerprint-based techniques into civilian applications, such as user convenience, template security, and hygiene. Furthermore, with the development of computer information security technology, multi-modal biometrics becomes an unstoppable and unchangeable tendency.

Nowadays, rapid advance in fingerprint sensing technology provides solutions to meet the increasing demands of people. Researchers find that the touchless fingerprint imaging technique has decisive advantages of being insensitive to skin deformation (skin elasticity, non-uniform pressure) and skin conditions (dry/wet or dirt), avoiding distortions and inconsistencies due to projecting a 3D finger onto a 2D flat plane image, securing against latent fingerprints, practically maintenance free, being hygienic and robust to fake attacks [34, 82, 83, 104]. Meanwhile, larger fingerprint area and other finger relative information can be easily offered by capturing images at a distance. As shown in Fig. 7.1, the effective area of touch-based fingerprint (left) just corresponds to the portion of the touchless fingerprint (right) enclosed by polygon approximately and finger shape and Distal Interphalangeal Crease (DIP) is offered by touchless imaging.

Thanks to such merits of touchless imaging, researchers and companies begin to design and investigate touchless fingerprint recognition systems although some of them are still in the prototyping phase [33-35, 37, 40, 45, 81-84, 104, 106, 107, 152]. Typically, the group led by Kim in Korea proposed a prototype of touchless fingerprint recognition system using a camera sensor, but just some preprocessing steps were referred to the captured fingerprint images [81]. They also developed a fingerprint enhancement method, resolved the 3D to 2D image mapping problem, and applied the fingerprint verification technology to mobile handsets in their following work [37, 82]. In 2010, they renewed their device to obtain more than one view of the finger at one time to solve finger rolling problem and proposed a mosaicking method using fingerprint minutiae [83]. Hiew et al. [84] designed their own digital camera based touchless fingerprint capturing device and finished an end to end solution fingerprint recognition system by extracting Gabor feature of cropped core point region and using SVM classifier. Kumar et al. [45] captured touchless fingerprint images using webcam and proposed using their defined Level Zero Feature (texture-based feature) to realize low resolution fingerprint recognition. Parziale et al. [35] from TBS Company designed a multi-camera touchless fingerprint capture device (Surround Imager™) and proposed a new representation of fingerprints, namely 3D minutiae, for fingerprint recognition. Jain et al. [33] then proposed an unwrapping algorithm to solve the interoperability issue between rolled images used in AFRS and the touchless fingerprint image captured by the Surround Imager™ in [33]. After that, TBS goes in for improving their device and realizing 3D fingerprint recognition [107]. We also introduced a mosaicking method and compared performance between mosaicked images and flat touch-based fingerprint images in Chapter 4. However, few of such works realized human authentication. Three major reasons may be involved. First, there is lack of public and sufficient touchless fingerprint image database for performance evaluation; this greatly limits the development of touchless fingerprint recognition algorithms. Second, the essential drawback of low ridge-valley contrast makes unprecedented difficulties for classical fingerprint feature extraction; this essential disadvantage can be explained by the imaging method of two devices; in the case of FTIR (Frustrated Total Internal Reflection) imaging, the light that passes through the glass upon valleys is totally reflected but the light that passes through the glass upon ridges is not reflected; in the case of touchless imaging, both ridges and valleys reflect light, and the contrast of ridges and valleys is a result of ridges receiving and reflecting a little more light than valleys; Fig. 7.2 shows an example of a touch-based fingerprint, corresponding its touchless fingerprint, and their pixel value cross sections; this is why usually lower recognition accuracy is obtained when compared touchless-based fingerprint recognition system with touch-based ones. Third, in real fingerprint recognition systems, the performance is degraded by the limitation caused by single-view touchless imaging, such as depth of the field (Dof) of the camera, perspective distortion introduced by camera.

To solve the problems mentioned above, a touchless multi-view fingerprint database with 541 fingers captured by the device presented in Chapter 4 is firstly built for performance evaluation. Then, new fingerprint features which can be robustly extracted from low ridge-valley contrast images are investigated, and the corresponding algorithms for feature extraction and matching are proposed. Also, a view selection strategy is described to reduce computation complexity when multi-view images of one finger are matched. The block diagram of the proposed touchless multi-view fingerprint authentication system is shown in Fig. 7.3. An end to end touchless fingerprint authentication system is finally achieved with an EER of ~1.7%, which is acceptable for practical civilian application.

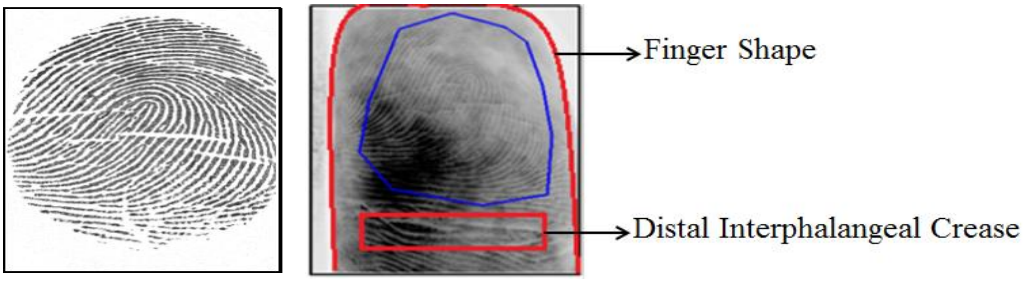

Fig. 7.1: The touch-based fingerprint (left) corresponds to the portion of the touchless fingerprint (right) enclosed by polygon approximately, and extra information provided by touchless fingerprint image (red lines labeled).

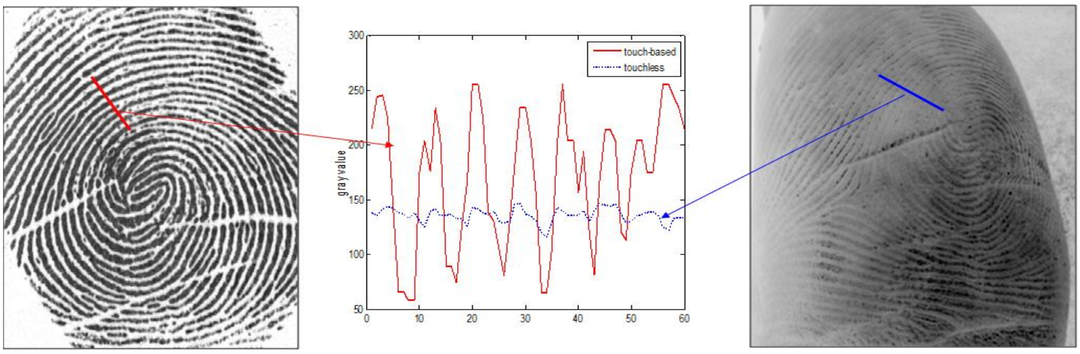

Fig. 7.2: Touch-based fingerprint (left), corresponding touchless fingerprint (right), and their pixel value cross sections (middle).

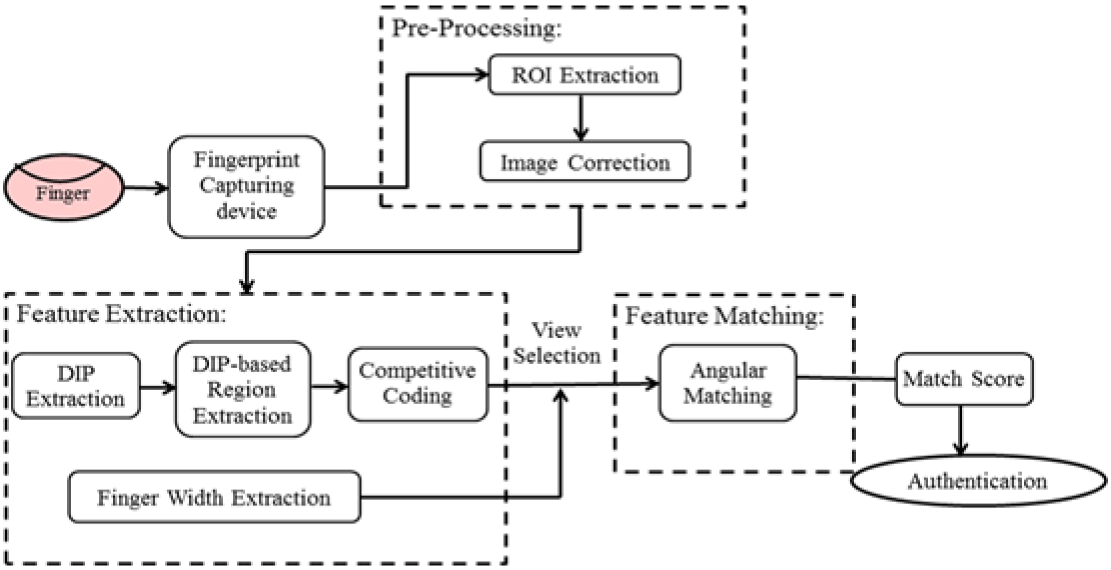

Fig. 7.3: Block diagram of the proposed touchless multi-view fingerprint recognition system.

7.2 Fingerprint Pre-process

Fig. 7.4 shows an example of our captured three channels of fingerprint images. It can be seen that the contrast of ridges and valleys is low, ridge frequency increases from the center part to the side parts, and large fingerprint area with more information is captured.

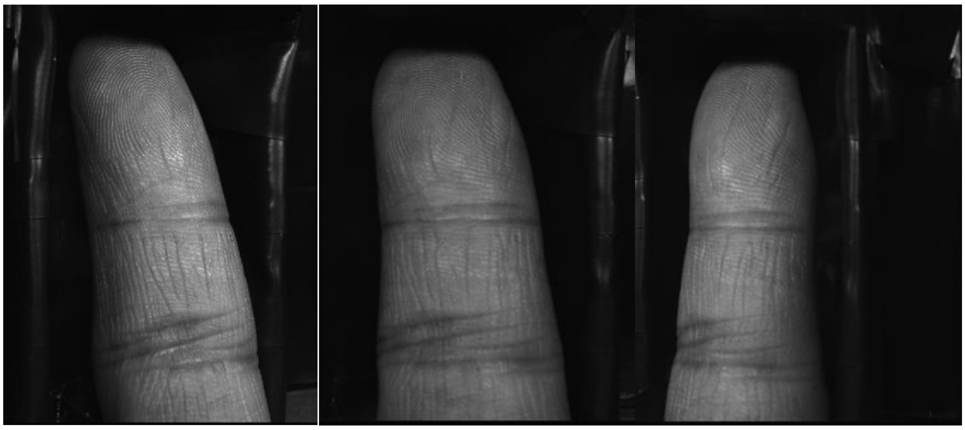

Fig. 7.4: Images of a finger captured by our device (left, frontal, right).

Obviously (see Fig. 7.4), it is necessary to pre-process the original images. First, the foreground should be separated from background, namely ROI extraction. In the ideal situation, simple thresholding segmentation algorithm can easily separate the ROI region from the background due to the full black background of the designed place to put fingers. In the real application, a more robust iterative thresholding segmentation method was adopted to extract ROI. This method had been introduced in Chapter 4 and it is found that this method is effective to the captured images. Fig. 7.5(a) shows the segmentation result of the frontal fingerprint image given in Fig. 7.4.

Since there were tilted fingerprint images caused by volunteers who put their fingers casually in image collection, it was requested to correct the image before feature extraction. The detailed correction steps are introduced in Chapter 6. We then show an example of image correction in Fig. 7.5. The corrected image (Fig. 7.5(c)) is finally obtained by rotating the original image by angle θ anti-clockwise, where θ is the angle between the fit line (blue line in Fig. 7.5(b)) and the vertical axis (red line in Fig. 7.5(b)).

It is noted that whether the ROI is extracted correctly or not has an impact on the image rectification result since the angle is calculated based on the ROI. However, thanks to the full black background of the designed place to put fingers and the robust ROI extraction method, there are few wrongly extracted ROIs on the whole database. Fig. 7.6 gives the histogram of all of the rotation angles obtained by correcting images on the whole database using the proposed method. It can be seen from the result that the angle is usually smaller than 10 degrees. Here, we intensively segmented an image (Fig. 7.7(a)) with bad ROI (see Fig. 7.7(b)) and rectified the image using the proposed correction method. The rotation angle is ~ 7.53° and Fig. 7.7(c) shows the corrected image of Fig. 7.7(a). Fig. 7.7(e) illustrates the corrected result based on good ROI (Fig. 7.7(d)) which was extracted by the method introduced in this chapter. The rotation angle is ~ 5.92°. The difference between them was small and acceptable. This phenomenon reflects that the proposed correction method is robust to the ROI result in a certain degree. It is because that the rotation angle is calculated after fitting the center points by a line (see red line shown in Fig. 7.7(b)), which alleviates the influence of wrongly calculated center points (green points shown in Fig. 7.7(b)) caused by the bad ROI region.

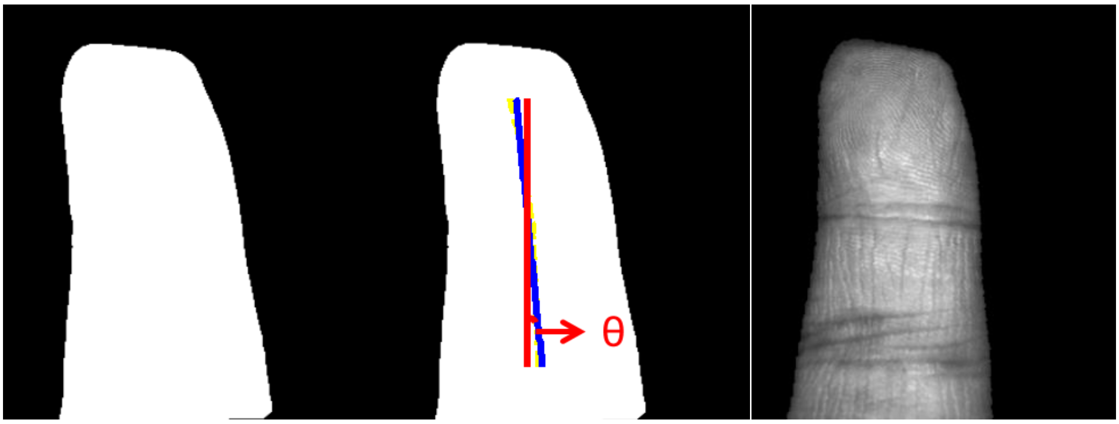

(a) (b) (c)

Fig. 7.5: Pre-processing results of the frontal image given in Fig. 7.4. (a) ROI. (b) Illustration of angle calculation when doing image correction. (c) Corrected fingerprint image.

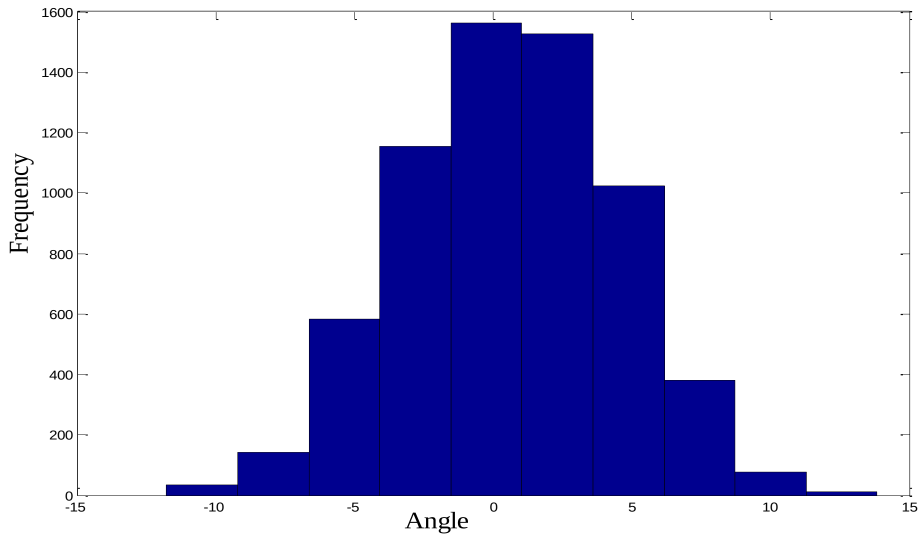

Fig. 7.6: Histogram of all of the rotation angles obtained by correcting images on the whole database using the proposed correction method.

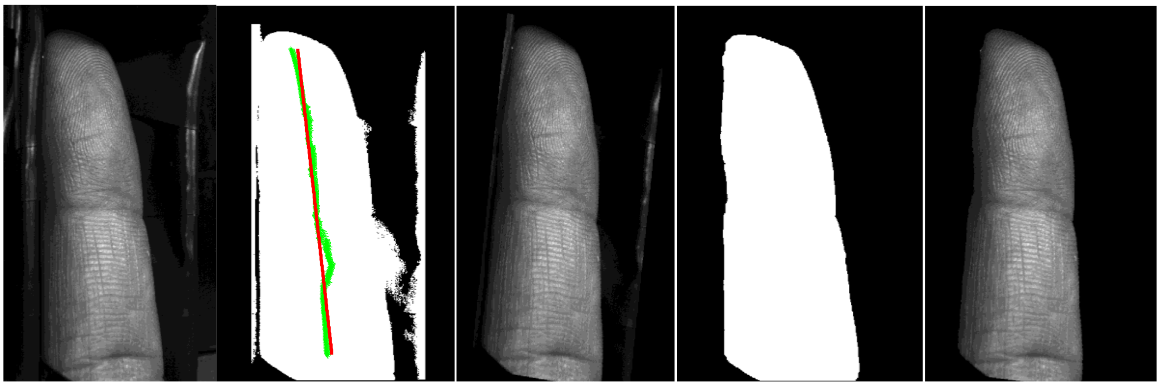

(a) (b) (c) (d) (e)

Fig. 7.7: Example of image correction with bad and good ROI. (a) Original fingerprint image. (b) Intensively extracted bad ROI. (c) Corrected fingerprint image based on (b). (d) Good ROI extracted by the method adopted in this chapter. (e) Corrected fingerprint image based on (d).

7.3 DIP-based Feature Extraction and Matching

7.3.1 Feature Extraction

In general, fingerprint features are divided into three levels [12]. Such three level fingerprint features are categorized by their relationship with fingerprint ridges. For example, Level 1 features are the macro details of fingerprints such as singular points and global ridge patterns. Level 2 features refer to the ridge endings and bifurcations. Level 3 features are defined as the dimensional attributes of the ridges. However, it is difficult to robustly extract features which are closely related to fingerprint ridges from touchless fingerprints due to the intrinsic drawback of low ridge-valley contrast. Thus, in [45], authors labeled four levels of fingerprint features according to the image resolution. They designated level 0 features as fingerprint features which can be observed /extracted from very low resolution images (~50 dpi). Such level 0 features are then extracted and used for human authentication on their established database with very low resolution images. By observing the raw image captured by the device designed by us, we found that the distal interphalangeal crease (DIP) based and finger width features are less relative to fingerprint ridges and can be used for human authentication. It can be concluded that these features can be extracted from very low resolution fingerprint images, and they are studied in this chapter. Here, it should be noticed that the pre-prcosessed image was downsampled before feature extraction to reduce the computational complexity.

DIP [73] is defined as the only permanent flexion crease which is located between medial and distal segments of finger except thumb (between proximal and distal segments), as shown in Fig. 7.8 (cropped by red rectangle). It can be seen that they have two obvious characteristics: I) the principle orientation is almost perpendicular to the fingertip; II) they are dark and thick lines, and similar to the principle line in palm print (see Fig. 7.9). A method is then proposed in this paper to extract the location of DIP and the DIP-based feature based on these two characteristics.

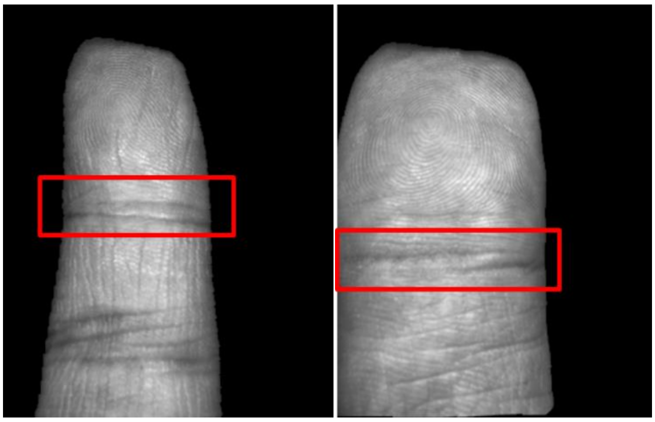

(a) (b)

Fig. 7.8: Example images to show DIP feature (cropped by red rectangle). (a) Index finger. (b) Thumb.

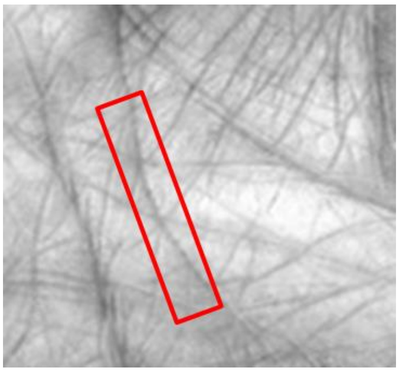

Fig. 7.9: Principle line on palm print (cropped by red rectangle).

Firstly, the orientation field of the pre-processed fingerprint image was calculated using the classical Gradient-based approach introduced in [50], represented by $\{O \mid o_i \in [0^\circ, 180^\circ)\}$ in this paper. In view of character I of DIP, the points whose orientation are close to 0° or 180° predict the existence of DIP. A mask was then generated to forecast the location of DIP by using Eq. 7.1. Angles of 30° and 150° were set by experience in Eq. 7.1. Fig. 7.10 gives an example of the mask of Fig. 7.5(c).

$$M = \begin{cases} 1 & o_i \le 30^\circ \mid o_i \ge 150^\circ \\ 0 & otherwise \end{cases} \tag{7.1}$$

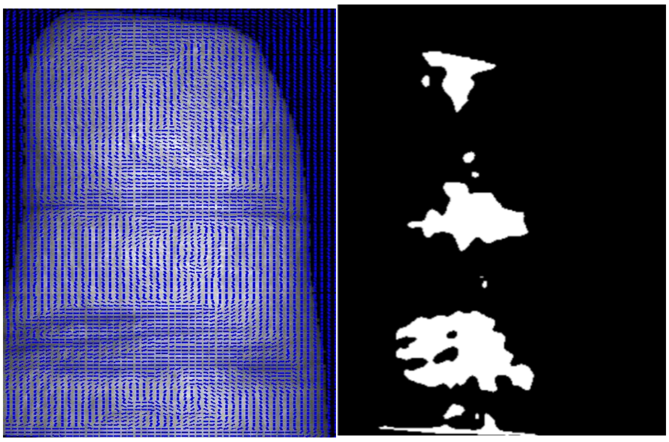

(a) (b)

Fig. 7.10: Orentation map and generated mask M of Fig. 6(c). (a) Orientation map. (b) M .

Secondly, the intensity image (I_M , see Fig. 7.11(a)) which predicts the location of DIP on the original image was obtained by using M . Here, the regions of M with zero intensity values were set to 255 (maximal gray-level value, white region in Fig. 7.11(a)) when I_M was generated. Because of character II of DIP, we projected the intensity of pixels of I_M in row, represented by L_1 (see Fig. 7.11(b)). It can be seen that the location of DIP lies in the local minimum of the projection line.

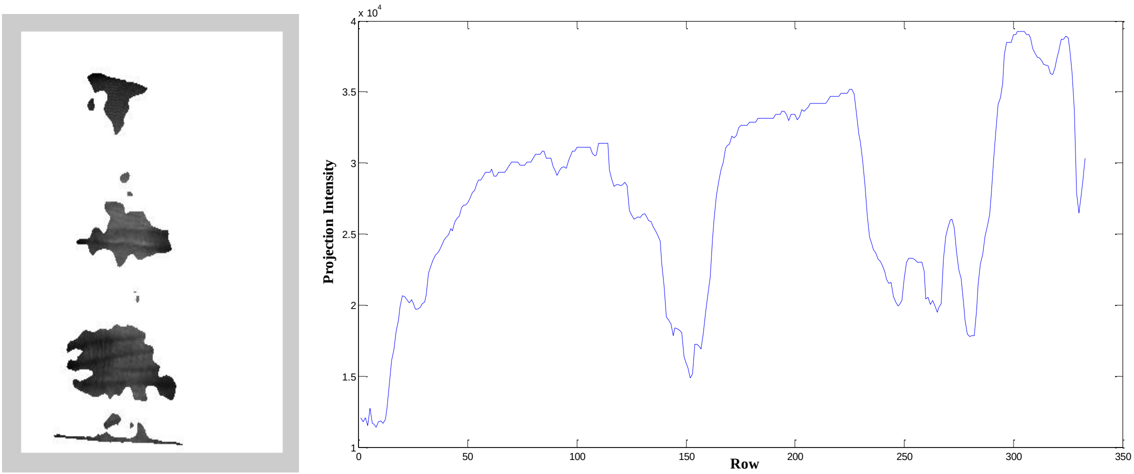

(a) (b)

Fig. 7.11: The intensity region which predicts DIP I_M and its corresponding projection line L_1. (a) I_M . (b) L_1 .

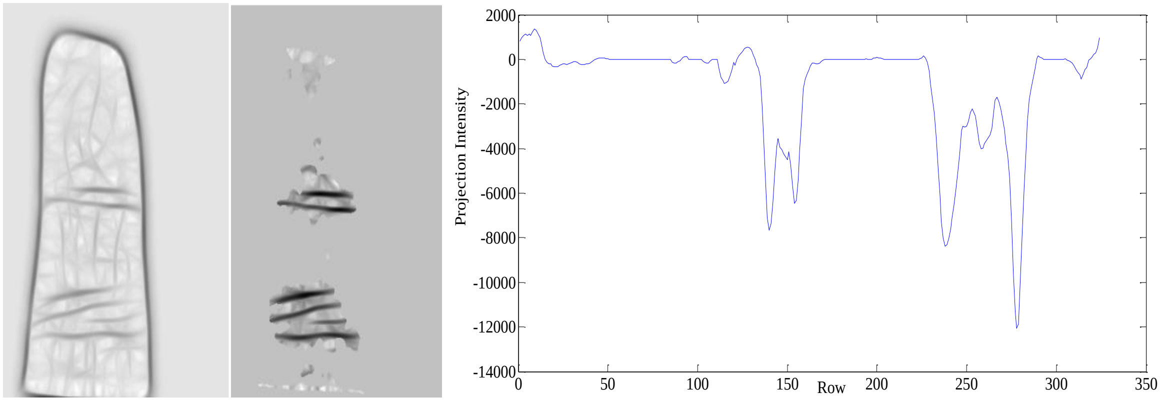

(a) (b) (c)

Fig. 7.12: Results applied to Fig. 7.5(c) based on the similarity to the principle line in palm print. (a) Maximum response map *R*. (b) Region mask R_M. (c) Projection line L_2.

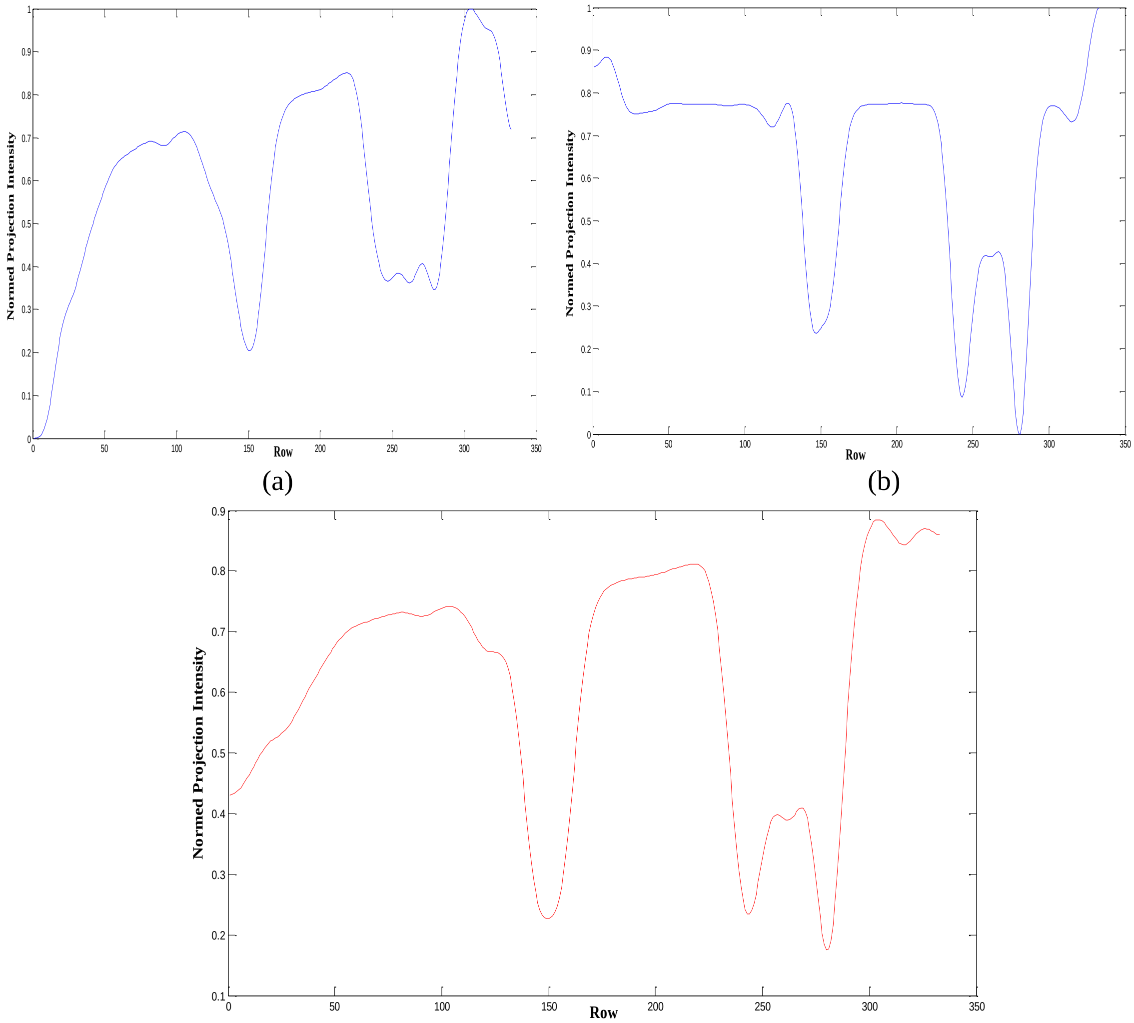

(a) (b)

(c)

Fig. 7.13: Projection lines after processing. (a) Smoothed projection line of L_1. (b) Smoothed projection line of L_2. (c) Final combined projection line L.

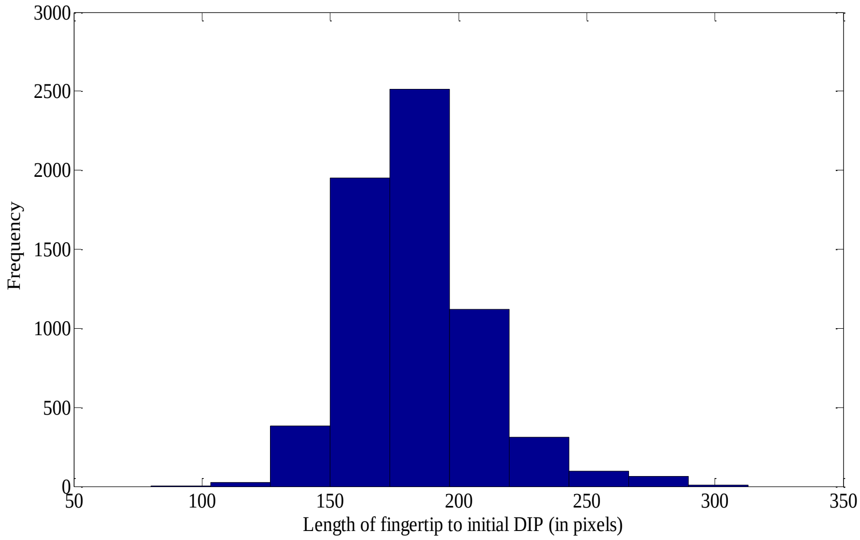

Fig. 7.14: Histogram of length of fingertip to initial DIP on our database.

Thirdly, since DIP is similar to the principle line in palm print mentioned in character II of DIP, we applied a set of Gabor filters introduced in [153] to the pre-processed image to form a set of response maps. Here, the frequency of the Gabor filters was set to $\frac{1}{3.45}$ and the range of orientation was $\left[0^{\circ}:15^{\circ}:180^{\circ}\right)$. After that, a maximum response map R (see Fig. 7.12(a)) was obtained by extracting the maximum response of each pixel from the set of response maps. The corresponding region where DIP exists can be extracted by M, marked as R_M (see Fig. 7.12(b)). The local minima will be formed if the intensity of pixels of R_M was projected in row, as the projection line L_2 shown in Fig. 7.12(c). It is obvious that the local minima of the projection line indicate the possible location of DIP.

After the extraction of two projection lines, L_1 and L_2, a 1-Dementional Gaussian filter with length of five was adopted to smooth them and normed their values to [0, 1], as shown in Fig. 7.13(a) and Fig. 7.13(b). Finally, they were combined into one line by simple averaging strategy (see Fig. 7.13(c)).

Since there were several local minima ($\{V_i \mid i = p_1, p_2, \cdots, p_N\}$, where p represents the position of local minimum) in the projection line L, criteria should be made to pick up the closest one. It is prior knowledge that the positions of DIP for the same finger type are similar. The lengths from the fingertip to the DIP of five finger types were estimated and taken as a threshold (T) to indicate the location of DIP by Eq. 7.2. The threshold T was determined after two steps. Step one: we manually measured the lengths from the fingertip to the DIP of five finger types of several persons and converted the lengths into image pixels by Eq. 7.3, where r denotes image resolution, h is the height of the image, and H represents the measured length (in millimeters). The measured value (h) was taken as a coarse threshold to compute the location of the DIP by using Eq. 7.2. Step two: we statistically computed the lengths from the fingertip to the initial DIP of each finger on the whole database. The refined threshold was obtained by analyzing the histogram of the calculated lengths from the fingertip to the initial DIP (shown in Fig. 7.14). It was set to 180 in the chapter. The location of the DIP was finally defined by considering both of the local minima of the projection line and the priori lengths, as illustrated in Eq. 7.2.

$$P_{DIP} = \min_{p}\left\{abs\left(p - T\right)\right\} \tag{7.2}$$

$$H = 25.4 \times h / r \tag{7.3}$$

Finally, the location of DIP was taken as the base line, and a region of size 101*288 pixels centered at the base line was cropped. DIP-based feature was finally formed by coding the region using competitive coding scheme introduced in [153], as shown in Fig. 7.15. Such feature was extracted in this study since the DIP lines are similar to the palm lines. Orientation information of DIP lines was extracted by competitive coding scheme using multiple 2D Gabor filters. The filters and parameters were the same as those which were used to extract the projection line L_2.

Additionally, since the finger shape was fully imaged by the device, the finger width feature could be extracted by counting the non-zero values of the pre-processed image row by row. We designated the counts from the fingertip to the location of DIP as the finger width feature, as illustrated in Fig. 7.16.

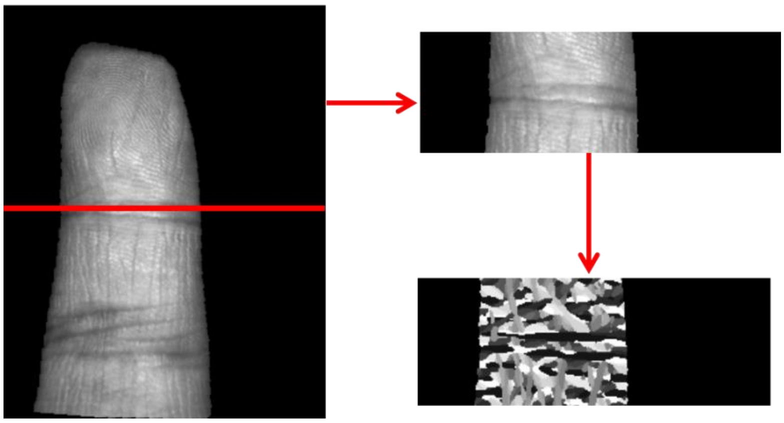

Fig. 7.15: Illustration of extraction of DIP-based feature.

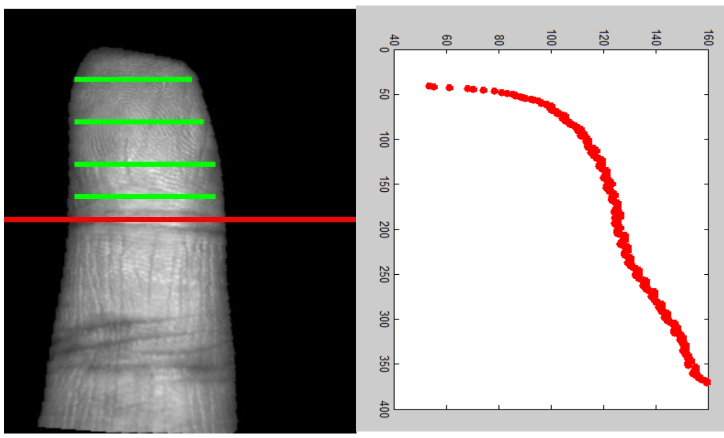

(a) (b)

Fig. 7.16: Illustration of finger width extraction. (a) Finger width refered in the chapter (green lines labeled). (b) Final extracted finger width feature.

7.3.2 View Selection

There are three views of fingerprint images (left-side, frontal, and right-side) for each finger. So nine times of matching are needed to identify one finger to find out the best matching. It is time consuming. This chapter thus proposed a view selection strategy before matching to reduce the complexity but keep the accuracy. Since the finger width feature can be easily extracted from each view of images, the mean values of finger width of each view were calculated and compared between views of gallery and probe images. Those pairs whose difference was smaller than a threshold were finally selected. Eq. 7.4 gives the criterion of the proposed view selection strategy, where W_G and W_P represents the mean value of finger width for gallery and probe images separately. In the end, the number for matching (9 times in total) could be reduced to about 3 to 5 times after this view selection.

$$\left\{(i,j)=\arg_{i,j}\left(abs\left(W_{Gi}-W_{Pj}\right)<30\right) \mid i,j=1,2,3\right\},\quad \begin{cases}1: left\_side\\ 2: frontal\\ 3: right\_side\end{cases} \tag{7.4}$$

7.3.3 Feature Matching

Since the competitive code based on DIP was taken as the DIP-based feature, angular matching method [153, 154] was adopted. This method was proposed to compare orientation information stored in competitive code effectively and efficiently. It calculated the angular distance by bit operation. In this study, there were 12 directions (labeled as integer: 0, 1, 2, … , 11) used when DIP-based feature was computed. Four bits can fully represent each element. However, to realize bit operation, six bits should be used since maximum angular distance will be six when 12 directions are used.

Table 7.1 shows the bit representation of competitive code in this chapter. The DIP-based feature was finally represented by seven bits since the adding of one bit to label mask. The angular distance is then defined as Eq. 7.5, where G_{mask} and P_{mask} represent the masks of DIP-based feature G and P in gallery and probe images, G_i^b (or P_i^b) denotes the i^{th} bit plane of G (or P), $\cap$

is an AND operator and $\otimes$ is bitwise exclusive OR, and $M \times N$ is the size of feature matrixes. The calculated angular distance was used as the match scores in this chapter. Since there were several view pairs between a registered finger and an input finger, the best match score, namely the minimum one, among match scores of all view pairs was chosen as the final match score to do the authentication.

Table 7.1: Bit representation of competitive code.

Elements representing competitive code	Bit 1	Bit 2	Bit 3	Bit 4	Bit 5	Bit 6
0	0	0	0	0	0	0
1	0	0	0	0	0	1
2	0	0	0	0	1	1
3	0	0	0	1	1	1
4	0	0	1	1	1	1
5	0	1	1	1	1	1
6	1	1	1	1	1	1
7	1	1	1	1	1	0
8	1	1	1	1	0	0
9	1	1	1	0	0	0
10	1	1	0	0	0	0
11	1	0	0	0	0	0

$$D(G,P)=\frac{\sum_{y=0}^{M-1}\sum_{x=0}^{N-1}\sum_{0}^{6}\left(G_{mask}(x,y)\cap P_{mask}(x,y)\right)\cap\left(G_i^b(x,y)\otimes P_i^b(x,y)\right)}{6\sum_{y=0}^{M-1}\sum_{x=0}^{N-1}G_{mask}(x,y)\cap P_{mask}(x,y)} \tag{7.5}$$

7.4 Experimental Results and Performance Analysis

7.4.1 Database and Remarks

The database was established by using the touchless multi-view fingerprint imaging device introduced in Chapter 4. It contained 541 fingers from both male and female, aged 22 to 45. Five kinds of fingers were all included. There were two samples collected in each of two sessions separated by a time period of about two weeks. Each sample consisted of three views of fingerprint images with size of 576 pixels by 768 pixels and at a resolution of about 400dpi. The following matches and experiments were conducted on the database. 1) Genuine matches: Fingerprint images of the same finger were matched with each other, resulting in 3,246 genuine match scores. 2) Imposter matches: the first fingerprint image of each finger in the first session was matched with the first fingerprint images of all the other fingers but with the same finger type in the second session, resulting in 15,010 imposter match scores. Based on the obtained match scores, the equal error rates (EER) and the receiver operating characteristic (ROC) curves were calculated for performance evaluation.

Since minutiae are the classical fingerprint features used in touch-based AFRSs, and Scale Invariant Feature Transformation (SIFT) [116] is one of the frequently used non-minutia features used for fingerprint recognition with poor image quality. Both were adopted for authentication to compare their recognition performance with the proposed DIP-based feature on the established database. The methods introduced in [111] and Chapter 4 of this thesis were employed to extract and match these two features respectively in this chapter. There are lots of minutiae-based fingerprint matching algorithms [18, 50, 83, 111, 156-161]. The one proposed in [111] was used in this study for the reason that it ranks 1st on DB3, the most difficult database in FVC2002 and outperforms the best two algorithms PA15 and PA 27 on four databases in FVC2002. The minutiae match score between two fingerprints was defined as the percentage of the matched minutiae among the complete set of minutiae on the two fingerprints, and the SIFT match score between two fingerprints was defined as the number of matched SIFT points.

Fusion was implemented in score level. Score normalization was firstly applied so as to make the match scores of different matchers transform into a common domain [155]. The min-max (MMN) technique [155] was considered in the experiment. After normalization, min (MIN), max (MAX), simple sum (SSUM) and weighted sum (WSUM) rules were used to combine the match scores of individual matchers into a single final score for the input fingerprint. Obviously, the MIN and MAX rules respectively select the minimum and maximum of the match scores of all individual matchers as the final score, whereas the SSUM rule takes the summation of the match scores as the final score [155]. The WSUM rule tests different weights from 0 to 1 with an interval as 0.1 to find the best weight to form the final score [71].

7.4.2 Recognition Performance using DIP-based Feature

To evaluate the performance of the proposed method using DIP-based feature, the genuine and imposter match score distribution map and the ROC curve were both given, as shown in Fig. 7.17. The EER was also calculated. It can be seen that the match scores range from 0 to 0.4614. Match scores for genuine pairs are between 0.1 and 0.3, while match scores for imposter pairs are concentrated on ~0.41. It can well separate genuine and imposter pairs. An EER of ~1.7% was obtained when the DIP-based feature is used for recognition, which shows the effectiveness of user authentication using the DIP-based feature for multi-view touchless fingerprint images.

7.4.3 Effectiveness Validation of the Proposed View Selection Scheme

Since there are three views of fingerprint images captured at one time for one finger, recognition results will be different if different view pairs are used or diverse fusion strategies are adopted. This study took the DIP-based feature matching as an example to validate the effectiveness of the proposed view selection scheme. Fig. 7.18 shows the ROC curves by matching single view fingerprint images, the ROC curve by matching multi-view fingerprint images after view selection, as well as the ROC curves based on four kinds of fusion strategies using DIP-based feature. From the results, it can be seen that the matching result after our view selection outperforms the results of both of single view matching and matching using simple fusion strategies (all of four kinds fusion mentioned). This is because the best matching candidates were selected from the overall nine times of matching after the view selection process but single view matching and single view fusion could not guarantee the best matching, as the example shown in Fig. 7.19. The best matching score existed between $\left(Probe_R, Gallery_F\right)$ (red labeled in Fig. 7.19, 0.2641), which was not included in single view pairs (blue labeled in Fig. 7.19) but in the view candidates after the view selection process. Thus, the best matching score (0.2641) could be obtained by minimizing results after the view selection process, whereas better but not the best matching score (0.2812) was obtained after score-level fusion using MIN rule.

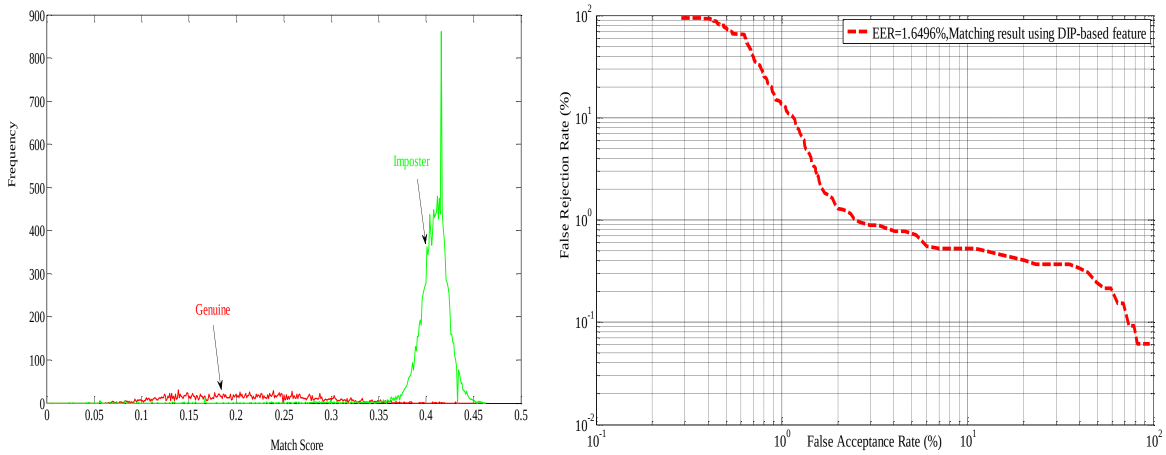

(a) (b)

Fig. 7.17: Verification results using DIP-based feature. (a) Genuine and imposter distributions. (b) The ROC curve using DIP-based feature.

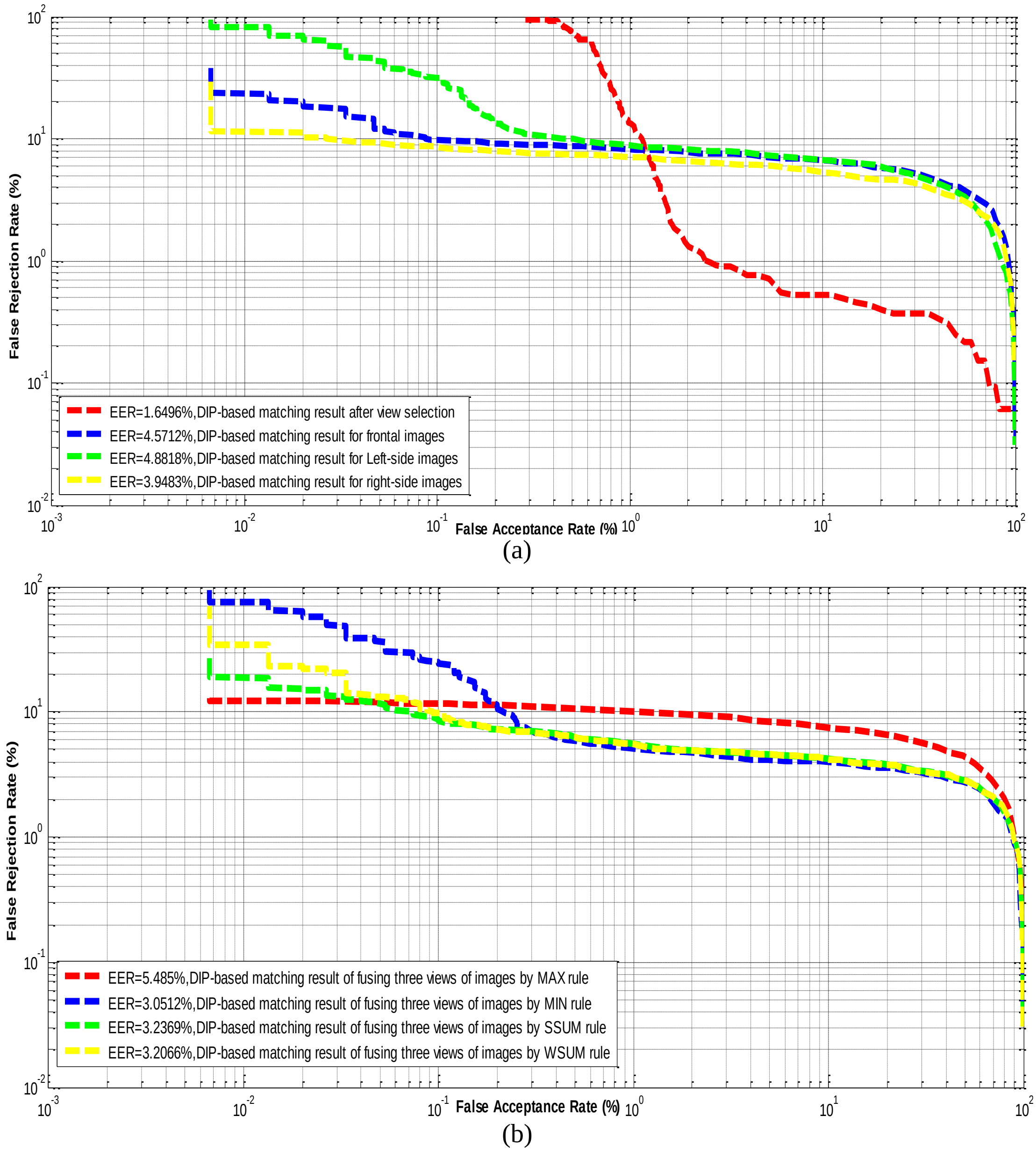

Fig. 7.18: The ROC curves based on different view fingerprint images and various fusion strategies. (a) The ROC curves of single view fingerprint images compared with ROC curve of multi view fingerprint images after view selection. (b) The ROC curves based on four kinds of fusion strategies.

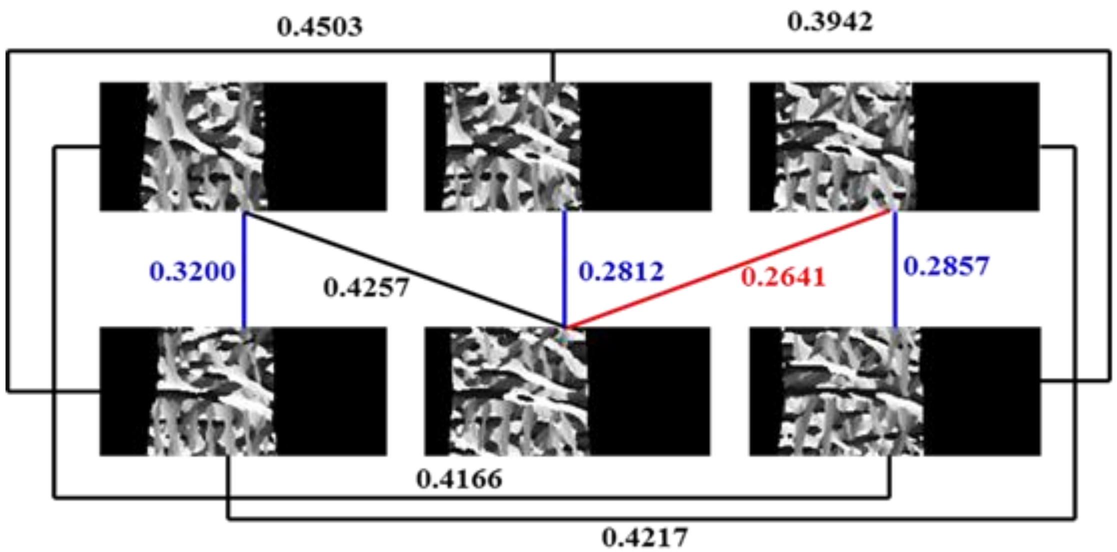

Fig. 7.19: Scores of matching DIP-based feature extracted from Gallery images (left-side, frontal, right-side) and Probe images (left-side, frontal, right-side).

7.4.4 Comparison of Recognition Performance Based on Different Fingerprint Features

As we mentioned in section 7.4.1, minutiae and SIFT features were both considered for human authentication and implemented on the database to investigate their performance for touchless fingerprint images. Firstly, examples of matching results using DIP-based feature, minutiae, and SIFT feature for one genuine pair and one imposter pair are shown in Fig. 7.20. It can be found that there were a few of matched pairs for minutiae matching (7 for genuine pair and 0 for imposter pair). There were 315 matched SIFT feature points for genuine fingerprint image pair while 7 couples for imposter pair. The angular distances of DIP-based feature matching were 0.214 and 0.417 for genuine and imposter pairs, respectively. The ROC curves and EERs were also given, as shown in Fig. 7.21. The best EER of minutiae-based matching was ~10%, while the best EER of SIFT feature-based matching was ~3%. Both EERs were larger than the best one obtained by matching DIP-based feature (see Fig. 7.18(a)). It can be concluded that the proposed

DIP-based feature is more effective than both minutiae and SIFT feature when touchless multi-view fingerprint images are matched. Generally, non-minutia features which are less sensitive to the clarity of ridges will be more suitable for touchless fingerprint recognition when only one feature is used for authentication.

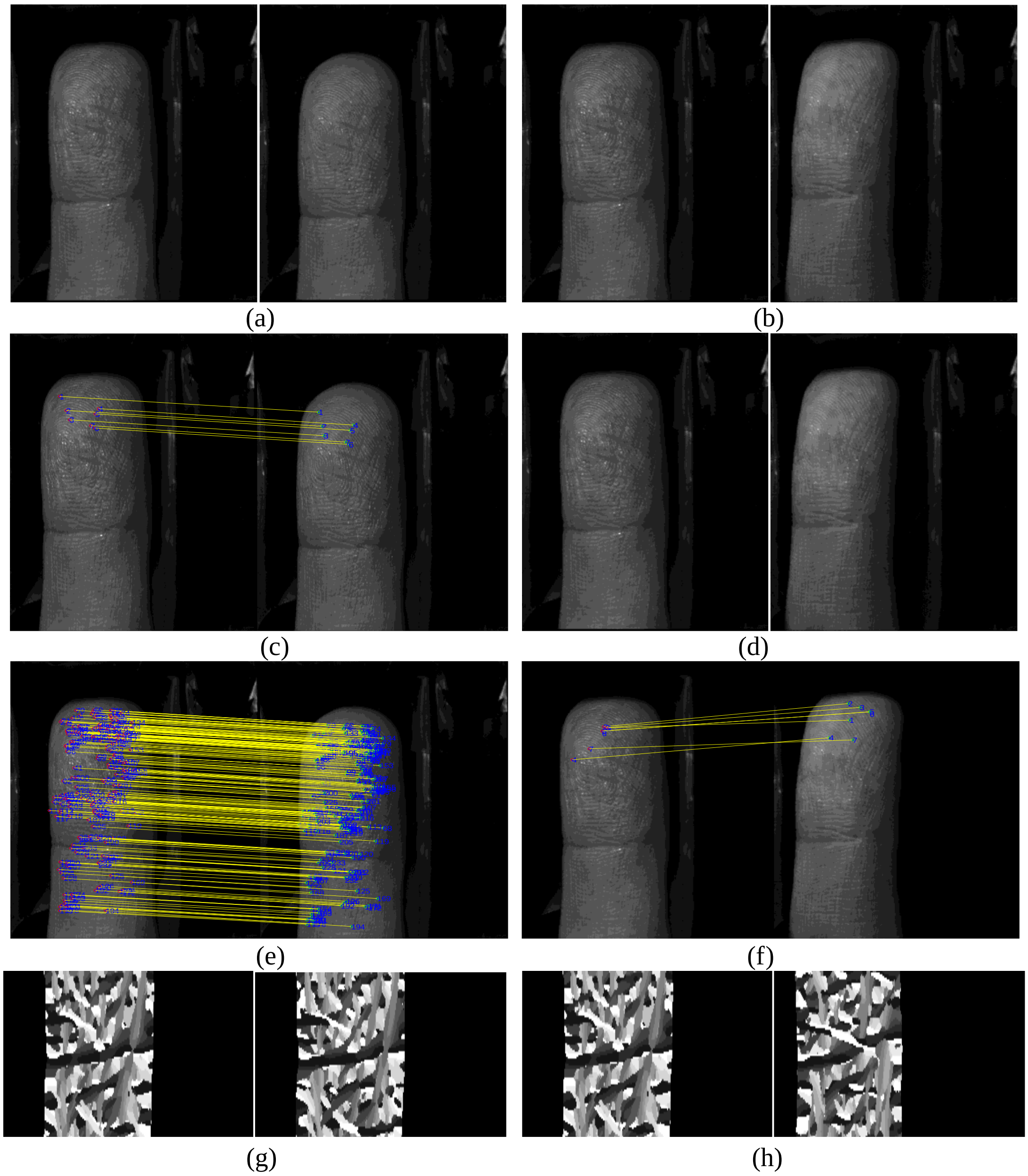

Fig. 7.20: Example matching results by minutiae, SIFT and DIP-based features for a genuine fingerprint image pair and an imposter pair. (a) Original genuine fingerprint image pair (right ring finger). (b) Original imposter fingerprint image pair (right ring finger vs. left ring finger of the same person). (c) Minutiae matching result of (a). (d) Minutiae matching result of (b). (e) SIFT feature matching result of (a). (f) SIFT feature matching result of (b). (g) DIP-based feature comparison of (a) (angular distance is 0.214). (h) DIP-based feature comparison of (a) (angular distance is 0.417).

Fig. 7.22 provides the ROC curves and EERs of the fusion results in match score level. It can be seen that performance improved after fusion. DIP-based feature plays an important role in improving recognition accuracy. As low as an EER of ~0.5% was achieved if all of these three features were fused.

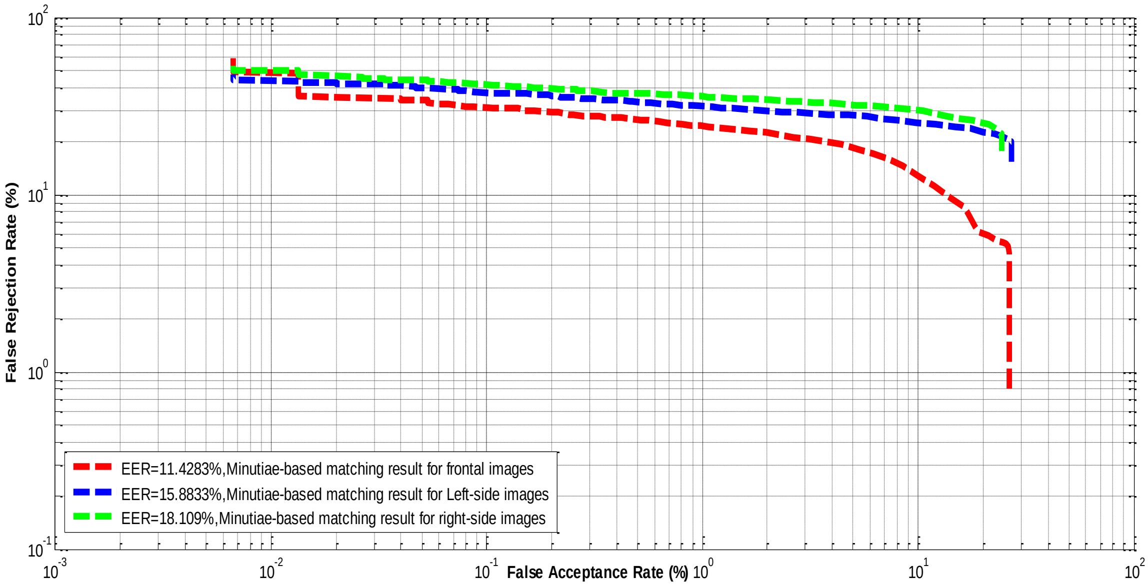

(a)

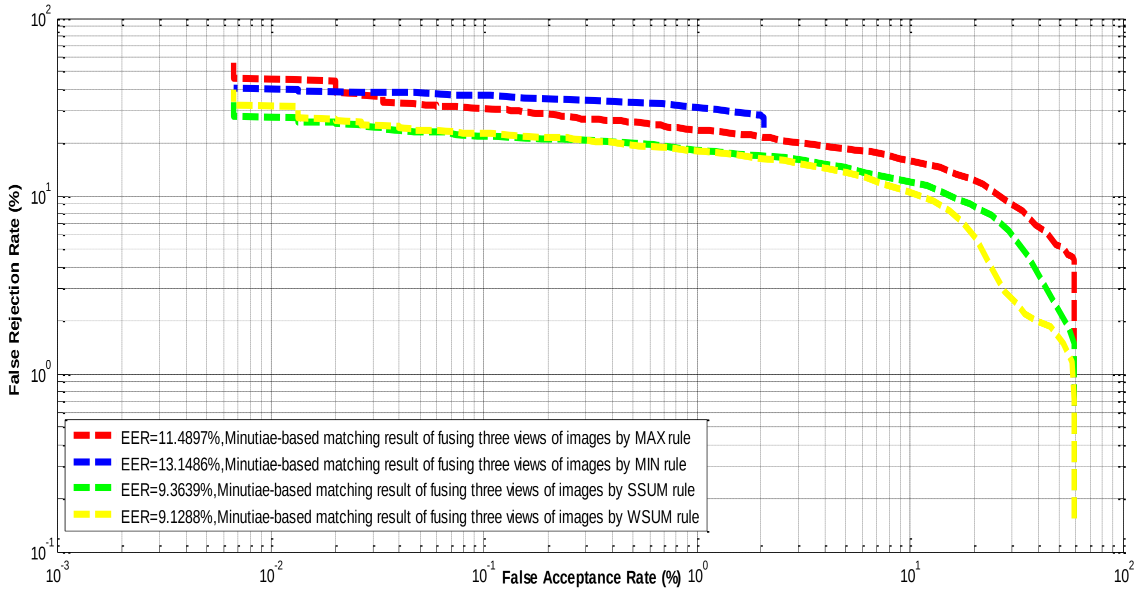

(b)

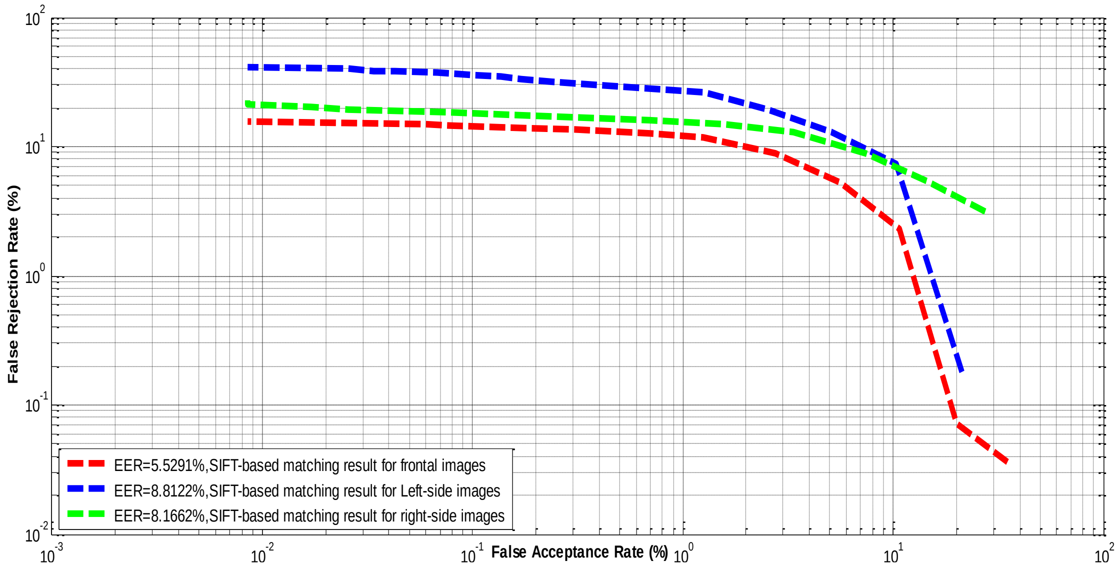

(c)

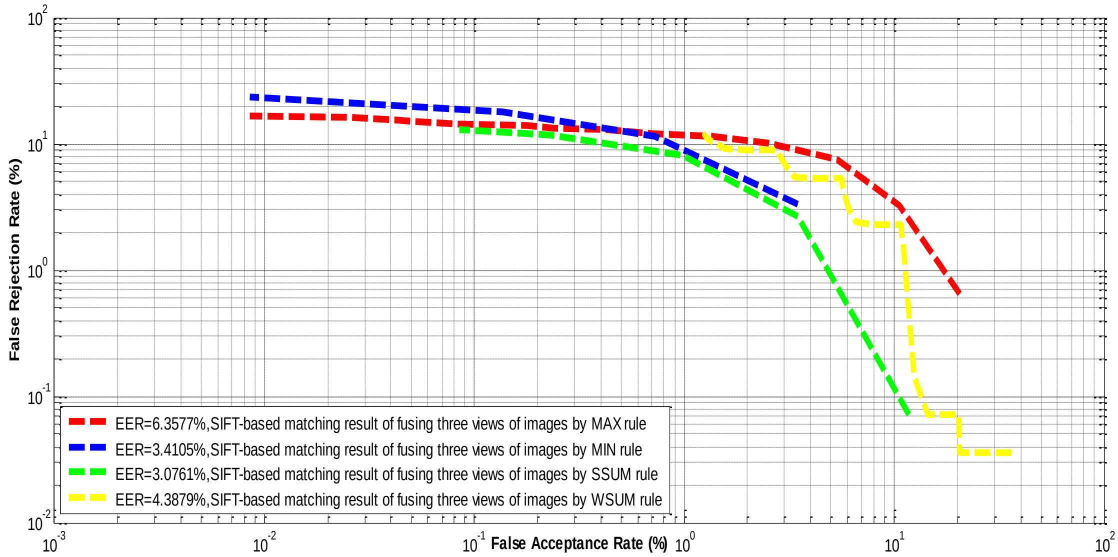

(d)

Fig. 7.21: The ROC curves based on different features on situation of both using single view images and adopting fusion strategies. (a) The ROC curves on situation of single view fingerprint images when only minutiae are used. (b) The ROC curves based on four kinds of fusion strategies when only minutiae are used. (c) The ROC curves on situation of single view fingerprint images when only SIFT feature is used. (d) The ROC curves based on four kinds of fusion strategies when only SIFT feature is used.

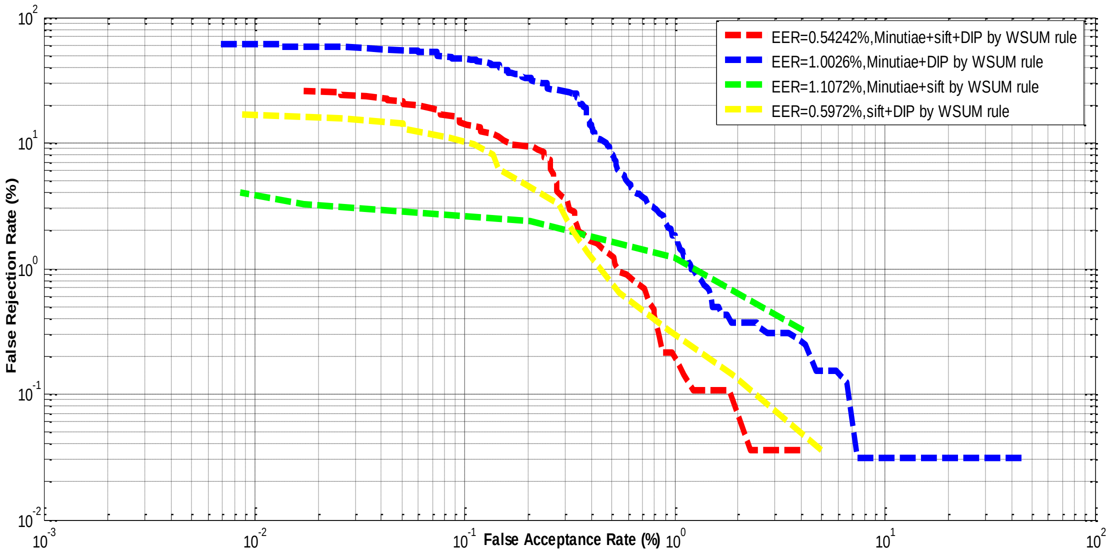

Fig. 7.22: The ROC curves of different feature fusion.

7.5 Conclusion

This study provided an end to end user authentication system using DIP-based feature for touchless fingerprint images. Multi-view strategy was used in the capturing device to alleviate system performance degradation caused by single-view imaging. DIP-based feature, which could be robustly extracted from low ridge-valley contrast touchless fingerprint images, were presented and used for authentication. The corresponding algorithms for feature extraction and matching were also introduced in this chapter. View selection scheme was adopted before matching to reduce computation complexity when multi-view images for one finger are matched. Experiments were implemented on the touchless multi-view fingerprint image database established by us with 541 fingers acquired in two sessions with an interval of about two weeks (each 2 samples). Classical and frequently-used fingerprint features (e.g. minutiae and SIFT feature) as well as the new proposed DIP-based feature were used and evaluated on the established database. It can be found: i) DIP-based fingerprint recognition outperforms other compared features when only one feature used; ii) the view selection strategy is more effective than other common used fusion strategies; iii) it is hard to obtain high recognition accuracy by traditional minutiae-based systems for touchless fingerprint images (The EER was around 10%). However, it is effective to combine non-minutia features and minutiae features for touchless fingerprint recognition systems (best EER of ~0.5% was achieved). The experimental results presented in this chapter are promising. We believe that the performance of touchless fingerprint recognition system will be further improved since the fact that the area of touchless fingerprints is generally larger than that of touch-based fingerprints, which enables us to extract more distinctive information from touchless fingerprints than from touch-based fingerprints. There are also broad prospects to propose effective minutiae extraction and matching methods specific to touchless fingerprint images since minutiae are the most widely used feature in current AFRSs.

Chapter 8

Summary and Future Research

8.1 Research Contributions

With the advent of advanced imaging techniques and people's increasing demands, novel types of AFRSs are raised. It thus brings about new issues for fingerprint-based user authentication systems. This thesis tried to solve the emerging problems specific to two types of new raised AFRSs, one is high resolution AFRS and the other one is touchless 3D AFRS. The emphasis of our research focus on touchless 3D AFRS since some work about high resolution AFRS had been done by our group. The details of our research contributions are listed as follows.

1. <u>Provide a way to build a standard resolution for high resolution AFRS.</u> Since resolution is one of the main parameters affects the captured fingerprint image quality and issues such as cost, interoperability, and performance of an AFRS, it is of great importance to offer a standard resolution for AFRSs. We, for the first time, provided a way to recommend a reference resolution. The procedure of our method is: Firstly, we established a multi-resolution fingerprint database from 500dpi to 2,000dpi for resolution selection. Then, three criteria based on two most representative fingerprint features, minutiae and pores, are set. The reference resolution for high resolution AFRS is finally recommended by theoretical and recognition performance analysis using these three criteria.
2. <u>Propose a fingerprint pore matching method with high recognition accuracy.</u> This approach matches pores in a hierarchical way. Specific to the noise and distortions of captured fingerprints and the inaccurate of extracted features, a more robust coarse matching method was put forward. Next, a WRANSAC algorithm was used to refine the coarse matching result. By following this coarse-to-fine strategy, higher recognition accuracy was achieved when compared with the existing pore matching methods.

3. Build a new touchless multi-view fingerprint acquisition device. The device was designed by optimizing parameters regarding the captured fingerprint image quality and device size. The optimization design of the device was demonstrated by introducing our design procedure and comparing with current touchless multi-view fingerprint acquisition devices. The efficiency of the device was further proved by comparing recognition accuracy between mosaicked images obtained by our proposed method and touch-based fingerprint images.
4. Put forward a 3D reconstruction method based on touchless multi-view fingerprint images. For the reason that 3D fingerprint reconstruction technique offers a solution for 3D fingerprint image generation and application when only multi-view 2D images are available, we studied the technique about 3D fingerprint reconstruction. It is very difficult for 3D fingerprint reconstruction due to the poor quality of touchless fingerprint images and the impossible of establishing pixel to pixel correspondences between two different views of 2D fingerprint images. We thus improved the methods for feature extraction from touchless fingerprint images and proposed to estimate finger shape model instead of establishing pixel to pixel correspondences. 3D fingerprint reconstruction results from different fingerprint feature correspondences were then given. Best result was finally selected out to establish our 3D fingerprint image database by analyzing the reconstruction accuracy.
5. For the first time study 3D fingerprint features and their applications for personal authentication. Due to the unavailable of public 3D fingerprint database, there are few studies about 3D fingerprint recognition. We for the first time defined 3D fingerprint features including curve-skeleton and overall maximum curvatures, which are coarser than level 1 fingerprint features, and then investigated their distinctiveness for user authentication. These features are found to be useful to assist fingerprint matching and make contribution to fingerprint recognition by combining with 2D fingerprint features.
6. Raise an end to end solution for touchless multi-view fingerprint recognition. Since more information can be captured by touchless imaging, we proposed an end to end user authentication system based on touchless multi-view fingerprint images. In this system, new features --Distal Interphalangeal Crease (DIP) based feature was proposed, extracted and

matched by our designed algorithms. Experimental results show that higher recognition accuracy can be obtained based on the DIP-based feature compared with SIFT and minutiae features. Promising EER is achieved by combining DIP-based feature with other features for touchless fingerprint recognition systems.

8.2 Future Directions

Even though some progresses have been made on this thesis to develop AFRSs with high performance, the results still need to be further improved to meet people's needs. We suggest the following directions to extend our research studies.

1. Set standard resolution for all of the AFRSs. In our research, we set a reference resolution under the condition of fixed image size. However, different image sizes are used for different AFRSs. Trade-off should be made between the influences of resolution and image size within a certain range on AFRS. It is necessary to figure out their relationship so as to establish standard resolution for AFRSs.
2. Reduce computational complexity for pore matching. Even though high recognition accuracy can be achieved by the proposed pore matching method, the computational complexity is also very high due to the abundant amount of pore number. This high computational complexity limits the application of the proposed method. How to further improve the efficiency of the proposed pore matching method is in our future work. One possible solution is first aligning two fingerprints to estimate the overlapping area between them and then matching only the pores lying in the overlapping area.
3. Propose robust feature extraction and matching method specific to touchless fingerprint images. Touchless fingerprint images have the characteristics of low ridge-valley contrast and large variations of ridge frequency. Such features make huge difficulties for ridge relevant features (e.g. minutiae) extraction. The current feature extraction methods are almost specific to touch-based fingerprint images which have quite different image quality compared with touchless ones. Thus, new feature extraction approaches which are robust to the drawbacks of touchless fingerprint images should be very important to extend the application of touchless

fingerprint recognition systems. Meanwhile, distortions relevant with touchless imaging are also different with touch-based ones. Proposing effective feature matching methods specific to touchless fingerprint images are also very necessary to broad the utility of touchless fingerprint recognition systems.

4. Make full use of the rich information on touchless fingerprint images. Since the area captured by touchless fingerprint imaging is generally larger than the touch-based one, there is more information provided (e.g. large minutiae number, finger shape feature, finger crease feature and 3D information etc.). We believe the recognition accuracy will be improved by make full use of these features.

5. Investigate and take full advantage of 3D fingerprint images. Currently, researchers found 3D fingerprint images provide more attributes for fingerprint features than 2D fingerprint images. For instance, a minutia feature in 2D fingerprint image is usually represented by its location and orientation. While in 3D case, one additional spatial coordinates and orientation are available. Thus, fingerprint recognition with higher security can be achieved by matching features in 3D space (e.g. 3D minutia matching). Observing fingerprint in 3D images, we also found that the center part of the finger is higher than the side part and the core point of fingerprint almost locates at the highest part of the finger. These characteristics of 3D fingerprint images benefit alignment when comparing two fingerprint images. Thus, future work goes on excavating the merits of 3D fingerprint images and making such advantage benefit fingerprint recognition.

6. Discover the relationship between different levels of fingerprint features and propose more powerful fusion strategy. With the available of 3D fingerprint images, 3D fingerprint features which are coarser than level 1 fingerprint features can be obtained as mentioned in the thesis. We did not pay much attention on fusion among different features. We believe that exploring suitable fusion schemes for different levels of fingerprint features will be very interesting and meaningful.

BIBLIOGRAPHY

[1] International Biometric Group, *The most trusted report on the biometrics industry*, available at https://ibgweb.com/products/reports/bmir-2009-2014.

[2] R. Clarke, "Human identification in information systems: management challenges and public policy issues," *Information Technology and People*, vol. 7, no. 4, pp. 6-37, 1994.

[3] B. Miller, "Vital signs of identity," *IEEE Spectrum*, vol. 31, no. 2, pp. 22-30, 1994.

[4] S. Davies, "Touching big brother: how biometric technology will fuse flesh and machine," *Information Technology and People*, vol. 7, no. 4, pp. 60-69, 1994.

[5] A. Jain, R. Bolle, and S. Pankani, eds., *Biometrics: Personal Identification in Networked Society*, Kluwer Academic Publishers, USA, 1999.

[6] D. Zhang, *Automated Biometrics: Technologies and Systems*, Kluwer Academic Publishers, USA, 2000.

[7] BCC Research, *The global biometrics market*, available at http://www.bccresearch.com/report/IFT042B.html.

[8] Scientific Working Group on Friction Ridge Analysis, Study and Technology, *Peer reviewed glossary of the scientific working group on friction ridge analysis, study and technology (SWGFAST)*, available at http://www.swgfast.org/documents/glossary/090508_Glossary_2.0.pdf.

[9] S. Pankanti, S. Prabhakar, and A. Jain, "On the individuality of fingerprints," *IEEE Transactions on Pattern Analysis and Machine Intelligence*, vol. 24, no. 8, pp. 1010-1025, 2002.

[10] J. Chen and Y. Moon, "The statistical modeling of fingerprint minutiae distribution with implications for fingerprint individuality studies," in *Proceedings of 2008 IEEE Conference on Computer Vision and Pattern Recognition*, pp. 1-7, 2008.

[11] Y. Chen and A. K. Jain, "Beyond minutiae: A fingerprint individuality model with pattern, ridge and pore features," in *Proceedings of the 3rd International Conference on Biometrics*, pp. 523-533, 2009.

[12] D. Ashbaugh, *Quantitative-Qualitative Friction Ridge Analysis: An Introduction to Basic and Advanced Ridgeology*, Boca Raton: CRC Press, 1999.

[13] W. Herschel, *The Origin of Finger-Printing*, Oxford University Press, 1916.

[14] W. Herschel, "Skin furrows of the hand," *Nature*, vol. 23, no. 578, pp. 76, 1880.

[15] H. Faulds, "On the skin-furrows of the hand," *Nature*, vol. 22, no. 574, pp. 605, 1880.

[16] F. Galton, *Finger Prints*, Macmillan, London, 1892.

[17] H. Lee and R. Gaensslen, *Advances in Fingerprint Technology*, 2nd edition, Elsevier, New York, 2001.

[18] D. Maltoni, D. Maio, A. Jain, and S. Prabhakar, *Handbook of Fingerprint Recognition*, 2nd Edition, Springer, New York, 2009.

[19] A. Ross and A. Jain, "Biometric sensor interoperability: A case study in fingerprints," *in Proceedings of Biometric Authentication Workshop*, 2004.

[20] M. Tartagni and R. Guerrieri, "A fingerprint sensor based on the feedback capacitive sensing scheme," *IEEE Journal of Solid-State Circuits*, vol. 33, no. 1, pp. 133-142, 1998.

[21] W. Yau, T. Chen and P. Morguet, "Benchmarking of fingerprint sensors," *in Proc. Workshop on Biometric Authentication (in ECCV 2004)*, LNCS 3087, pp.89-99, 2004.

[22] J. Mainguet, M. Pegulu and B. Harris, "Fingerchip: thermal imaging and finger sweeping in a silicon fingerprint sensor," *in Proc. Workshop on Automatic Identification Advances Technologies*, pp. 91-94, 1999.

[23] D. Setlak, "Advances in fingerprint sensors using RF imaging techniques," *in Automatic Fingerprint Recognition Systems, N. Ratha and R. Bolle (Eds.), Springer, New York*, pp. 27-53, 2004.

[24] S. Memon, M. Sepasian, and W. Balachandran, "Review of finger print sensing technologies," *IEEE International Conference on Multitopic*, pp. 226-231, 2008.

[25] W. Bicz, D. Banasiak, P. Bruciak, S. Gumienny, Z. Gumuliński, D. Kosz, A. Krysiak, W. Kuczyński, M. Pluta and G. Rabiej, "Fingerprint structure imaging based on an ultrasound camera," *Instrumentation Science and Technology*, vol. 27, pp. 295-303, 1999.

[26] J. Schneider, "Ultrasonic fingerprint sensors," *in Advances in biometrics: sensors, algorithms and systems, N.K. Ratha and V. Govindaraju (Eds.), Springer, London*, pp. 63-74, 2007.

[27] X. Xia and L. O'Gorman, "Innovations in fingerprint capture devices," *Pattern Recognition*, vol. 36, no. 2, pp. 361-369, 2003.

[28] M. Hase and A. Shimisu, "Entry method of fingerprint image using a prism," *Trans. Institute Electron. Commum. Eng. Jpn*., vol. J67–D, pp. 627-628, 1984.

[29] R. Bahuguna and T. Corboline, "Prism fingerprint sensor that uses a holographic element," *Applied Optics*, vol. 35, no. 26, pp. 5242-5245, 1996.

[30] G. Zhou, Y. Qiao and F. Mok, "Fingerprint sensing system using a sheet prism," US Patent 5796858, 1998.

[31] I. Fujieda, Y. Ono and S. Sugama, "Fingerprint image input device having an image sensor with openings," US Patent 5446290, 1995.

[32] N. Young, G. Harkin, R. Bunn, D. McCulloch, R. Wilks and A. Knapp, "Novel fingerprint scanning arrays using polysilicon tft's on glass and polymer substrates," *IEEE Electron Device Letters*, vol. 18, no. 1, pp. 19-20, 1997.

[33] G. Parziale, E. Diaz-Santana and A. Jain, "3D touchless fingerprints: compatibility with legacy rolled images," *in Proc. Biometric Symposium*, 2006.

[34] G. Parziale, "Touchless fingerprinting technology," *in Advances in Biometrics: Sensors, Algorithms and Systems, N.K. Ratha and V. Govindaraju (Eds.), Springer, Heidelberg*, pp. 25-48, 2007.

[35] G. Parziale and E. Diaz-Santana, "The surround imager: a multi-camera touchless device to acquire 3D rolled-equivalent fingerprints," *in: Proceedings of International Conference on Biometrics (ICB), Hong Kong, China*, vol. 3832, pp. 244-250, 2006.

[36] B. Hiew, A. Teoh and Y. Pang, "Touchless fingerprint recognition system," *in Proc. Workshop on Automatic Identification Advanced Technologies*, pp. 24-29, 2007.

[37] C. Lee, S. Lee, J. Kim and S. Kim., "Preprocessing of a fingerprint image captured with a mobile camera," *in Proc. Int. Conf. on Biometrics*, LNCS 3832, pp. 348-355, 2006.

[38] D. Lee, K. Choi, H. Choi and J. Kim, "Recognizable-image selection for fingerprint recognition with a mobile-device camera," *IEEE Transaction on Systems, Man, and Cybernetics, Part B*, vol. 38, no. 1, pp. 233-243, 2008.

[39] D. Lee, K. Choi, H. Choi and J. Kim, "Recognizable-image selection for fingerprint recognition with a mobile-device camera," *IEEE Transaction on Systems, Man, and*

Cybernetics, Part B, vol. 38, no. 1, pp. 233-243, 2008.

[40] A. Fatehpuria, L. Lau and L. Hassebrook, “Acquiring a 2D rolled equivalent fingerprint Image from a non-contact 3D finger scan,” *in Proc. SPIE Conf. on Biometric Technology for Human Identification III*, 2006.

[41] R. Rowe, K. Nixon and P. Butler, “Multispectral fingerprint image acquisition,” *in Advances in Biometrics: Sensors, Algorithms and Systems, N.K. Ratha and V. Govindaraju (Eds.), Springer, London*, pp. 3-24, 2007.

[42] G. Levi and F. Sirovich, “Structural description of fingerprint images,” *Information Sciences*, pp. 327-355, 1972.

[43] A. Moenssens, *Fingerprint Techniques*, Chilton Book Company, London, 1971.

[44] B. Bindra, O. P. Jasuja, and A. K. Singla, “Poroscopy: A method of personal identification revisited,” *Internet Journal of Forensic Medicine and Toxicology*, vol. 1, 2000.

[45] A. Kumar and Y. Zhou, “Contactless fingerprint identification using level zero features,” *Proc CVPR'11*, pp. 121-126, 2011.

[46] A. Sibbald, “Method and apparatus for fingerprint characterization and recognition using auto-correlation pattern,” US Patent 5633947, 1994.

[47] A. Stoianaov, C. Soutar, and A. Graham, “High-speed fingerprint verification using an optical correlator,” *in Proceedings SPIE*, vol. 3386, pp. 242-252, 1998.

[48] A. Bazen, G. Verwaaijen, S. Gerez, L. Veelenturf, and B. Zwaag, “A correlation-based fingerprint verification system,” *in Proceedings of the ProRISC2000 Workshop on Circuits, Systems and Signal Processing, (Veldhoven, Netherlands)*, pp. 205-213, 2000.

[49] F. Pernus, S. Kovacic, and L. Gyergyek, “Minutiae-based fingerprint recognition,” *in Proceedings of the Fifth International Conference on Pattern Recognition*, pp. 1380-1382, 1980.

[50] A. K. Jain, L. Hong, and R. Bolle, “On-line fingerprint verification,” *IEEE Transactions on Pattern Analysis and Machine Intelligence*, vol. 19, pp. 302-314, 1997.

[51] L. Coetzee and E. Botha, “Fingerprint recognition in low quality images,” *Pattern Recognition*, vol. 26, no. 10, pp. 1441-1460, 1993.

[52] A. Willis and L. Myers, “A cost-effective fingerprint recognition system for use with low-quality prints and damaged fingertips,” *Pattern Recognition*, vol. 34, no. 2, pp. 255-270, 2001.

[53] G. Fang, S. Srihari, H. Srinivasan and P. Phatak, “Use of ridge points in partial fingerprint matching,” *in Proc. SPIE Conf. on Biometric Technology for Human Identification IV,* vol. 6539, 2007.

[54] J. Stosz and L. Alyea, “Automated system for fingerprint authentication using pores and ridge structure,” in *Proc. SPIE*, pp. 210-223, 1994.

[55] M. Trauring, “Automatic comparison of finger-ridge patterns,” *Nature*, pp. 938-940, 1963.

[56] B. Mehtre and M. Murthy, “A minutiae based fingerprint identification system,” in *Proceedings of the 2nd International Conference on Advances in Pattern Recognition and Digital Techniques*, 1986.

[57] N. Ratha and R. Bolle, *Automatic Fingerprint Recognition Systems*, Springer, New York, 2004.

[58] L. Hong, Y. Wan, and A. K. Jain, “Fingerprint image enhancement: Algorithms and performance evaluation,” *IEEE Transactions on Pattern Analysis and Machine Intelligence*, vol. 20, pp. 777-789, 1998.

[59] B. G. Sherlock, D. M. Monro, and K. Millard, "Fingerprint enhancement by directional Fourier filtering," *IEE Proceedings on Vision, Image and Signal Processing*, vol. 141, no. 2, pp. 87-94, 1994.

[60] A. K. Jain, S. Prabhakar, L. Hong, and S. Pankanti, "Filterbank-based fingerprint matching," *IEEE Transactions on Image Processing*, vol. 9, pp. 846-859, 2000.

[61] R. Cappelli, D. Maio, and D. Maltoni, "Fingerprint classification by directional image partitioning," *IEEE Transactions on Pattern Analysis and Machine Intelligence*, vol. 21, no. 5, pp. 402-421, 1999.

[62] N. Ratha, J. Connell, and R. Bolle, "Image mosaicing for rolled fingerprint construction," in *Proceedings of the 14th International Conference on Pattern Recognition*, vol. 2, pp. 1651-1653, 1998.

[63] A. Ross, S. Dass, and A. Jain, "A deformable model for fingerprint matching," *Pattern Recognition*, vol. 38, pp. 95-103, 2005.

[64] A. Ross, A. K. Jain, and J. Reisman, "A hybrid fingerprint matcher," *Pattern Recognition*, vol. 36, pp. 1661-1673, 2003.

[65] Y. Chen, S. Dass, and A. Jain, "Fingerprint quality indices for predicting authentication performance," in *Proceedings of Audio- and Video-based Biometric Person Authentication*, pp. 160-170, 2005.

[66] L. Liu, T. Jiang, J. Yang, and C. Zhu, "Fingerprint registration by maximization of mutual information," *IEEE Transactions on Image Processing*, vol. 15, pp. 1100-1110, 2006.

[67] B. Bhanu and X. Tan, *Computational Algorithms for Fingerprint Recognition*, Kluwer Academic Publishers, 2004.

[68] K. Kryszczuk, P. Morier, and A. Drygajlo, "Study of the distinctiveness of level 2 and level 3 features in fragmentary fingerprint comparison," in *Proceedings of Biometric Authentication, ECCV 2004 International Workshop*, pp. 124-133, 2004.

[69] A. Roddy and J. Stosz, "Fingerprint features – Statistical analysis and system performance estimates," Proceedings of the IEEE, vol. 85, no. 9, pp. 1390-1421, 1997.

[70] Q. Zhao, L. Zhang, D. Zhang, N. Luo, and J. Bao, "Adaptive pore model for fingerprint pore extraction," *Proc.18th International Conference on Pattern Recognition*, 2008.

[71] Q. Zhao, L. Zhang, D. Zhang, and N. Luo, "Direct pore matching for fingerprint recognition," *ICB'09*, pp. 597-606, 2009.

[72] Q. Zhao, D. Zhang, L. Zhang, and N. Luo, "High resolution partial fingerprint alignment using pore–valley descriptors," *Pattern Recognition*, vol. 43, no.3, pp. 1050-1061, 2009.

[73] CDEFFS, *Data Format for the Interchange of Extended Fingerprint and Palmprint Features*, Version 0.4, 2009.

[74] International Biometric Group, *Analysis of Level 3 Features at High Resolutions (Phase II)*, 2008.

[75] A. Jain, Y. Chen, and M. Demirkus, "Pores and ridges: fingerprint matching using level 3 features," *in Proceedings of the18th International Conference on Pattern Recognition*, vol. 4, pp. 477-480, 2006.

[76] A. Jain, Y. Chen, and M. Demirkus, "Pores and ridges: high-resolution fingerprint matching using level 3 features," *IEEE Transactions on Pattern Analysis and Machine Intelligence*, vol. 29, no. 1, pp. 15-27, 2007.

[77] K. Kryszczuk, A. Drygajlo, and P. Morier, "Extraction of level 2 and level 3 features for fragmentary fingerprints," *in Proceedings of the Second COST Action 275 Workshop, Vigo, Spain*, pp. 83-88, 2004.

[78] M. Ray, P. Meenen, and R. Adhami, “A novel approach to fingerprint pore extraction,” *in Proceedings of the 37th South-eastern Symposium on System Theory*, pp. 282-286, 2005.

[79] N. Parsons, J. Smith, E. Thonnes, L. Wang, and R. Wilson,” Rotationally invariant statistics for examining the evidence from the pores in fingerprints,” *Law, Probability and Risk*, vol. 7, pp. 1-14, 2008.

[80] Q. Zhao, D. Zhang, L. Zhang, and N. Luo, “Adaptive fingerprint pore modeling and extraction,” *Pattern Recognition*, vol. 43, no. 8, pp. 2833-2844, 2010.

[81] Y. Song, C. Lee, J. Kim, “A new scheme for touchless fingerprint recognition system,” *in: Proceedings of the 2004 International Symposium on Intelligent Signal Processing and Communication Systems*, pp. 524-527, 2004.

[82] C. Lee, S. Lee, J. Kim, “A study of touchless fingerprint recognition system,” *Lecture Notes in Computer Science*, vol. 4109, pp. 358-365, 2006.

[83] H. Choi, K. Choi, J. Kim, “Mosaicing touchless and mirror-reflected fingerprint images,” *IEEE Trans. On Information Forensics and Security*, vol. 5, no. 1, pp. 52-61, 2010.

[84] B. Hiew, Andrew B.J. Teoh, Y. Pang, “Touch-less fingerprint recognition system,” *IEEE Workshop on Automatic Identification Advanced Technologies*, pp. 24-29, 2007.

[85] Y. Chen, *Extended Feature Set and Touchless Imaging for Fingerprint Matching*, Michigan State University, 2009.

[86] J. S. Han, Z. Tan, K. Sato, M. Shikida, “Thermal characterization of micro heater arrays on a polyimide film substrate for fingerprint sensing applications,” *Journal of Micromechanics and Microengineering*, vol.15, no. 2, pp. 282-289, 2005.

[87] H. Cummins, W. J. Waits, J. T. McQuitty, “The breadths of epidermal ridges on the finger tips and palms: a study of variation,” *American Journal of Anatomy*, vol. 68, no.1, pp. 127-150, 1941.

[88] M. Acree, “Is there a gender difference in fingerprint ridge density?” *Forensic Science International*, vol. 102, no.1, pp. 35-44, 1999.

[89] Q. Zhao, *High Resolution Fingerprint Additional Features Analysis*, The Hongkong Polytechnic Univeristy, 2010

[90] D. Zhang, W. Wang, Q. Huang, S. Jiang, and W. Gao, “Matching images more efficiently with local descriptors,” *in Proceedings of the 19th International Conference on Pattern Recognition*, 2008.

[91] D. Donoho, “For most large underdetermined systems of linear equations the minimal l1-norm solution is also the sparsest solution,” *Comm. Pure and Applied Math.*, vol. 59, no. 6, pp. 797-829,2006.

[92] I. Daubechies, M. Defriese, and C. DeMol, “An iterative thresholding algorithm for linear inverse problems with a sparsity constraint,” Comm. Pure Applied Math., vol. 57, no. 11, pp. 1413-1457, 2004.

[93] S. Boyd and L. Vandenberghe, *Convex Optimization*, Cambridge University, 2004.

[94] S. J. Kim, K. Koh, M. Lustig, S. Boyd, and D. Gorinevsky, “A method for large-scale l1-regularized least squares,” *IEEE Journal on Selected Topics in Signal Processing*, vol. 1, no. 4, pp. 606-617, 2007.

[95] J. Wright, A. Yang, A. Ganesh, S. Sastry, and Y. Ma, “Robust face recognition via sparse representation,” *IEEE Transactions on Pattern Analysis and Machine Intelligence*, vol. 31, no. 2, pp. 210-227, 2009.

[96] P. Simard, Y. Cun, and J. Denker, “Efficient pattern recognition using a new transformation distance,” *in Proceedings of Advances in Neural Information Processing Systems 5 (NIPS*

Conference), pp. 50-58, 1992.

[97] D. Keysers, J. Dahmen, T. Theiner, and H. Ney, "Experiments with an extended tangent distance," *in Proceedings of the 15th International Conference on Pattern Recognition*, pp. 2038-2041, 2000.

[98] D. Keysers, W. Macherey, H. Ney, and J. Dahmen, "Adaptation in statistical pattern recognition using tangent vectors," *IEEE Transactions on Pattern Analysis and Machine Intelligence*, vol. 26, no. 2, pp. 269-274, 2004.

[99] S. Yan and H. Wang, "Semi-supervised learning by sparse representation," *in Proceedings of SIAM International Conference on Data Mining*, pp. 792-801, 2009.

[100] M. Fishler and R. Bolles, "Random sample consensus: a paradigm for model fitting with applications to image analysis and automated cartography," *Communications of the ACM*, vol. 24, no. 6, pp. 381-395, 1981.

[101] M. Zuliani, *RANSAC for Dummies*, MathWorks, 2008. Available at: http://www.mathworks.com.

[102] Mitsubishi touchless fingerprint sensor. Available at: http://global.mitsubishielectric.com.

[103] Lumidigm multispectral fingerprint imaging. Available at: http://www.lumidigm.com.

[104] TST biometrics BiRD3. Available: http://www.tst-biometrics.com.

[105] F. Chen, "3D fingerprint and palm print data model and capture devices using multi structured lights and cameras," US Patent Application Publication, Pub. No. 2006/0120576, 2006.

[106] Fingerprint science group: handshot. Available at: http://privacy.cs.cmu.edu/dataprivacy/projects/handshot /index.html.

[107] TBS touchless fingerprint imaging: 3D-enroll, 3D-terminal. Available at: http://www.tbsinc.com.

[108] A. Elli, "Understanding the color of human skin," *in Proc. 6th SPIE Conf. Human Vision and Electronic Imaging, SPIE*, vol. 4299, pp. 243-251, 2001.

[109] L. Wang, R. El-Maksoud, J. Sasian, and V. Valencia, "Illumination scheme for high-contrast, contactless fingerprint images," *Proc. SPIE*, vol. 7429, pp. 742911-1-742911-7, 2009.

[110] U. Park, S. Pankanti, and A. Jain, "Fingerprint verification using SIFT features," *Proc. of SPIE*, vol. 6944, pp. 69440K-69440K-9, 2008.

[111] J. Feng, "Combining minutiae descriptors for fingerprint matching," *Pattern Recognition*, vol. 41, no. 1, pp. 342-352, 2008.

[112] S. Malathi and C. Meena, "Partial fingerprint matching based on SIFT features," *International Journal on Computer Science and Engineering*, vol. 2, no. 4, pp. 1411-1414, 2010.

[113] A. Jain and A. Ross, "Fingerprint mosaicking," *in: Proceedings of IEEE International Conference on Acoustics, Speech, and Signal Processing (ICASSP) , Orlando, Florida*, vol. 4, pp. IV-4064 - IV-4067, 2002.

[114] S. Shah, A. Ross, J. Shah, and S. Crihalmeanu, "Fingerprint mosaicing using thin plate splines," *in: The Biometric Consortium Conference*, 2005.

[115] K. Choi, H. Choi, S. Lee, and J. Kim, "Fingerprint image mosaicking by recursive ridge mapping," *Special Issue on Recent Advances in Biometrics Systems, IEEE Trans. Syst., Man, Cybern. B*, vol. 37, no. 5, pp. 1191-1203, 2007.

[116] D. Lowe, "Distinctive image features from scale-invariant keypoints," *International Journal of Computer Vision*, vol. 60, no. 2, pp. 91-110, 2004.

[117] J. Kittler, J. lllingworth, J. Foglein, and K. Paler, “An automatic thresholding algorithm and its performance,” *in Proc. Seventh Int. Conf: Pattern Recognition, Montreal. P.Q. Canada*, vol. 1, pp. 287-289, 1984.

[118] M. Grabner, H. Grabner, and H. Bischof, “Fast Approximated SIFT,” *ACCV’06*, pp. 918-927, 2006.

[119] R. Hartley, *Multiple View Geometry in Computer Vision*, Cambridge Univ. Press, Cambridge, U.K., 2000.

[120] C. Hernandez, G. Vogiatzis, and R. Cipolla, “Multiview photometric stereo,” *IEEE Trans. Pattern Anal. Mach. Intell.*, vol. 30, no. 3, pp. 548-554, 2008.

[121] F. Blais, M. Rious, and J. Beraldin, “Practical considerations for a design of a high precision 3-D laser scanner system,” *Proc. SPIE*, vol. 959, pp. 225-246, 1988.

[122] Y. Wang, L. Hassebrook, and D. Lau, “Data acquisition and processing of 3-D Fingerprints,” *IEEE Transactions on Information Forensics and Security*, vol. 5, no. 4, pp. 750-760, 2010.

[123] G. Stockman, S. Chen, G. Hu, and N. Shrikhande, “Sensing and recognition of rigid objects using structured light,” *IEEE Control Syst. Mag.*, vol. 8, no. 3, pp. 14-22,1988.

[124] G. Hu and G. Stockman, “3-D surface solution using structured light and constraint propagation,” *IEEE Trans. Pattern Anal. Mach. Intell.*, vol. 11, no. 4, pp. 390-402, 1989.

[125] Z. Zhang, “A flexible new technique for camera calibration,” *IEEE Trans. on Pattern Anal. Mach. Intell.*, vol. 24, no. 11, pp. 1330-1334, 2000.

[126] J. Bouguet, *Camera Calibration Toolbox for Matlab*. Available at: http://www.vision.caltech.edu/bouguetj/calib_doc/download/index.html.

[127] G. Parziale and A. Niel, “A fingerprint matching using minutiae triangulation,” *on Proc. of International Conference on Biometric Authentication (ICBA), LNCS*, vol. 3072, pp. 241-248, 2004.

[128] S. Rusinkiewicz, O. Holt, and M. Levoy, “Real-time 3D model acquisition,” *The Proceedings of the 29th annual conference on Computer graphics and interactive techniques*, no. 3, vol. 21, pp. 438-446, 2002.

[129] B. Bradley, A. Chan, and M. Hayes, “A simple, low cost, 3D scanning system using the laser light-sectioning method,” *IEEE International Instrumentation and Measurement Technology Conference Victoria, Vancouver Island, Canada*, pp. 299-304, 2002.

[130] D. Zhang, V. Kanhangad, N. Luo, and A. Kumar, “Robust palmprint verification using 2D and 3D features,” *Pattern Recognition*, vol. 43, no. 1, pp. 358-368, 2010.

[131] H. O. Saldner and J. M. Huntley, “Temporal phase unwrapping: Application to surface profiling of discontinuous objects,” *Appl. Opt.*, vol. 36, no. 13, pp. 2770–2775, 1997.

[132] D. Zhang, G. Lu, and W. Li, “palmprint recognition using 3-D information,” *IEEE Trans. on SMC-part C: Applications and Reviews*, vol. 39, no. 5, pp. 505-519, 2009.

[133] S. Chatterjee and A. Hadi, “Influential observations, high leverage points, and outliers in linear regression,” *Statistical Science*, vol. 1, no. 3, pp. 379-416, 1986.

[134] N. Draper and H. Smith, *Applied Regression Analysis*, 2nd ed., Wiley, 1981.

[135] S. Chikkerur, A Cartwright and V. Govindaraju, “Fingerprint enhancement using STFT analysis,” *Pattern Recognition*, vol. 40, no. 1, pp. 198-211, 2007.

[136] S. Jirachaweng and V. Areekul, “Fingerprint enhancement based on discrete cosine transform,” *in Proc. Int. Conf. on Biometrics, LNCS 4642*, pp. 96-105, 2007.

[137] J. Weichert, “Coherence-enhancing diffusion filtering,” *International Journal of Computer Vision*, vol. 31, no. 2-3, pp111-127, 1999.

[138] H. Chen and G. Dong, “Fingerprint image enhancement by diffusion processes,” *in Proceedings of the 13th International Conference on Image Processing*, pp. 297-300, 2006.

[139] Y. Hao and C. Yuan, “Fingerprint image enhancement based on nonlinear anisotropic reverse diffusion equations,” *in Proceedings of The 26th Annual International Conference of the IEEE Engineering in Medicine and Biology Society*, pp. 1601-1604, 2004.

[140] R. Hastings, “Ridge enhancement in fingerprint images using oriented diffusion,” *Digital Image Computing Techniques and Applications*, pp. 245-252, 2007.

[141] A. Almansa and T. Lindeberg, “Fingerprint enhancement by shape adaptation of scale-space operators with automatic scale selection,” *IEEE Transactions on Image Processing*, vol. 9, no. 12, pp. 2027-2042, 2000.

[142] M. Xie and Z. Wang, “Fingerprint enhancement based on edge-directed diffusion,” *in Proceedings of the 11th International Conference on Image Processing*, 2004.

[143] C. Samir, A. Srivastava, and M. Daoudi, “Three-dimensional face recognition using shapes of facial curves,” *IEEE Trans. on Pattern Anal. Mach. Intell.*, vol. 28, no. 11, pp. 858-1863, 2006.

[144] X. Lu, A. Jain, and D. Colbry, “Matching 2.5D face scans to 3D models,” *IEEE Trans. Pattern Anal. Mach. Intell.*, vol. 28, no. 1, pp. 31-43, 2006.

[145] P. Yan and K. Bowyer, “Multi-biometrics 2D and 3D ear recognition,” *in Proc. AVBPA 2005*, pp. 503-512, 2005.

[146] H. Chen and B. Bhanu, “Human ear recognition in 3D,” *IEEE Trans. on Pattern Anal. Mach. Intell.*, vol. 29, no. 4, pp. 718-737, 2007.

[147] P. Yan and K. Bowyer, “Biometric recognition using 3D ear shape,” *IEEE Trans. on Pattern Anal. Mach. Intell.*, vol. 29, no. 8, pp. 1297-1308, 2007.

[148] D. Zhang, G. Lu, W. Li, L. Zhang, and N. Luo, “Three dimensional palmprint recognition using structured light imaging,” *2nd IEEE International Conference on Biometrics: Theory, Applications and Systems, BTAS*, pp. 1-6, 2008.

[149] W. Li, L. Zhang, D. Zhang, G. Lu, and J. Yan, “Efficient joint 2D and 3D palmprint matching with alignment refinement,” *in: Proc. CVPR 2010*, pp. 795-801, 2010.

[150] W. Li, D. Zhang, and L. Zhang, “Three dimensional palmprint recognition,” *IEEE International Conference on Systems, Man, and Cybernetics*, pp. 4847-4852, 2009.

[151] N. Cornea, D. Silver, and P. Min, “Curve-skeleton properties, applications, and algorithms.” *IEEE Transactions on Visualization and Computer Graphics*, vol. 13, no. 3, pp. 530-548, 2007.

[152] J. Scheneider and D. Wobschall, “Live scan fingerprint imagery using high resolution C-scan ultrasonography,” *Proc. 25th Int. Conf. on Security Technology*, pp. 88-95, 1991.

[153] A. Kong and D. Zhang, “Competitive coding scheme for palmprint verification,” *in Proc. Seventeenth Int. Conf: Pattern Recognition*, vol. 1, pp. 520-523, 2004.

[154] D. Zhang, W. Kong, J. You, M. Wong, “On-line palmprint identification,” *IEEE Trans. Pattern Anal. Mach. Intell.*, no. 9, vol. 25, pp. 1041-1050, 2003.

[155] A. Ross, K. Nandakumar, and A. Jain, *Handbook of Multibiometrics*, Springer, 2006.

[156] M. Tico and P. Kuosmanen, “Fingerprint matching using an orientation-based minutia descriptor,” *IEEE Trans. Pattern Anal. Mach. Intell.*, vol. 25, no. 8, pp. 1009-1014, 2003.

[157] X. Chen, J. Tian, X. Yang, “A new algorithm for distorted fingerprints matching based on normalized fuzzy similarity measure,” *IEEE Trans. Image Process.*, vol. 15, no. 3, pp. 767-776, 2006.

[158] X. Jiang and W. Yau, "Fingerprint minutiae matching based on the local and global structures," *in: Proceedings of the International Conference on Pattern Recognition, Barcelona*, vol. 2 , pp. 1038-1041, 2000.

[159] X. Luo, J. Tian, and Y. Wu, "A minutiae matching algorithm in fingerprint verification," *in: Proceedings of the International Conference on Pattern Recognition, Barcelona*, vol. 4, pp. 833-836, 2000.

[160] N. Ratha, R. Bolle, V. Pandit, and V. Vaish, "Robust fingerprint authentication using local structural similarity," *in: Fifth IEEE Workshop on Applications of Computer Vision*, pp. 29-34, 2000.

[161] J. Qi and Y. Wang, "A robust fingerprint matching method," *Pattern Recognition*, vol. 38, no. 10, pp. 1665-1671, 2005.

[162] F. Liu, Q. Zhao, L. Zhang, and D. Zhang, "Fingerprint pore matching based on sparse representation," *in Proceedings of the 20th International Conference on Pattern Recognition*, 2010.